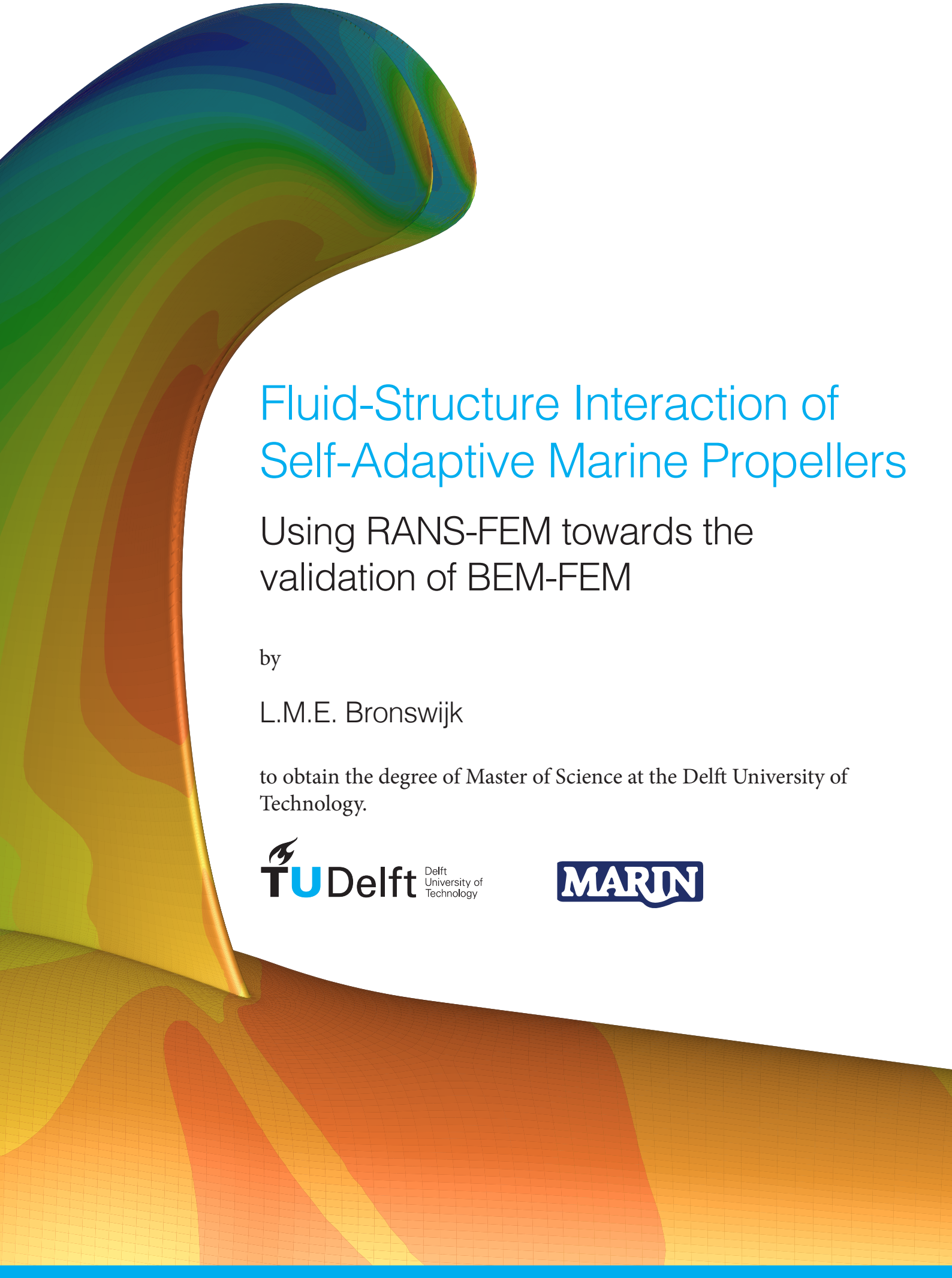

Fluid-Structure Interaction of Self-Adaptive Marine Propellers

Using RANS-FEM towards the validation of BEM-FEM

by

L.M.E. Bronswijk

to obtain the degree of Master of Science at the Delft University of Technology.

TU Delft Delft University of Technology

MARIN

Fluid-Structure Interaction of Self-Adaptive Marine Propellers

Using RANS-FEM towards the validation of BEM-FEM

by

L.M.E. Bronswijk

to obtain the degree of Master of Science in Marine Technology
at the Delft University of Technology

to be defended publicly on Wednesday June 28, 2017 at 10:30 AM.

Student number:	4006143	
Project duration:	September, 2016 – June, 2017	
Thesis committee:	Prof. dr. ir. M.L. Kaminski	TU Delft
	ir. P. J. Maljaars	TU Delft
	Dr. ir. P. R. Wellens	TU Delft
	Dr. ir. H. C. J. van Wijngaarden	MARIN
	ir. J. Windt	MARIN

An electronic version of this thesis is available at http://repository.tudelft.nl/.

MARIN TU Delft

Abstract

For decades, marine propeller blades have been manufactured solely using alloys of metals like nickel, aluminium, bronze and stainless steel. However, recent studies have shown that using composites as material for the propeller blades can have benefits. Due to the material the blades becomes self-adaptive (flexible). The claimed benefits are for instance better corrosive characteristics, better vibration control and higher cavitation inception speeds. However, a challenge with flexible propellers is that in the design stage, the Fluid-Structure Interaction (FSI) has to be taken into account. If simulations are performed, the method that is mostly used is a coupling between an existing fluid solver and structural solver. The study presented in this report is part of the Greenprop project, which has the aim to calculate the hydro elastic response of flexible propellers by developing a coupling between a Boundary Element Method (BEM) and Finite Element Method (FEM), i.e. BEM-FEM simulations. In these BEM-FEM simulations a pressure correction is applied for the tip vortex, a viscous effect that is not captured by BEM. The settings of this correction showed a large influence on the hydro elastic response of the propeller blades. The study presented in this report is aimed towards the validation of BEM-FEM with Reynolds Averaged Navier Stokes (RANS) coupled to FEM. By using RANS, viscous effects are taken into account. Within the scope of this study simulations are performed with the epoxy propeller of Greenprop in a uniform wakefield, using RANS solver ReFRESCO and FE package ANSYS.

First, a 2D benchmark case is carried out. The reason for this case is to get familiar with the methods and to check the reliability of the FSI module in ReFRESCO. It is concluded that the FSI module of ReFRESCO gives similar results compared to literature. The FSI module is tested thoroughly and more insight is obtained in the settings and performance of the FSI module of ReFRESCO. The benchmark case has led to the conclusion that the FSI module is reliable and can be used in the propeller study.

Second, the propeller study is performed. This study is divided in a rigid and a flexible part. For the rigid propeller case, the open water results are compared to experiments and BEM simulations both performed by Greenprop. The accuracy of the RANS results is determined by evaluating the numerical uncertainty and comparing to experimental results. For advance ratios up to 0.8 a good resemblance is found with a maximum deviation of -4% for RANS compared to experiments. For advance ratios larger than 0.8 both the deviations in results and numerical uncertainties of RANS increase. The influence of blockage, modelling- and experimental errors are discussed. In the comparison with BEM lower thrust and torque are found for RANS, which is attributed to viscous effects. The pressure distributions on the blade of RANS and BEM are compared. The results found in the rigid propeller are used in the flexible propeller study.

For the RANS-FEM simulations of the flexible propeller, the FE model is coupled to the RANS solver. The eigenfrequencies of the FE model are used as validation, the first two modes show a deviation of 0.3% and 0.8% compared to the Greenprop FE model. A decrease in thrust and torque is obtained for the flexible RANS-FEM compared to the rigid RANS simulations. This led to an open water efficiency increase of -0.5% to -1.7%. For BEM-FEM the same trends are visible in the influence of flexibility on thrust and torque. For the deformation of the blade, bending and pitch are analysed. The bending deformation of the low advance ratio shows a good resemblance with the experimental results, for pitch the difference was too large to draw a conclusion. This is attributed to post processing and modelling errors at the tip of the blade in ReFRESCO. The comparison of bending and pitch with BEM-FEM led to several recommendations according to the settings of the correction applied in BEM-FEM. From the flexible propeller study it can be concluded that more insight is gained in the response of the epoxy propeller in uniform flow obtained with RANS-FEM compared to RANS, BEM-FEM and experiments.

Preface

This thesis is the final work to obtain the degree of Master of Science in Marine Technology with the specialisation Ship and Offshore Structures. This research is carried out at Maritime Research Institute Netherlands (MARIN) in Wageningen and the Ship Hydromechanics and Structures department of the TU Delft. The study is part of the Greenprop project, which focuses on calculating the hydro-elastic response of flexible marine propellers. Simulations are performed with the epoxy propeller of Greenprop in a uniform wakefield. RANS solver ReFRESCO is used for the fluid part and Finite Element (FE) package ANSYS for the structural part. The FSI module of ReFRESCO is used for the coupled RANS-FEM simulations.

I would like to thank Pieter Maljaars who came up with the assignment but also for his advice, help and patience during my thesis. I would like to thank MARIN for the facilities and especially supervisor Jaap Windt who got me familiarised with Linux, ReFRESCO and the FSI module. Next to that, my other supervisors, Professor Kaminski and Peter Wellens for their support during progress meetings. Last but not least, Erik van Wijngaarden for reviewing my report several times and Arjan Lampe and Douwe Rijpkema for answering my questions and providing tools used in this study.

L.M.E. Bronswijk
Delft, June 16, 2017

Contents

List of Figures

List of Tables

Nomenclature

$[C]$	Damping matrix
$[K]$	Stiffness matrix
$[M]$	Mass matrix
α	Angle of attack, Constant, Mass proportional damping
β	Stiffness proportional damping
∇	Volume of an element
$\ddot{x}$	Acceleration
$\dot{x}$	Velocity
Γ	Continuous interface
γ_j	Interpolation constant
μ	Dynamic viscosity
ν	Poisson's ratio
Ω	Volume domain
ω_n	Natural frequency
Φ	Pitch angle
ϕ	Flow quantity, Radial basis function
ρ	Density
$\mathbf{Q}$	Vector in equations of motion
$\mathbf{u}_f$	Displacement fluid interface
$\mathbf{u}_s$	Displacement structural interface
θ_S	Skew angle
$\vec{v}$	Velocity
A	Area, mesh A, Vector in equations of motion
c	Chord, Damping
D	Drag force, Diameter
E	Young's Modulus
e_e	local error of an element
F	Flux, Force
f_i	Body forces
h_i	Grid size

I	Moment of inertia
J	Advance ratio
k	Stiffness
K_Q	Dimensionless torque
K_T	Dimensionless thrust
L	Lift force
l	Length
L_1	L_1 norm
L_2	L_2 norm
L_∞	L infinity norm
m	Mass
N	Number of element faces
n	Degrees of freedom, Outward pointing normal
N_p	Total number of nodes
n_p	Rotational speed
P	Surface forces
p	Order of accuracy
p_f	Stress tensor fluid interface
p_s	Stress tensor structural interface
Q	Torque
q	Polynomial, Distributed loading
r	radius
S	Skew, Source term, Surface domain
T	Period, Thrust
t	Time
U	Conserved state
V_A	Advance velocity
V_R	Relative water velocity
x	Displacement
Y	Numerical uncertainty function
AFM	Absolute Formulation Method
AR	Aspect Ratio
BEM	Boundary Element Method
FEM	Finite Element Method

FFT	Fast Fourier Transform
FSI	Fluid Structure Interaction
LE	Leading Edge
MARIN	Maritime Research Institute Netherlands
RANS	Reynolds Averaged Navier Stokes
RBF	Radial Basis Function
TE	Trailing Edge
VLM	Vortice Lattice Method

1 Introduction

For decades marine propeller blades have been manufactured solely using alloys of metals like nickel, aluminium, bronze and stainless steel. However, recent studies have shown that composites as material can have benefits. On the one hand, these claimed benefits are due to the material properties, such as better corrosive characteristics, low magnetic footprint and high strength and stiffness compared to weight. On the other hand, the much larger deformation of the propeller can lead to other advantages compared to normal marine propellers. The flexible propeller adapts to its working conditions, which can lead to better vibration control, higher cavitation inception speeds, and even higher efficiency in off-design conditions.

A challenge of self-adaptive (flexible) propellers is that in the design stage, the deformation can no longer be neglected as in rigid propeller design. The deformation of the propeller influences the flow, and the flow influences the deformation. This interaction is called Fluid-Structure Interaction (FSI) . FSI has to be taken into account in the design stage of a flexible propeller. The design methods used for flexible propellers consist of experiments or numerical solvers. This study is aimed towards the validation of one of the possible numerical solvers.

First, some general information on marine propellers is given. This is followed by a literature review on self-adaptive (flexible) marine propellers. The introduction ends with the objectives and scope of this study.

1.1. Marine Propellers

Propellers are an important part of the propulsion system of ships. Their design depends on parameters like size of the aft ship, velocity of the vessel and wakefield created by the vessel. Some geometrical characteristics of marine propellers, essential for the understanding of this report, are outlined in the next section. In section 1.1.2 the method of expressing the performance of a marine propeller is explained, as these parameters and methods are extensively used in this study.

1.1.1. Geometry

The propeller is connected to the engine shaft of a ship. The root of propeller blades is connected to the hub which is coupled to the shaft. A schematic representation of a hub with one blade is shown in figure 1.1. The orientation is as if looking from the aft of the ship including propeller.

The right hand side of the blade in figure 1.1 is called the leading edge (LE). This is the side of the propeller entering the fluid first. This propeller is therefore rotating clockwise, also called a right-handed propeller. Opposite to the leading edge is the trailing edge (TE) . When looking at a cross section at a constant radius from the hub, the geometry of figure 1.2 is found. In a cross section the leading- and trailing edge are often called nose and tail respectively. The chord (c) is the circular segment connecting nose and tail. Note that in figure 1.2 the cross section is expanded. The midchord is the midpoint of this line, indicated in blue in the figure.

A parameter determined in the design stage of the ship and propeller is the skew. In figures 1.1 and 1.2 the skew of the blade is expressed in two different ways, either in skew angle or distance. The skew angle(θ_S) is

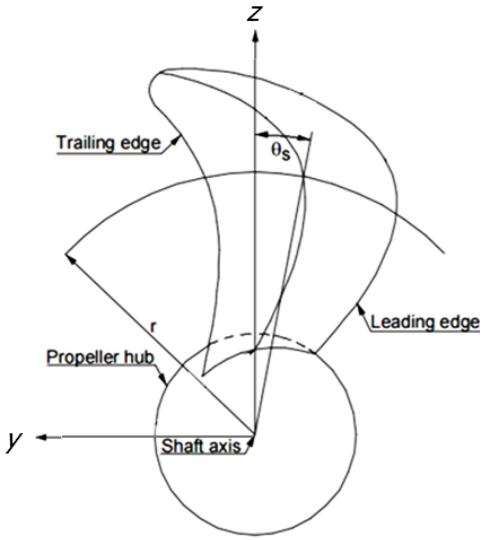

Figure 1.1: Propeller geometry YZ-plane [7]

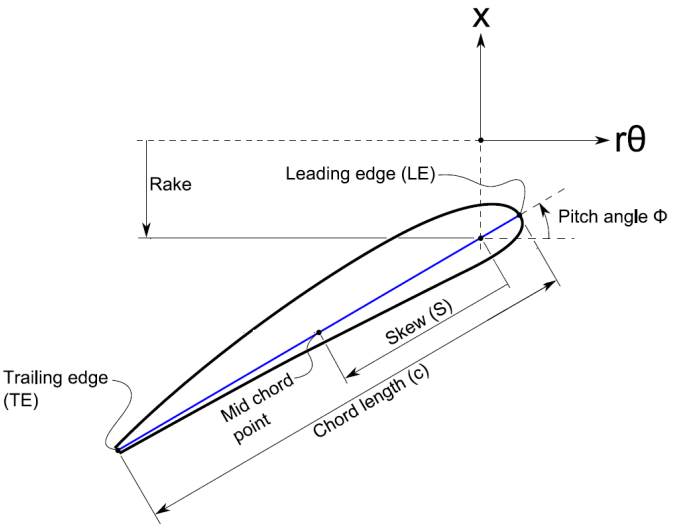

Figure 1.2: Propeller geometry of a slice in the Xθ-plane [32]

depicted in figure 1.1. In figure 1.2 skew is expressed as the distance of the midchord point from the origin of the propeller root, indicated by S. The advantage of highly skewed propellers can be a reduction of propeller induced vibrations on the hull and an increase in cavitation inception speed [8].

The pitch angle (Φ) is the angle in which the propeller blade is turned towards the ship and equals the rotation angle in the xθ-plane in figure 1.1. The distance the propeller travels after one revolution due to its pitch angle is called nominal pitch. However, in reality, the distance travelled by the propeller is less than the nominal pitch, due to slip between propeller and fluid [43]. The pitch angle thus determines the inflow angle of the water onto the blade and thereby the load on the propeller blades. The amount of pitch is determined in the design stage of the ship and its propulsion system, being influenced by the engine speed, requested forward speed and loading on the blades. Another parameter determined in the design stage of the ship and propeller is the rake of the propeller blades. Rake represents the axial shift of the blades from the origin. Rake is shown in figure 1.2. With rake, a larger blade area can be obtained with the aft body of the ship as the limiting factor.

1.1.2. Performance

The flow into the propeller is determined by the flow around the hull. This is called the wakefield. The efficiency and performance of a propeller are often determined in open water. To measure the performance in open water, model tests are performed in a uniform flow, without the influence of the ship hull on the inflow of the propeller blades.

In figure 1.3 a cross section of a propeller blade is shown with relative water velocity (V_R) caused by the forward velocity of the ship, or so called advance velocity (V_A) and the blade rotation speed (n_p)[47]. The suction side of the propeller is located upstream in forward sailing condition. This side has the lowest pressure due to the higher velocity at this side. On the pressure side the largest pressures are found.

The forces related to the flow velocities around the blade are also indicated in figure 1.3. The lift force (L) that is generated, depends on the inflow velocities, angle of attack and the geometry of the blade. A drag force (D) exists due to the fluid resistance on the blade. From this lift- and drag force, the thrust (T) and torque (Q) can be determined.

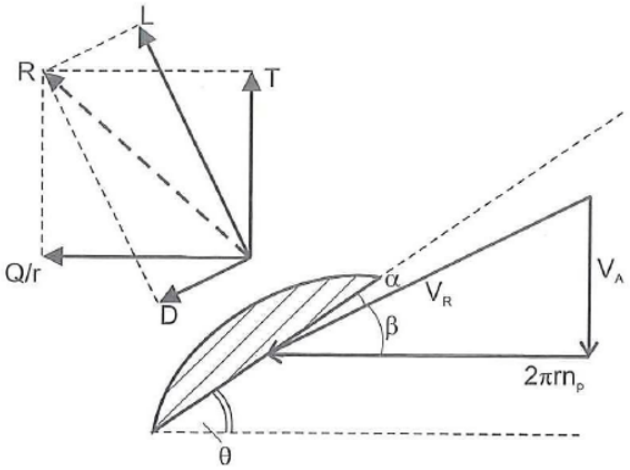

Explanation of the symbols of figure 1.3
- V_A: Advance velocity
- n_p: Blade rotation speed
- V_R: Relative water flow velocity
- α: Angle of attack
- L: Lift force
- D: Drag force
- T: Thrust force
- Q: Torque

Figure 1.3: Cross section of a propeller blade with forces resulting from the inflow- and rotational velocity [47].

The obtained thrust (T) and torque (Q) by model tests in open water can be used to construct a so called open water diagram. In an open water diagram the non-dimensional thrust (K_T), torque (K_Q) and efficiency (η_O) are expressed against the advance ratio J, which is the dimensionless inflow condition. Parameters ρ and D represent the water density and propeller diameter respectively, in the following equations [23] [47],

$$J = \frac{V_A}{n_p D}, \qquad K_T = \frac{T}{\rho n_p^2 D^4}, \quad K_Q = \frac{Q}{\rho n_p^2 D^5}, \qquad \eta_O = \frac{J K_T}{2\pi K_Q} \tag{1.1}$$

Together these parameters are used to construct the open water diagram. The open water diagram is used to show the propeller performance in uniform flow. An example of an open water diagram is shown in figure 1.4.

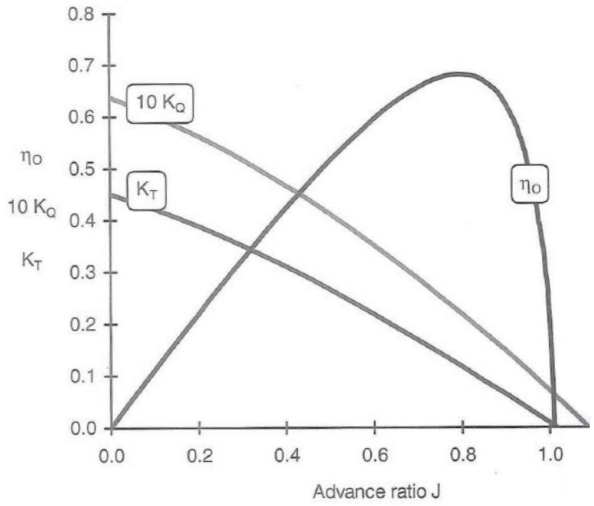

Figure 1.4: Example of an open water diagram [47]

1.2. Flexible Marine Propellers

Self-adaptive marine propellers are made of composites or epoxy rather than metal alloys. Several of the claimed benefits are outlined in the next section. Design methods that are most often used in literature are explained and a literature review on research available on this subject is given.

1.2.1. Claimed Benefits

Benefits due to the material characteristics are that composite has high strength and stiffness combined with low weight [18]. The corrosive characteristics make it a competitive material in the marine industry compared to steel. Next to that, crack nucleation as in metal is prevented by using fibres in composites [5]. For the application on navy vessels, the low magnetic footprint of composite marine propellers is of high importance [27].

The flexibility of the material forces the propeller to adapt its geometry to its working conditions [34]. This results in deformation in response to the hydrodynamic loading, which can lead to reduced cavitation and lower propeller- and hull vibrations [5][18]. In increasing load, the propeller may reduce pitch which can lead to higher efficiency in off-design conditions by benefiting from the usually unwelcome velocity variation in the wakefield behind a ship [34].

1.2.2. Design Methods

When it comes to the design of flexible marine propellers the performance should be determined in relation to geometry changes. Several methods can be used for the determination of deformation and performance of self adaptive propellers. Methods found in literature are:

- Experiments - Thrust, torque and deformation are measured in cavitation tunnels. Often image correlation is used to capture the displacement of the blades. In some literature, cavitation is compared for a flexible propeller and its rigid counterpart.
- Simulations - Using numerical methods to determine the deformations and performance of flexible propellers.

When numerical methods are used for the design, the fluid-structure interaction should be taken into account. The flexibility (stiffness) of the propeller has to be included in the simulation. To be able to simulate FSI, two methods are available, the partitioned- and monolithic approach. The partitioned approach is mostly used for FSI problems, where two separate already existing codes for fluid and structure are used to solve the FSI problem. In the monolithic approach one code is used for the whole FSI problem.

When a partitioned approach is chosen, a Finite Element Method (FEM) is used for the structural solver. For the fluid solver, most often used methods are the Vortice Lattice Method (VLM), Boundary Element Method (BEM) and Reynolds Averaged Navier Stokes (RANS). The differences in the fluid solvers are in the level in which characteristics of the fluid are taken into account and how the equations are discretised. In this study RANS is used towards the validation of BEM, VLM will not further be explained. For the understanding of the next section it should be noted that in BEM the fluid is assumed to be irrotational and viscosity is neglected. In RANS these characteristics are taken into account. Theory of BEM, RANS and FSI will be explained in more detail in chapter 2.

1.2.3. Literature

The literature available on flexible propellers can be roughly divided on the basis of design methods used, the choice of fluid solver in the simulations, the geometry of the propeller, uniform- or non-uniform wake and the parameters that are used for the analysis. Maljaars and Kaminski [30], give a clear overview of research on flexible marine propellers. In the theory chapter 2 an overview is given of the most important literature for this study.

The knowledge gaps identified in the paper of Maljaars and Kaminski [30] for the flexible propeller research are that

- no comparative studies between RANS, BEM, and VLM for the FSI analysis of flexible propellers have been presented in literature so far;
- most of the papers presented results in non-dimensional quantities for flexible propellers, whereas deformations can give more insight in the behavior of the flexible propellers;
- knowledge on cavitation behavior or reduced acoustic signature of flexible propellers is very limited up to now;
- no results have been published that demonstrate the actual efficiency improvement of flexible blades on full scale;
- no investigation in fatigue/strength assessments have been performed.

One project that tries to fill in these knowledge gaps is Greenprop. The Greenprop project has the aim to develop software for the design of flexible propellers for the maritime industry. More specifically,

"Greenprop focuses on the development of a coupling between a Finite Element Method (FEM) software and a Boundary Element Method (BEM) in order to calculate the hydro-elastic response of flexible (composite) propellers in steady and unsteady flow" [28].

When comparing the results for bending- and pitch deformation of the flexible Greenprop propeller, differences were found compared to the model experiments also performed by Greenprop. Several approximations and corrections are made in the BEM-FEM simulations. Therefore, it is not clear where this difference originates. A possible cause for the differences can be the viscous effects not being captured by BEM. To validate the BEM corrections, it is recommended to perform simulations with the same propeller with a solver taking into account viscosity. More information on the Greenprop project is given in the theory chapter 2, together with more literature on flexible marine propellers.

1.3. Objectives

Taking into account the research performed on flexible propellers until now, the knowledge gaps identified by Maljaars and Kaminski [30] and the differences found by Greenprop [28], a clear knowledge gap can be filled by performing coupled RANS-FEM simulations with the GreenProp propeller. By using RANS, viscous effects are taken into account. The RANS-FEM results can be compared with BEM-FEM and experiments performed with the same propeller. Therefore, RANS-FEM is used towards the validation of BEM-FEM.

RANS solver ReFRESCO is used for this study. The objectives of this study can be divided in the actual propeller study using RANS-FEM and the validation of the FSI module of RANS solver ReFRESCO. The possibility to include fluid-structure interaction in ReFRESCO is implemented since 2017 and is therefore relatively new [21]. The code has been tested on several 2D cases only. Therefore, an important part of this study is to validate this module.
The objectives of this study are to,

1. test the performance of the FSI module in ReFRESCO, by performing a benchmark case and compare results to available literature;
2. validate the results of the open water diagram of the rigid propeller in RANS. By comparing to Greenprop results of the experiments and BEM simulations.
3. verify the response of the propeller FE model by comparing to Greenprop FE- and physical model;

4. analyse the response of the epoxy Greenprop propeller in RANS-FEM by observing the thrust, torque, bending and pitch response and comparing to BEM-FEM and experimental results.

First a test case in 2D is performed to become familiar with the software and the FSI module of ReFRESCO. Furthermore, ReFRESCO is validated against available literature, and a sensitivity analysis is performed to investigate the influence of different settings which will be used in the propeller study. After the test case, the actual propeller study is started. A flow diagram of the study is shown in figure 1.5.

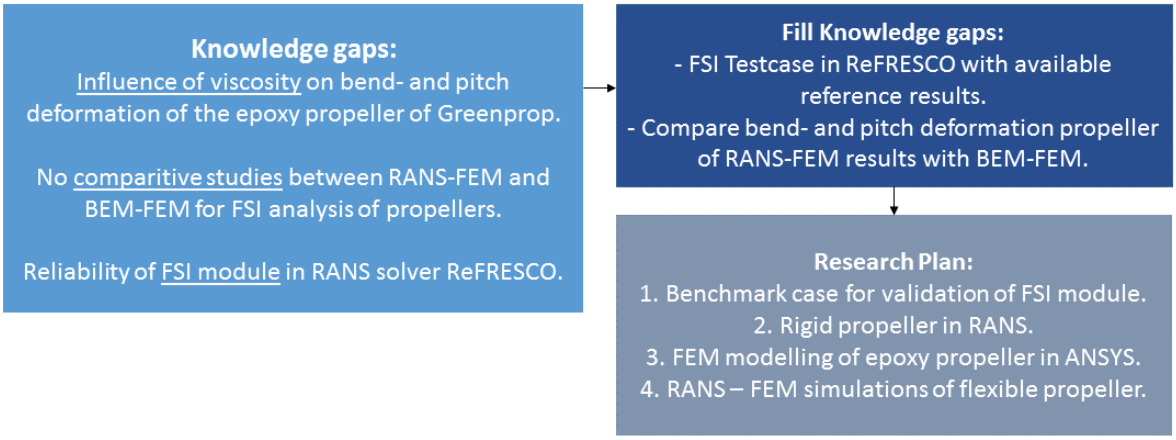

Figure 1.5: Flowdiagram of research

The results of the RANS simulations are compared to the experimental data and to the BEM-FEM simulations. It should be noted that in all the methods modelling errors are made. It is important to get an idea of the measurement and simulation errors before any conclusion is drawn.

1.4. Scope

Within the scope of this study simulations are performed with the propeller of Greenprop, using RANS solver ReFRESCO coupled to FEM. The epoxy propeller is used. This propeller is the most flexible one used by Greenprop, leading to the highest deformation, compared to the composite propellers. Besides that, the FEM modelling of this propeller is relatively simple as the propeller can be assumed isotropic. The bronze (rigid) propeller is used to verify the open water diagram. Simulations are performed in a uniform wakefield, as Greenprop results are available for these conditions only.

For the propeller study, simulations in the same conditions as the Greenprop simulations and experiments are performed. Greenprop tested advance ratios in the range of 0.369 to 0.851. To reduce the amount of simulations in this study it is chosen to focus on three conditions as performed by Greenprop. These conditions have a varying advance ratio, and therefore angle of attack on the propeller blade. Advance ratios of the three conditions are J= 0.369, 0.512 and 0.849. These were chosen to give a broad view on the effect of RANS compared to BEM in the range of advance ratios tested by Greenprop. It is expected that by using RANS a better resemblance is found with the experimental data compared to BEM. Especially in regions where there is a large influence of viscous effects. Viscous effects include flow separation, boundary layer development and tip vortex dynamics. These mostly appear in conditions with large angles of attack on the blade. This corresponds to low advance ratios as becomes clear from figure 1.3.

1.5. Overview Report

Before the actual study is started, a theoretical background is given in chapter 2 on solving methods of fluid and structure, numerical methods and fluid structure interaction. After that the benchmark case is discussed. This benchmark case is discussed in chapter 3. This benchmark case ends with a sensitivity study on proportional damping, timestep and RBF radius.

The propeller part of this research is divided in a rigid- and a flexible propeller part. In figure 1.6, a flow diagram of the propeller part is shown. In chapter 4, the rigid part of the propeller simulations is discussed. The flexible part can be found in chapter 4. In both chapters the discretisation of fluid and structure are discussed together with results of rigid and flexible propeller simulations. Chapter 6 contains the overall conclusion and recommendations of this study.

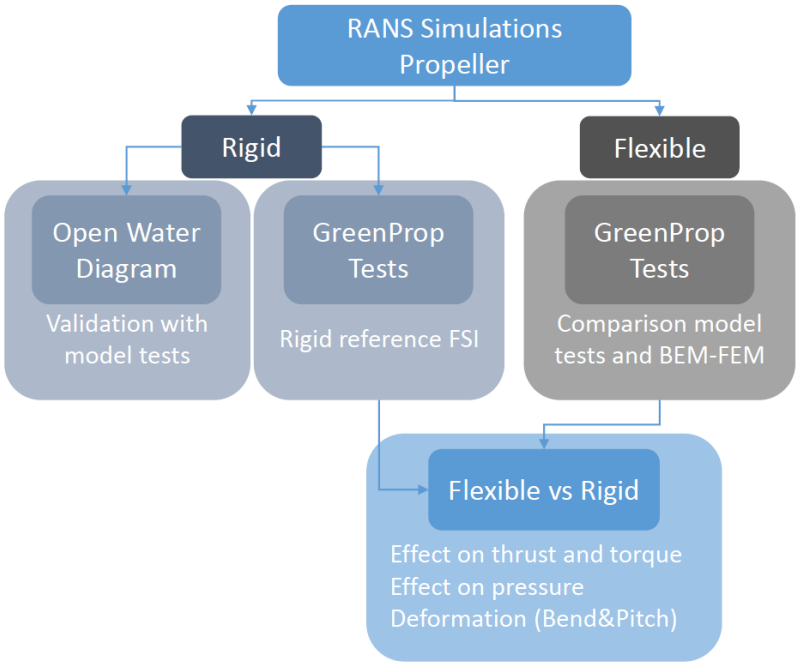

Figure 1.6: Plan propeller study simulations and comparisons

2

Theoretical Background

In this chapter the theoretical background is given necessary for the understanding of the benchmark- and propeller case chapters. Started is with literature on flexible marine propellers. Followed by the theory on fluid- and structure and the solvers used for fluid and structure in this study. The chapter ends with the description of fluid-structure interaction and how it is implemented in the solver.

2.1. Literature Flexible Propellers

In the introduction it was explained that the literature can be roughly divided in the basis of design methods used, the choice of fluid solver in the simulations, the geometry of the propeller, uniform- or non-uniform wake and the parameters that are used for the analysis. Some literature is summarised in this section.

In literature, whenever simulations are performed, most often a partitioned approach is used, with a separate fluid- and structural solver. The structural model of the propellers used in simulations, are mostly constructed out of shell- or solid elements. When looking at the fluid solver used in literature, most of the available research papers use either a BEM solver coupled to FEM (BEM-FEM) or a RANS solver coupled to FEM (RANS-FEM). In most cases BEM was chosen for computational time and cost reasons rather than accuracy. Reasons for choosing RANS rather than BEM were that BEM assumes the fluid to be inviscid, while the propeller operates in a viscous flow [18]. Especially for conditions where the viscous effects are significant a RANS solver will perform better.

The geometry of the propellers used in literature mostly have large skew [18] [34] [5]. Especially for displacement of the tip, the twist of the blade high skew is wanted. Maljaars and Dekker [29] showed that skew angle has a large influence on the hydro-elastic response: *"The movement of the thrust load causes, especially in case of highly skewed propellers, a larger de-pitching moment. Based on these results it can be concluded that the skew angle has a pronounced effect on the hydro-elastic response of a flexible propeller."*

In this study RANS-FEM is used, therefore some literature on RANS-FEM of flexible propellers is further outlined. Ducoin [13] used RANS-FEM for the modelling of a deformable hydrofoil. Simulations were compared to experimental tests performed in a tunnel. It was concluded that the coupled method was accurate for this case and ready to be implemented in more difficult marine structures like propellers and ship stabilizers. Mulcahy [34] used a highly skewed propeller with five blades. Simulations of the rigid propeller were compared to available literature. K_T and K_Q showed higher values when compared to literature. Then, a hydrofoil was modelled to check the convergence of the RANS-FEM coupling. After this a design was made for a flexible propeller, with the aim of producing the same thrust in the design condition. RANS-FEM coupling was used, but no information about the coupling of the non-matching grids was presented. Different ply arrangements of the composites were considered. It was concluded that to obtain the largest deformation, the propeller should be thin and highly skewed. The selection of appropriate composite materials should be further investigated. In He et al[18], a highly skewed propeller was used with seven blades. Blades were made out of carbon-fibre reinforced composites. The response in a non-uniform wake was analysed. Tip node displacement, thrust- and torque coefficients and maximum von Mises stress were monitored during

simulations. It was concluded that the stacking scheme of the fibres has a large influence on the loading of the blade. The harmonic forces and moments of the composite blade were much smaller compared to the metal blade.

Raj and Reddy [35], investigated the cavitation inception of different ply arrangements of composite propellers compared to its rigid counterpart. FLUENT and ANSYS were used for the CFD-FEM coupling. In this study non-matching grids were used and no information on interpolation schemes was presented. They found a slightly larger operating range of advance ratio J without cavitation for the flexible propellers. It must be noted that in this paper a 4-bladed propeller was used with moderate skew and large blade areas compared to other propellers found in literature. Taketani [42] compared cavitation tunnel tests to RANS-FEM simulations, using STAR-CCM+ for the fluid modelling and ABAQUS for the FEM modelling. However, no information about the interpolation scheme was given. Results from the cavitation tunnel showed lower thrust and torque for the composite propellers. It was found that deformation has an optimum level, when thrust dropped below a certain level the propeller efficiency decreases. Cavitation lowered for the composite propeller compared to its aluminium counterpart. However, the method of capturing the deformations showed some inaccuracies.

Parameters that are used for comparison to rigid counterpart propellers or performance prediction are mostly non-dimensional thrust and torque, (tip) displacement and pressure. Maljaars [29] concluded that thrust is not the right quantity to qualify the accuracy of the results, since the difference in thrust due to the flexibility has the same order of magnitude as the inaccuracy of BEM. For experimental tests, digital image correlation revealed to be a promising measuring technique.

This study is on the validation of RANS-FEM towards BEM-FEM used by Greenprop. In the Greenprop project BEM solver Procal was used. BEM-FEM Simulations and model tests are performed in a cavitation tunnel by Greenprop for one rigid and three flexible propellers (one full epoxy and two composite). In the BEM solver three different corrections were applied [28]. A minimum pressure coefficient to lower the suction peak that is overestimated by BEM. This correction is applied to improve the fit of the calculated torque closer to measured torque. The second correction is a pressure correction at the tip. As there is a wing tip vortex, pressures at the tip will be zero. This tip vortex is not captured by BEM making it necessary to apply a correction. The third correction is due to the fact that BEM does not take into account viscosity. A viscous correction is implemented in BEM solver Procal. Simulations were performed with different values for these corrections.

2.2. Fluid

In the introduction it was explained that RANS solver ReFRESCO is used for the fluid part. In this section some background knowledge is given on the Navier Stokes equations behind RANS, including assumptions and simplifications made to these equations. Furthermore, ReFRESCO is introduced. Only the most important methods and settings of ReFRESCO for the understanding of the report are discussed here. For more background knowledge on ReFRESCO it is referred to the ReFRESCO website of MARIN[31]. The last subsection consists of the numerical errors occurring in simulations and methods to quantify these numerical errors.

2.2.1. Navier-Stokes Equations

The conservation laws describe the state of a fixed volume over time. The conservation of mass states that the amount of incompressible fluid mass in a certain volume remains the same[2]. Newton's second law states that the change of momentum of a volume equals the total force on the volume [45], which leads to the conservation of momentum equations. The energy equation describes the change of internal energy, while keeping the total amount the same. The general conservation law can be described by using integrals over the volume domain (Ω) and surface of the domain(S)[17],

$$\frac{d}{dt}\int_{\Omega} U d\Omega + \int_{S} F(U)\cdot n dS = \int_{\Omega} S(U,t) d\Omega \tag{2.1}$$

In this equation U is the conserved state, F the flux of the conserved state, n the outward pointing unit normal to the surface and S the source term[17]. The Navier-Stokes equations describe the fluid behaviour and consist of the conservation of mass and momentum equations, equations 2.2a and 2.2b, respectively[2].

$$\frac{d}{dt}\int_{\Omega} \rho d\Omega + \int_{S} (\rho \vec{v})\cdot \vec{n} dS = 0 \tag{2.2a}$$

$$\frac{d}{dt}\int_{\Omega} \rho v_i d\Omega + \int_{S} \rho v_i \vec{v}\cdot \vec{n} dS = \int_{S} T\cdot \vec{n} dS + \int_{\Omega} \rho f_i d\Omega \tag{2.2b}$$

with P the surface forces and f_i the body forces [2]. In this study it is assumed is that the fluid is isothermal, therefore the energy equations are left out of the Navier Stokes equations. Next to the assumption of the fluid being isothermal, other assumptions and simplifications of the Navier-Stokes equations are possible. These are outlined in the next subsection.

Assumptions and simplifications

Different assumptions lead to simplifications of the Navier-Stokes equations. The mathematical models used in different fluid solvers differ in which simplifications are applied. Some of these simplifications are shown in figure 2.1.

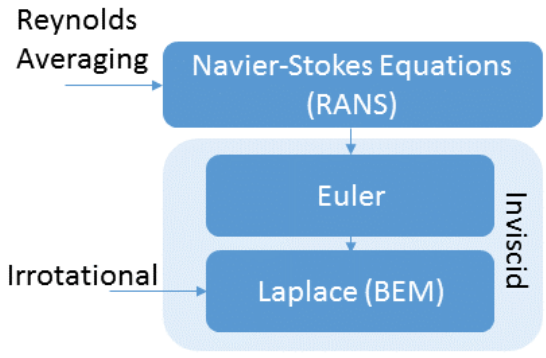

- Reynolds Averaging: This is used to separate turbulent fluctuations from the mean flow. The flow variables of the Navier Stokes are divided in a fluctuating and averaging part [4]. The effect of the turbulent fluctuations are accounted for through turbulence models [45].
- Steady state: For steady state the state of the fluid does not change in time. The time derivatives in the conservation equations can be left out.

Figure 2.1: Navier-Stokes and assumptions

- Incompressible: For incompressible fluids the density remains the same over time. The $\frac{\partial \rho}{\partial t}$ term can be left out of the Navier Stokes equations.

- Inviscid: The flow field can be divided in two regions. One region is called the boundary layer where friction is important. The region outside the boundary layer is frictionless (potential flow) [1]. When the fluid is said to be inviscid, the viscous stresses can be neglected and the so called Euler equations are obtained.

- Irrotational: The velocity field of the fluid particles is assumed to have no rotational directions. When the fluid is assumed both inviscid and irrotational the Laplace equations are obtained. In a Boundary Element Method (BEM) the Laplace equations are solved.

2.2.2. Numerical Methods

When a fluid problem is solved numerically, a discrete representation of the fluid domain is obtained by dividing in either volumes, elements or panels depending on the solvers used. Different numerical methods are known to solve the fluid equations. All with different accuracy and level in which properties are taken into account. In the introduction, section 1.2.2, it was explained that the RANS solver is used in this study which is compared to BEM. The assumptions made in these two solvers were outlined in figure 2.1.

RANS solver ReFRESCO

ReFRESCO stands for Reliable & Fast RANS Equations (solver for) Ships, Cavitation and Offshore. It solves the multi-phase unsteady incompressible RANS equations. The pressure velocity coupling is achieved using a SIMPLE segregated method. ReFRESCO is capable of simulating moving, deforming grids and includes several turbulence models. ReFRESCO runs on Linux workstations and HPC clusters. The code is parallelised using MPI and subdomain decomposition [31].

A typical solving process in ReFRESCO consists of three iteration loops, the time loop, outer loop and inner loop [4]. Within a time step the outerloop is solved. Within the outerloop all equations are solved in the inner loops. These consists of the momentum equations, pressure correction equation and velocity field and turbulence model. Iterative methods are used to solve these large systems of equations. An iterative method is explained by Wesseling [45]: "An iterative method generates successive approximations $y^1, y^2, ...$ If $\lim y^i = y$, for $i \to \infty$, this method is said to converge. A number of iterations i is needed to obtain a sufficiently accurate solution y[45]." The convergence criteria govern the accuracy of the solution. One of the iterative methods is the velocity pressure coupling. In the ReFRESCO theory report [4] this coupling is described by, *"Velocity- pressure coupling is achieved by either solving the coupled mass-momentum system directly or by using a segregated SIMPLE pressure correction method. All other equations are treated in a segregated manner, which means that the equations for a certain variable are solved for all cells. Then the equations for the next variable are solved for all cells etc [4]."*

Several turbulence models are implemented in ReFRESCO. Two of them are used in this study, namely the $k-\omega$ (SST 2003) and $k-\sqrt{k}L$ model. Both models are eddy-viscosity based turbulence models. In Rijpkema et al [38] these two turbulence models were used in a propeller case as well. It is explained that the $k-\omega$ SST model is a combination of the $k-\omega$ model in the viscous sub layer and logarithmic part and $k-\epsilon$ models in the wake region of the boundary layer. The $k-\sqrt{k}L$ is a scale adaptive simulation model, being able to recognise and adjust to resolved scales in the simulation. This model is more applicable in unsteady simulations and has better iterative convergence. In the results of Rijpkema et al [38], it is described that the differences in performance characteristics between $k-\omega$ SST model and $k-\sqrt{k}L$ were within 0.5%. The iterative convergence of the $k-\sqrt{k}L$ model improved compared to the $k-\omega$ model. More information on turbulence models can be found in the ReFRESCO theory manual [4].

In ReFRESCO the possibility of a moving grid method is implemented. The moving grid method is used in the propeller study. In this method several options are available to simulate the flow around the propeller. In this study the absolute formulation (AFM) is used in which the RANS equations are solved in the moving reference frame but written in terms of absolute or inertial reference frame quantities[4].

Discretisation

In each grid cell the conservation laws as described in section 2.2.1 are defined. The mesh is an important part. The level of refinement that is needed is dependent on the method used. When viscosity is taken into account a boundary layer around an object is present. To capture this phenomenon the mesh around the

object should be sufficiently fine to resolve the high gradients of the flow [45]. The y+ value should be below 1 to resolve the flow. For y+ below 50 wall functions are used for Re of around 10^6.

A QUICK scheme for the convective flux discretisation is the most accurate. This scheme is second order accurate, leading to the discretisation error becoming four times smaller when the grid is refined two times. This leads to a grid independent solution. The central differencing scheme is second order as well. A blending factor of one indicates that the central differencing scheme is used and a blending factor of zero equals the use of the first order upwind scheme. For a full description of these schemes, it is referred to the ReFRESCO theory manual[4].

Next to the spatial discretisation of the grid, time discretisation is used to solve the problem over time. In the benchmark case and rigid propeller case steady simulations are performed. In these simulations the time-derivative is zero and only one single time step is calculated [4]. For the unsteady FSI simulations the second order backward difference method is used. This method is further outlined in section 2.4.

2.2.3. Numerical errors

Due to the discrete presentation in panels, elements or volumes the numerical approach introduces errors. The errors consist of round off-, modelling-, discretisation- and iterative errors. Round-off errors are related to the finite precision of computers[14]. It is assumed that the round-off errors are negligible compared to the other errors. The modelling errors are introduced due to the mathematical model used for the fluid flow phenomena. These modelling errors are tried to be kept small by choosing correct models and settings for the flow behaviour that is expected. The iterative error is introduced by solving the partial differential equations iteratively. This error is explained in the next subsection. The discretisation error is due to the discrete representation of the fluid grid. This error is explained in the last subsection.

Iterative Errors

The iterative error is mostly monitored by residuals, representing the part of the equations that is left after an iteration loop. The iterative error should be several orders lower than the discretisation error[15]. The iterative error can be expressed by the L_1, L_2 or L_∞ norm, by using norms of the change in solution from one iteration to the other [14]. The L_∞ and L_2 are used in this study and defined by,

$$L_\infty(\triangle\phi) = Max(|\triangle\phi_i|) \qquad 1 \leq i \leq N_p \tag{2.3}$$

$$L_2(\triangle\phi) = \sqrt{\frac{\sum_{i=1}^{N_p}(|\triangle\phi_i|)^2}{N_p}} \tag{2.4}$$

where N_p is the total number of nodes of a given grid and $\triangle\phi$ the local change of a flow quantity.

Discretisation Errors

Generally, the discretisation error can be reduced by introducing more elements or volumes. When constructing the fluid grid, the jump estimators can indicate whether refinement is needed in the grid. The jump estimators measure variation in results between two consecutive cell centres. If the step between two cell centres is too large the mesh should be refined at that location. During ReFRESCO simulations, the jump estimators can be monitored. The error estimators used in this method are [46],

$$J_e = \sqrt{\frac{e_e^2}{2L_2(\triangle\phi)}} \tag{2.5}$$

With:
e_e = local error of an element $e_e^2 = \frac{\nabla}{4N}\sum_{k=1}^{N}(\phi_L - \phi_R)^2$.
$L_2(\triangle\phi)$ = L_2 norm of a scalar variable ϕ.
N = number of element faces.
∇ = Volume of an element.
ϕ_L,ϕ_R = Left and right values of a face of a volume element.

For the evaluation of the discretisation error the method of Eça and Hoekstra [14] is used in this study. In this method grids are coarsened or refined to obtain several geometrically similar grids that only differ in cell size and therefore in number of elements. The order of accuracy (p) is found by:

$$\phi_i - \phi_o = \alpha h_i^p \tag{2.6}$$

with ϕ_i the solution at grid node i, ϕ_o the estimated exact solution, a constant α, grid size h_i and order of accuracy p. The unknowns can be determined when there are at least three or more grids available. ϕ_o, α and p are obtained with a least squares fit of the data, minimizing the function Y,

$$Y(\phi_o, \alpha, p) = \sqrt{\sum_{i=1} (\phi_i - (\phi_o + \alpha h_i^p))^2} \tag{2.7}$$

For a full description of this method, it is referred to the paper of Eça and Hoekstra [14].

2.3. Structure

The elastic modulus and moment of inertia are important parameters describing the stiffness of the material of the structure. This stiffness, together with the mass and damping of the structure is used to describe the dynamic behaviour, which can be expressed by the equations of motion. The equations of motion and Rayleigh damping are described in the next sections. In the FSI part of this study, FEM is used for the structural model, therefore, FEM is described in the last subsection.

2.3.1. Equations of Motion

The dynamic behaviour of a structure can be described by using the mass (m), damping (c) and stiffness (k) of the structure. When a structure, with one degree of freedom, is loaded with force F, the acceleration ($\ddot{x}$), velocity ($\dot{x}$) and displacement (x) of the structure can be derived from the equations of motion,

$$m\ddot{x} + c\dot{x} + kx = F \tag{2.8}$$

When the system of n degrees of freedom is left vibrating after an initial disturbance by an impulsive force F the frequencies at which it vibrates are called the eigenfrequencies. The system has n eigenfrequencies and corresponding modes, which describe the motion of the system at each frequency[36]. The eigenfrequencies and corresponding modes can be derived by mass normalizing the equations of motion,

$$\ddot{x} + \frac{k}{m}x = \frac{F}{m}$$

The natural frequency is then obtained by solving,

$$\omega_n = \sqrt{\frac{k}{m}}$$

For larger structures, with more degrees of freedom, the mass, damping and stiffness are described in matrices, $[M]$, $[C]$ and $[K]$, respectively. The acceleration, velocity and displacement are vectors with length corresponding to the number of degrees of freedom, $\{\ddot{x}\}$, $\{\dot{x}\}$ and $\{x\}$, respectively. The equations of motion are then,

$$[M]\{\ddot{x}\} + [C]\{\dot{x}\} + [K]\{x\} = \{F\} \tag{2.9}$$

for large systems these equations need to be solved numerically. For the determination of the eigenfrequencies and modes modal analysis can be used, in which the displacement of the masses are expressed as a linear combination of the normal modes of the system [36].

A system with a discrete number of degrees of freedom is called a discrete system and a system with infinite number of degrees of freedom is called a continuous system. Most of the time, continuous systems are treated as discrete systems [36]. For the benchmark case the derivation of the eigenfrequency is determined using a continuous system for the plate. This method is further described. A beam is chosen, because this can be used for the Benchmark case described in chapter 3. The equations of motion for a free vibration of a uniform beam can be described by [36],

$$EI\frac{\partial^4 w}{\partial x^4}(x,t) + \rho A\frac{\partial^2 w}{\partial t^2}(x,t) = 0 \tag{2.10}$$

A solution of the form $w(x,t) = W(x)T(t)$ is chosen. When this solution for $w(x,t)$ is filled in 2.10 the following expression is found:

$$\frac{c^2}{W(x)}\frac{\partial^4 W(x)}{\partial x^4} = -\frac{1}{T(t)}\frac{\partial^2 T(t)}{dt^2} = \omega_n^2 \tag{2.11}$$

$$\frac{\partial^4 W(x)}{\partial x^4} - \alpha_n^4 W(x) = 0 \qquad \frac{\partial^2 T(t)}{dt^2} + \omega_n^2 T(t) = 0 \tag{2.12}$$

with $\alpha_n^4 = \frac{\omega_n^2}{c^2} = \frac{\rho A \omega_m^2}{EI}$. The natural frequency can be derived from this equation by $\omega_n = (\alpha_n L)^2 \sqrt{\frac{EI}{\rho A l^4}}$.
For W(x) a solution in the form of $W(x) = Ce^{sx}$ can be found with $s^4 - \alpha_n^4 = 0$. This leads to $W(x) = C1e^{\alpha_n x} + C2e^{-\alpha_n x} + C3e^{i\alpha_n x} + C4e^{-i\alpha_n x}$. Constants C1, C2,C3, C4 and α_n can be derived from the boundary conditions. When a beam is used that is clamped at one end and free at the other end. The following boundary conditions can be identified. At the clamped end the deflection ($W(x)$) and slope ($\frac{\partial w}{\partial x}$) are zero. At the free end the bending moment ($EI\frac{\partial^2 w}{\partial x^2}$) is zero. If these boundary conditions are inserted in the equation of W(x) α_n is obtained which leads to the equation for the natural frequency. For common boundary conditions these values for $\alpha_n l$ can be found in Rao [36], for the first four eigenmodes of a fixed-free beam,

$$\alpha_n l = 1.8751, 4.6941, 7.8548, 10.9955, .. \quad \text{for} \quad n = 1,2,3,4,.. \tag{2.13}$$

2.3.2. Damping

Damping that influences the structural dynamics can be categorized into viscous damping, hysteresis damping, coulomb damping and radiation damping [16]. For this study, viscous damping will have the most effect. Rao [36], clearly describes viscous damping: *"When mechanical systems vibrate in a fluid medium such as air, gas, water or oil, the resistance offered by the fluid to the moving body causes energy to be dissipated. In this case, the amount of dissipated energy depends on many factors, such as the size and shape of the vibrating body, the viscosity of the fluid, the frequency of the vibration and the velocity of the vibrating body. In viscous damping, the damping force is proportional to the velocity of the vibrating body[36]."*

Structural damping can be added to the system by Rayleigh damping. The damping matrix is then composed by a fraction of the mass and stiffness matrix as in equation 2.14. The coefficients α and β are dependent on the frequency range and desired damping coefficient [6].

$$[C] = \alpha[M] + \beta[K] \tag{2.14}$$

Critical damping is the lowest damping for which the oscillatory movement is totally damped, so no oscillations occur. The fraction of this critical damping is called the damping coefficient. If Rayleigh damping is to be applied for a steady system, for instance 5 % critical damping is found. Then α and β can be determined using the frequency range (ω_1, ω_m) and selected damping ratios (ζ_1, ζ_m). β is obtained using equation 2.15, α by evaluating equation 2.16.

$$\beta = \frac{2\zeta_1\omega_1 - 2\zeta_m\omega_m}{\omega_1^2 - \omega_m^2} \tag{2.15}$$

$$2\zeta_1\omega_1 = \alpha + \beta\omega_1^2 \tag{2.16}$$

2.3.3. Numerical Methods

To solve the structural response Finite Element Methods (FEM) can be used. The structural model is then discretised in a finite number of elements. Different types of elements are available dependent on the type of problem. The elements differ in degrees of freedom and physics involved. In this study only solid elements are used, because the fluid structure interaction module of ReFRESCO can only include solid elements.

The elements that are used in this study are linear solid elements (SOLID185) and quadratic solid elements (SOLID186). SOLID185 is a 3D solid element having eight nodes and three translational degrees of freedom at each node. SOLID186 is its higher order version, that contains 20 nodes and exhibits quadratic displacement behaviour. Both elements support plasticity, hyperelasticity, creep, stress stiffening, large deflection and large strain capabilities [40]. It is important to know the behaviour of the structure before an element type is chosen. For structures where bending is dominant, shear locking can occur when using linear solid elements, as the curvature is not modelled accurately [16]. For a description of this phenomenon it

is referred to section 2.3.3. When using linear solid elements, more than one element through bending direction should be used to avoid shear locking.

In this study it is assumed that a linear elastic behaviour of the structures (benchmark and propeller) suffices. This means that deformations are assumed to be small and that the deformation is linear with the force applied [40]. For geometrically non-linear behaviour this does not hold. The structure responds non-linearly to the large deformations. Maljaars [28], showed that it was valid for the Greenprop propeller to assume linear elastic behaviour.

2.4. Fluid Structure Interaction

In the introduction it was explained that interaction between the fluid and structure should be taken into account for flexible propellers. In this chapter the physics are explained together with different approaches used to solve FSI problems.

2.4.1. General FSI

The equation of motion for an object with fluid structure interaction can be generally expressed as:

$$[M]\ddot{x} + [C]\dot{x} + [K]x = F(x) \tag{2.17}$$

The left side of this expression is governed by the structural characteristics: mass [M], damping [C] and stiffness [K], whereas the right hand side represents fluid loading on the structure which is partly dependent on the deformation x of the structure.

2.4.2. Solving of FSI

As explained in the introduction, different approaches are used to solve the FSI problem, e.g. a monolithic approach where the whole system is solved using the same software or a partitioned approach where fluid and structure problems are solved in separate programs.

In a monolithic approach the fluid and structure equations are solved simultaneously, using a single solver. This increases the stability of the simulation because their mutual influence is evaluated directly [12]. In a partitioned approach there is no flow change when the structural response is calculated. This introduces an extra error next to the numerical errors in the simulations. A coupling mechanism is necessary to evaluate the interaction of the two solvers. The partitioned approach is mostly used for FSI simulations. The biggest advantage of this approach is that existing and optimized software can be used for the fluid and structural problem.

When a partitioned approach is used, two discretisations are necessary, one for the fluid solver and one for the structural solver. For these grids there are two possibilities. One option is to use identical grids for fluid and structure leading to a point matching configuration. Another option is to use different grids for structure and fluid. This often occurs as the fluid grid normally requires a finer mesh than the structure. By using two different resolutions the computational time can be drastically reduced. A drawback of the partitioned approach is that the equations are not solved simultaneously in time due to the different solvers [2].

If there are two grids with different resolutions, an interpolation scheme is necessary to ensure correct displacement of the fluid grid from the structural response and correct loading transfer from fluid to structure interface. An interface coupling method is used for this purpose which is explained later on in detail. The fluid grid is remeshed using the result of the last time step. This is done by iterating until a converged solution is obtained [21]. A typical solving routine of a partitioned FSI problem is shown in figure 2.2.

2.4.3. FSI in ReFRESCO

The FSI module of ReFRESCO was recently implemented by Jongsma and Windt [20]. In this module, the equations of motion is solved by taking into account the fluid load, solved by ReFRESCO and the deformation of the structure. Damping can be added through Rayleigh damping. A full description of the implementation of FSI in ReFRESCO is found in the report of Jongsma[21]. Some of the equations and methods are outlined for the understanding of this study.

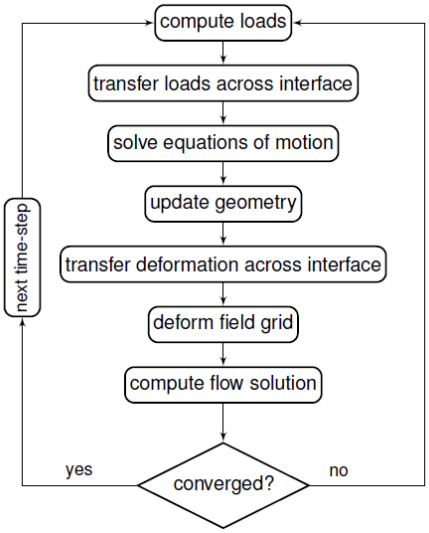

Figure 2.2: Overview of iteration scheme of one timestep [21]

In the FSI module of ReFRESCO the damping of the structure is neglected. The equations of motion of equation 2.17 is then,

$$[M]\ddot{x} + [K]x = F(x) \tag{2.18}$$

the $[M]$ and $[K]$ matrices of the structural solid model are used for the evaluation of the equations of motion. These matrices only need to be derived and included once, as they do not change during simulation. Three files are used as output from ANSYS. The .full (containing the [K] and [M] matrices), .rst (geometry) and the .intnodes file (containing the coordinates of the nodes on the interface of the structure). The flow diagram of the procedure during one time step of FSI in ReFRESCO is illustrated in figure 2.2.

To be able to solve a set of first order differential equations, the equations of motion are defined as:

$$\frac{d\mathbf{Q}}{dt} + A\mathbf{Q} = \begin{pmatrix}\mathbf{F}\\0\end{pmatrix}, \quad \text{with:} \quad \mathbf{Q} = \begin{pmatrix}M\dot{u}\\u\end{pmatrix} \quad \text{and} \quad A = \begin{bmatrix}0 & K\\-M^{-1} & 0\end{bmatrix} \tag{2.19}$$

To solve this set of equations numerically in time, different solution schemes can be used with $f(Q,t) = \begin{pmatrix}F\\0\end{pmatrix} - AQ$ [21]. Three solution schemes are incorporated in the FSI module, the Cranck-Nicholson, second order backward-difference scheme and the Newmark time integration. In this study the second order backward-difference, or so-called three-time level is used. Defined by,

$$\frac{3Q^{n+1} - 4Q^n + Q^{n-1}}{2\triangle t} = f(Q^{n+1}, t^{n+1}) \tag{2.20}$$

Two non-identical grids are used for the fluid and structure. An interpolation is needed for the transfer of load across the fluid-structure interface. This coupling method is explained in the next section. This interpolation is also used in the grid deform method, which governs the deformation of the fluid grid after the deformation of the structure is transferred across the interface.

2.4.4. Interface Coupling

The coupling of deformation and loads across the fluid structure interface is implemented in the FSI module of ReFRESCO by Jongsma [21]. In that report a description of the method and implementation can be found. However, for the completeness of this report, the method is also described here.

At the interface of the fluid and structure kinematic- and dynamic boundary conditions can be described[10], these conditions on the continuous interface Γ are defined by,

$$\mathbf{u}_f = \mathbf{u}_s \quad \text{on} \quad \Gamma \tag{2.21a}$$

$$p_s \mathbf{n}_s = p_f \mathbf{n}_f \quad \text{on} \quad \Gamma \tag{2.21b}$$

with $\mathbf{u}_f$ and $\mathbf{u}_s$ the displacements, p_s and p_f the stress tensors and $\mathbf{n}_s$ and $\mathbf{n}_f$ the outward normal of the structure and fluid interface. These boundary conditions state that either the displacement fields of fluid and structure interface are equal. The other states that the pressure on the fluid side of the interface is in equilibrium with the structural side. For the discrete representation and derivation of the coupling equations one is referred to appendix A. A conservative coupling approach is obtained if the energy is conserved across the fluid-structure interface[10]. This is the case when,

$$\int_{\Gamma f} \mathbf{u}_f \cdot p_f \mathbf{n}_f ds = \int_{\Gamma s} \mathbf{u}_s \cdot p_s \mathbf{n}_s ds \tag{2.22}$$

In the FSI module of ReFRESCO the total amount of energy, energy change and energy loss are monitored during a time step. For the creation of the interpolation matrix different methods can be used. In this study an RBF interpolation is used which is now further outlined.

Radial Basis Function Interpolation

In de Boer et al [10], the Radial Basis Function (RBF) interpolation is described as the approximation of a quantity transferred from mesh A to mesh B, by a sum of basis functions both at the interface of A and B. A typical interpolation function is,

$$\mathbf{w}_i(x) = \sum_{j=1}^{n_A} \gamma_j \phi(|x - x_{Aj}|) + q(x) \quad i = \{A, B\}, \quad \mathbf{w} = \{\mathbf{u}, p\mathbf{n}\} \tag{2.23}$$

in which ϕ is a radial basis function and x_{Aj} the nodes at interface of grid A at which the values are known. Interpolation constant γ and polynomial $q(x)$ can be obtained by satisfying,

$$\mathbf{w}_A(x_{Aj}) = \mathbf{W}_{Aj} \tag{2.24a}$$

$$\sum_{j=1}^{n_A} \gamma_j h(\mathbf{x}_{Aj}) = 0 \tag{2.24b}$$

with $\mathbf{W}_A$ the discrete values of $\mathbf{w}_A$ at the interface of mesh A and for all polynomials h with a degree less or equal than that of polynomial q[9]. The minimal degree of polynomial q depends on the chosen RBF function [10]. The values of mesh A and mesh B can be written in matrix form as,

$$\mathbf{W}_B = \begin{bmatrix} \Phi_{AB} & Q_B \end{bmatrix} \begin{bmatrix} \Phi_{AA} & Q_A \\ Q_A^T & 0 \end{bmatrix}^{-1} \begin{bmatrix} \mathbf{W}_A \\ 0 \end{bmatrix} \tag{2.25}$$

in which Φ_{AB} is the matrix containing the evaluation of the basis function $\phi_{AiBj} = \phi(||\mathbf{x}_A i - \mathbf{x}_{Bj}||)$ and Φ_{AA} the basis function of $\phi_{AiAj} = \phi(||\mathbf{x}_{Ai} - \mathbf{x}_{Aj}||)$, Q_B and Q_A are row vectors containing $\begin{bmatrix} 1 & x_{Aj,Bj} & y_{Aj,Bj} & z_{Aj,Bj} \end{bmatrix}$. The first two matrices of equation 2.25 form the transformation matrix. The number of rows and columns of this matrix is equal to the number of fluid or structure points on the interface[10].

There are several RBF functions that can be chosen. In the FSI module of ReFRESCO the C^2 function with compact support is used. Compact support means that only the mesh nodes inside a spere with radius r around a centre are influenced by the movement of this centre[9]. In the FSI module of ReFRESCO the interpolation works as follows, *"The subroutine starts by determining the communication that must be performed. For this purpose, a loop is performed over the vertices of the CFD interface nodes. Inside this loop, there is a loop over all nodes of the FE interface. For every combination of nodes, the rbf is evaluated.[20]"*

Due to the deforming structure, the fluid grid has to be deformed. For this purpose the RBF method is used as well. Aitken under-relaxation is used to speed up convergence of the fixed point iteration [3] [21]. A greedy method is applied for the RBF interpolation to reduce the size of the computation. The greedy method starts with a small subset of mesh cells and searches for the largest error. The cells with the largest error are included in the next interpolation [37].

3

Benchmark Case

A benchmark case is performed by carrying out RANS-FEM simulations using ReFRESCO and ANSYS. Reason for the benchmark case is to get familiar with the methods and to check the reliability of the FSI module in ReFRESCO, therefore a simple test case is chosen with available reference literature. A sensitivity analysis is performed on settings and methods to analyse the influence and effect on results, which can be used for further analysis in the actual propeller study. This chapter starts with an explanation of the benchmark case with properties of the flow and structure. Hereafter, the numerical set-up of the fluid- and structural grid are outlined, together with the settings and types of simulations performed. The simulation and sensitivity analysis results are discussed and this chapter ends with a conclusion on this benchmark case.

3.1. Case Description

The benchmark case consists of a 2D flexible thin plate clamped perpendicular to a bottom plate. With a uniform air flow applied parallel to the bottom plate. The thin plate has a height of 1 m and thickness of 0.01 m. The domain is rectangular with the inflow 5 m in front of the plate and the outflow 10 m after the plate. The coordinate system and dimensions are shown in figure 3.1. Due to this air flow the plate will start oscillating in the direction of the in- and outflow of the domain. The density of the plate is 1200 kg/m^3 and has an elastic modulus of 3.5 GPa, which is comparable to the material of plastic disposable coffee cups. The medium is air with density of 1 kg/m^3 with a velocity of 10 m/s. The corresponding Reynolds number is 50. The properties of plate and medium are presented in table 3.1. The RANS-FEM simulations are performed using ReFRESCO and ANSYS. First fluid- and structural grids are constructed, after which simulations are performed.

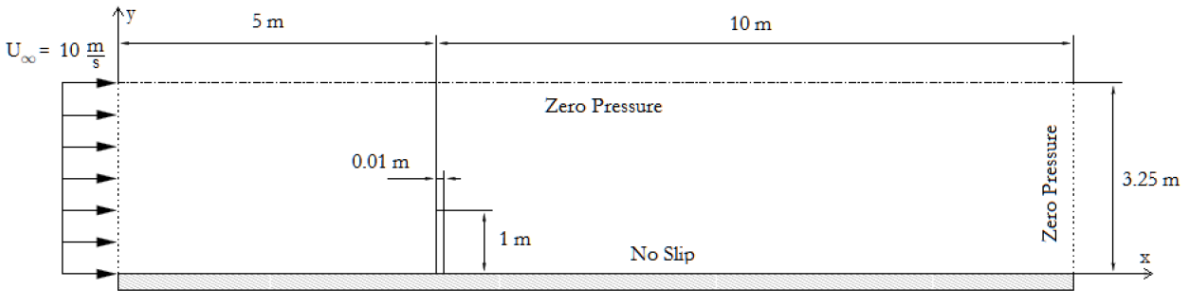

Figure 3.1: Dimensions of benchmark case with flexible thin plate [25]

The simulation results are compared to the PhD thesis of de Nayer [11] and MSc. thesis of Lesmana [25] who both performed this test case. De Nayer used a structured fluid grid of 30,000 cells, Lesmana an unstructured grid consisting of 16,938 cells both in the ISIS-CFD RANS solver. Both structural models consist of quadratic solid elements with 100 elements in height using structural solver Zorglib.

	Fluid	Solid	
Density ρ	1	1200	kg/m^3
Poisson's ratio ν	-	0.32	-
Young's modulus E	-	3.5	GPa
Dynamic viscosity μ	0.2	-	Pa s
Moment of inertia I	-	8.3e-8	m^4

Table 3.1: Properties of flexible plate and domain [25]

3.2. Structural Model

First, the structural model of the flexible thin plate is constructed. FE solver ANSYS is used because the output of this FE solver is supported by the FSI module of ReFRESCO. The FSI solver of ReFRESCO can only include solid elements, therefore solid elements are used for this model. Only the flexible plate of figure 3.1 is modelled in ANSYS. Clamped boundary conditions are applied at the bottom plate, and a free end on the top.

For the geometry of the plate it is most straightforward to make use of rectangular structural solid elements. The elements that can be chosen are linear solid elements (SOLID185) and quadratic solid elements (SOLID186). SOLID185 is a 3D solid element having eight nodes and three translational degrees of freedom at each node. SOLID186 is its higher order version, that contains 20 nodes and exhibits quadratic displacement behaviour. Both elements support plasticity, hyperelasticity, creep, stress stiffening, large deflection and large strain capabilities [40].

Important is to know the behaviour of the structure before an element type is chosen. To analyse whether the deformation is dominated by bending or shear the length to beam ratio (l/b) and slenderness ratio ($\frac{GAL^2}{EI}$) can be evaluated. The plate is long compared to its width which also follows from the ratios. For long beams bending is dominating in the deformation. For short beams this is mostly shear deformation. The length to beam ratio for this case is 100 and the slenderness ratio around 500. Therefore, the bending will be dominant in the plate compared to shear [41].

For structures where bending is dominant, shear locking can occur when using linear solid elements, as the curvature is not modelled accurately [16]. For a description of this phenomenon is referred to section 2.3.3. When using linear solid elements, more than one element through bending direction should be used to avoid shear locking.

First, the analytical formulas are given which are used for reference of the convergence study. Then, the structure grid is constructed by performing a convergence study on different elements sizes of the structural model and check the response with the analytical values.

3.2.1. Analytical Reference

As a reference for the convergence study of the ANSYS model, analytical values of natural frequency and deflection for a clamped beam are used. In both cases Euler-Bernoulli beam theory is used, which only takes into account pure bending and neglects the effect of shear. Assumptions made in this theory are that deflections are small, the neutral surface does not change during bending and the deformation due to shear is neglected[16]. In the last section it was demonstrated that bending will be dominant in the deformation of the plate. However, shear deformation could still have an effect. These assumptions should be kept in mind when comparison is made with the results of the ANSYS model.

The natural frequency of a clamped beam can be derived from the equations of motion. Using the Euler Bernoulli beam, the natural frequency equation is obtained by evaluating the boundary conditions of a beam clamped at one end and free on the other end [36]. For the derivation of these equations using modal analysis it is referred to section 2.3.1, of the theory chapter. The equation for natural frequency ω_n of modes $n = 1,2,3,..$ derived there, reads,

$$f_n = \frac{\alpha_n^2}{2\pi} \cdot \sqrt{\frac{EI}{\rho A l^4}} \quad \text{With:} \quad \alpha_n^2 = 1.875, 4.694, 7.885, .. \quad \text{for} \quad n = 1,2,3,.. \tag{3.1}$$

The natural frequency of the first mode is obtained by evaluating equation 3.1, with n=1. A frequency of 2.753 Hz was found, equal to de Nayer [11] and Lesmana [25].

For deflection of the plate the following analytical equation is used.

$$\delta_{max} = \frac{ql^4}{8EI} \tag{3.2}$$

The analytical displacement is calculated with a distributed loading of 50 N/m, elastic modulus of 3.5 GPa and moment of inertia of 8.3E-8 m^4 which leads to a maximum displacement of 0.0215 m, equal to reference values.

3.2.2. Grid Study

The element distribution of the grid is analysed by considering different distributions and comparing the results to the natural frequency and deflection determined in last section. The case is 2D, therefore, only the dimensions in x and y direction are defined in reference literature. However, as solid elements are used and the structural grid is eventually coupled to a 3D finite volume method, a dimension in z-direction (depth) is necessary as well. Dimensions of 0.01 and 0.02 are considered.

In table 3.2 the results for different element sizes are given when using linear solid elements (SOLID185). Left side of the table contains elements with a z-dimension of 0.01 m and the right side of 0.02 m. The element sizes, corresponding number of elements and the deviation from the analytical results are presented.

Chosen dim. For z [m]	0.01	0.01	0.01	0.01	0.01	0.02	0.02	0.02
Element size x [m]	0.0025	0.005	0.00125	0.0025	0.005	0.0025	0.005	0.005
Nr. elements in x	4	2	8	4	2	4	2	2
Element size y [m]	0.01	0.01	0.005	0.005	0.005	0.0025	0.005	0.005
Nr. elements in y	100	100	200	200	200	400	200	200
Element size z [m]	0.005	0.005	0.005	0.0025	0.005	0.01	0.01	0.005
Nr. elements in z	2	2	2	4	2	2	2	4
Aspect Ratio [-]	4	2	4	2	1	4	2	1
Total nr of elements	800	400	3200	3200	800	3200	800	1600
Nat. Freq. [Hz]	3.228	3.153	2.884	2.867	2.783	2.796	2.792	2.783
% from analytical sol.	17.2%	14.5%	4.8%	4.1%	1.1%	1.6%	1.4%	1.1%
Max. Displ in x [m]	0.0157	0.0164	0.0196	0.0198	0.0211	0.0209	0.0209	0.0211
% from analytical sol.	-27%	-24%	-9%	-8%	-2%	-3%	-3%	-2%

Table 3.2: Convergence study FE model with SOLID185 using different element sizes and dimensions for z

From the convergence study of table 3.2 it becomes clear that the natural frequency found in ANSYS is between 1.1 and 17 % higher than the analytically derived natural frequency. The deflection found in ANSYS is between 27 to 2 % lower. These deviations from the analytical values can be due to the Aspect Ratio (AR) of the elements. Numerically, the best solutions are found for an element aspect ratio of 1. This also becomes clear from the results of table 3.2. The best approximation is found for an aspect ratio of 1, when all element sizes are 0.005 m.

Deviation from the analytical results can be also due to assumptions made in the analytically derived values. The assumptions of pure bending, will lead to lower frequency and higher deflection when shear plays a role. However, as the ANSYS model seems to be "stiffer" it can be concluded that this is not the reason for the deviation from the analytical values, and bending is indeed dominant in the deformation of the plate.

Another reason for deviation can be the shear locking effect as linear elements are used. Due to the use of linear solid elements it is expected that the shear locking effect will lead to higher stiffness to bending and lower deflection. This is probably the cause for the higher frequency and lower displacement found with this

ANSYS model. It is expected that with higher order elements (SOLID186) this effect will be smaller. The response, when using quadratic solid elements (SOLID186) and the same element distribution, is closer to analytical results compared to the linear solid elements. Leading to a natural frequency of 2.76 and displacement of 0.0214 m, this is 0.3 % and 0.4 % from the analytical solution respectively. However, for a first reference SOLID185 is chosen for further analysis and assumed to be sufficiently accurate. The chosen ANSYS model with an element size of 0.005 in all directions, is given in figure 3.2 and table 3.3.

Element size x	0.005	m
Nr elements in x	2	
Element size y	0.005	m
Nr elements in y	200	
Element size z	0.005	m
Nr elements in z	2	
Natural Frequency	2.783	Hz
% From analytical solution	1.1	%
Max. Displacement in x	0.0211	m
% From analytical solution	-2	%

Table 3.3: Element sizes structure grid in ANSYS

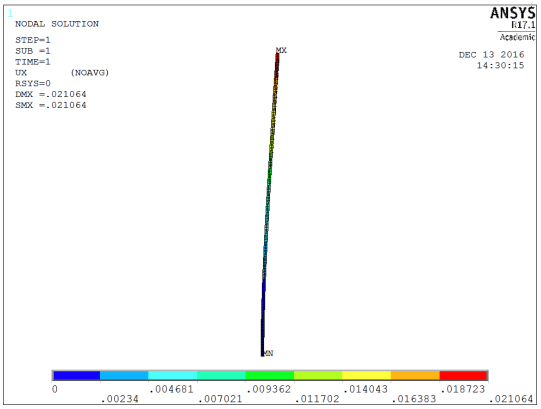

Figure 3.2: ANSYS model SOLID185 - Benchmark case

3.3. Fluid Model

The fluid grid is created using the program HEXPRESS, yielding unstructured full hexahedral meshes [19]. Dimensions of the computational domain are chosen equivalent to figure 3.1 with a total length of 15 m and height of 3.25 m. The dimension in z-direction is 0.01 m, corresponding to the structure grid, The Reynolds number of this problem is 50, based on the length of the plate and a uniform flow of air of 10 m/s, it is expected that the fluid flow is smooth without turbulent effects as in results of de Nayer and Lesmana [11] [25]. The applied boundary conditions are listed in table 3.4.

	Boundary condition
Inlet	Velocity at boundary = 10 m/s
Outlet	Pressure at outlet = 0.0 m/s
Plate	Velocity is zero at the wall, No wall functions applied (y+ should be <1).
Bottom domain	Velocity is zero at the wall, No wall functions applied (y+ should be <1).
Top domain	Pressure at top = 0.0 m/s
Left domain	Velocity normal to the wall is zero, tangential velocity at wall is free.
Righ domain	Velocity normal to the wall is zero, tangential velocity at wall is free.

Table 3.4: Boundary conditions on different walls of the fluid domain

First, a fluid grid is composed consisting of a total of 26,506 cells with a refinement near the plate and bottom. Then, a simulation is performed to check the accuracy of the grid. This is done by evaluating the y+ values and jump estimators which will be explained next. Depending on this evaluation the grid is refined or coarsened and different grid densities are obtained. Of the final grid the numerical uncertainty is determined before the final simulations are performed.

3.3.1. Discretisation

The accuracy of the grid is checked by evaluating the y+ values and jump estimators after a simulation. The y+ is the non-dimensional wall distance, used to indicate the grid spacing adjacent to the wall. The aimed value for y+ is depending on Reynolds number. To resolve the fluid equations down to the wall, i.e. without the use of wall function, an y+ below one is desired for low Reynolds numbers[39]. The y+ values are monitored at the plate bottom.

Evaluation of y+ values on the initial grid show that y+ at the bottom plate is much smaller than 1 and thus does not need refinement near the bottom of the plate. This is due to the low Reynolds number of 50.

The mesh at the bottom cells can be coarsened, which is applied in the revised second grid.

The jump estimators measure variation in results between two consecutive cell centres, which is a measure of the discretisation error. If the step between two cell centres is too large the mesh should be refined at that location. The error estimators used in this method are described in section 2.2.3 of the theory chapter. In the paper of Windt [46] the discretisation error was investigated in a boundary layer, small errors (<5 %) were found for jump estimators between 10^{-4} and 10^{-5}. Therefore, the jump estimators of this grid are kept in this range.
Evaluation of the jump estimators of the initial grid results show that refinement is needed in front of and after the plate as visible in figure 3.4. The grid is refined by placing a box around the plate, which is refined more than the surrounding cells (grid 2). This box refinement is based on the grid of Lesmana [25], with dimensions of 4.5 x 2 m around the plate. After evaluation the cells among the box are refined as well, leading to grid 3 in figure 3.8 and 3.9. This grid is used in further simulations.

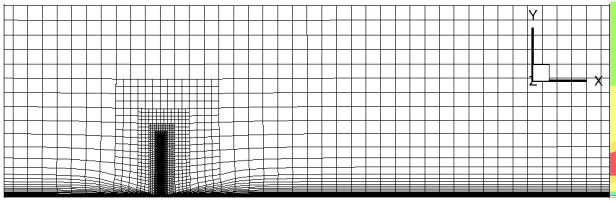

Figure 3.3: Initial fluid grid 1 (26,506 cells)

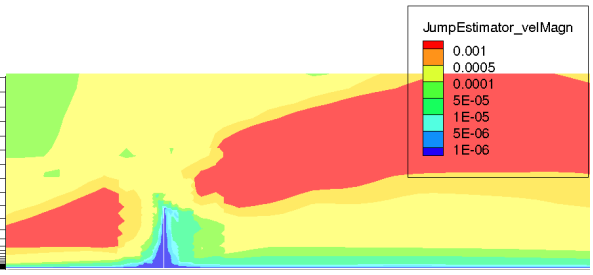

Figure 3.4: Jump estimators of initial fluid grid 1

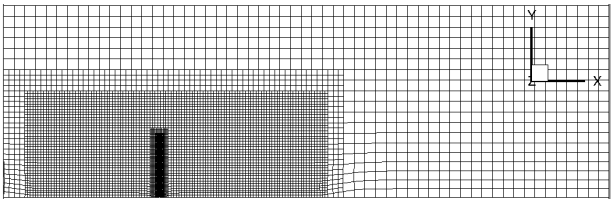

Figure 3.5: Grid 2, with box around plate (14,576 cells)

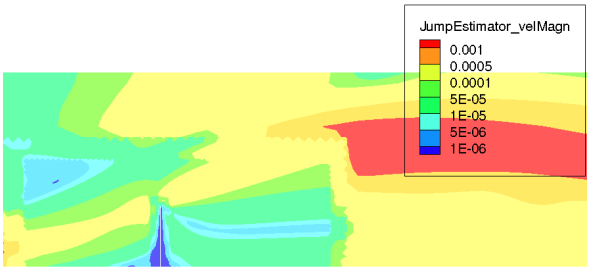

Figure 3.6: Jump estimators of grid 2

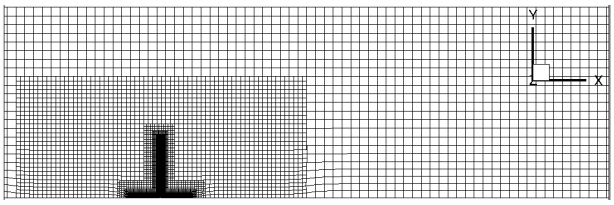

Figure 3.7: Grid 3, with box and finer grid (19,389 cells)

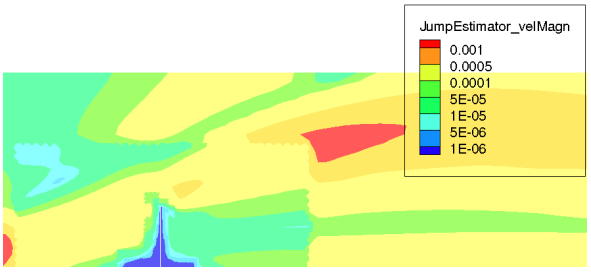

Figure 3.8: Jump estimators grid 3

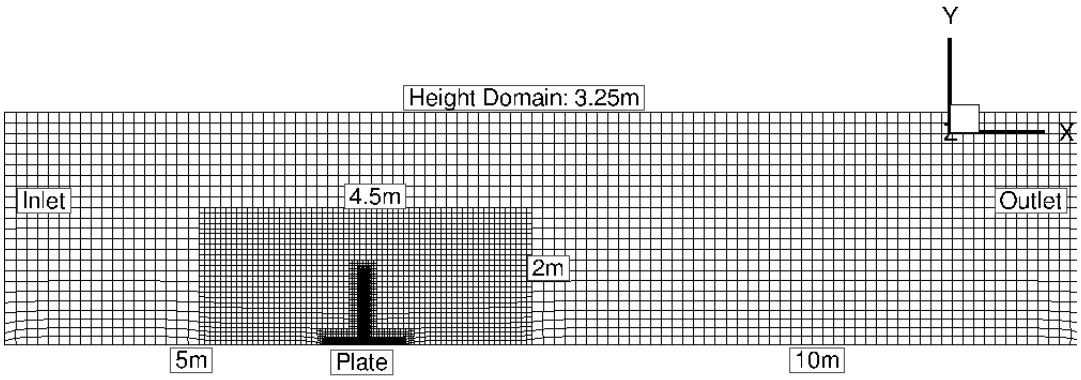

Figure 3.9: Domain of final fluid grid (19,389 cells)

3.4. Simulations

With the fluid- and structural grid obtained in the last sections simulations can now be performed. Two types can be distinguished, one where the plate is rigid, flexibility is not taken into account and only a RANS simulation is performed with the fluid grid. Other simulations are with the flexible plate by performing FSI (RANS-FEM) simulations. An overview of these simulations is given in figure 3.10. First the settings of the rigid and FSI simulations are outlined, for the understanding of these sections it is recommended to read the theoretical background on ReFRESCO and FSI in ReFRESCO of chapter 2.2.2 and 2.4. In section 3.5, the results are presented. For the rigid plate the pressure, streamlines and numerical uncertainty are determined, whereas for the flexible plate the pressure, deflection, frequency and numerical uncertainty are determined.

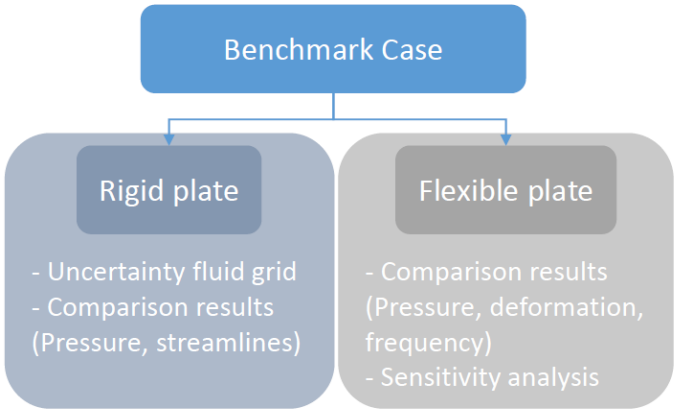

Figure 3.10: Simulations Benchmark case

3.4.1. Settings Rigid Plate

Simulations are performed by applying uniform flow of 10 m/s to the rigid plate. Steady calculations can be carried out as the Reynolds number of 50 is low and turbulent fluctuations in the flow will not be present. The flow will reach an equilibrium at around t = 10 s [25]. When only this equilibrium state of the fluid is to be captured, steady simulations can be performed. The fluid grid of figure 3.9 is used with the boundary conditions of table 3.4.

Within an iteration step of the outer loop, the complete non-linear system of equations is solved. The convergence tolerance of the outer loop is set to 1E-6. A QUICK scheme is used for the momentum solver. Velocity-Pressure coupling is achieved by solving the coupled mass-momentum system directly [4].

3.4.2. Settings Flexible Plate

RANS-FEM simulations are performed by coupling the ANSYS FEM model constructed in section 3.2 to the fluid. Before simulations are carried out, it is checked whether the location of the structural nodes is correct in the fluid grid. As explained in the theory chapter about FSI module in ReFRESCO, section 2.4.3, the FEM model is coupled by three output files of ANSYS, the geometry, mass- and stiffness matrix and a file containing information of the interface nodes of the structure grid. This file can be loaded into the fluid grid geometry to check whether the nodes properly connect.

Due to the flexibility of the plate, it is expected that the plate will start deflecting in response to the airflow of 10 m/s which is applied at once, without a ramp function. The FSI simulation requires an unsteady simulation to be performed, even though it is expected that the plate will reach an equilibrium and after some time a steady outcome is obtained. This is due to the grid deform method solving the deformation of the fluid grid due to the fluid structure interaction. This method updates the fluid grid corresponding to the deformation of the structure.

The convergence tolerance of 1E-6 of the outerloop is equal to the rigid simulations. A segregated mass momentum solver type is used, which means that the mass equation is solved for all cells, after which the subsequent equation is solved for all cells [4]. A coupled solver was not possible with FSI module during the time of the simulations. A quick scheme is used as in the rigid simulations.

Additional settings required for the FSI simulations are due to additional time discretisation of the unsteady simulation and due to the FSI module of ReFRESCO. A timestep of $\triangle t$ = 0.01 s is used, equal to $\triangle t$ of de Nayer [11] and Lesmana [25]. Time discretisation is solved by using a implicit three time level scheme. The grid deform method uses RBF interpolation with a radius of 0.8 m, a greedy method and a convergence tolerance of 1E-4. The load transfer across the interface of fluid and structure is governed by RBF interpolation with radius of 0.4 m and a convergence tolerance of 1E-12.

During the simulation the force on the plate is monitored, which is obtained from the pressure integrated over the plate area. The deformation of the plate is monitored by the x-coordinate at the top of the plate. The force and deformation are both stored in a text file at every time step.

3.5. Results Rigid plate

In this section results of the steady simulations with the rigid plate are presented. As explained in the previous section, first RANS simulations are performed with the rigid plate using the fluid grid obtained in section 3.3. Steady simulations are performed with uniform inflow of 10 m/s applied at once. First, the discretisation error is determined, then the results of the steady rigid plate simulations are compared to de Nayer [11] and Lesmana [25].

3.5.1. Numerical Uncertainty

The discretisation error is determined using the numerical uncertainty method of Eça and Hoekstra [14]. In this method the error is estimated by performing simulations with identical grids having different cell density. For a description of this method it is referred to the theoretical background, chapter 2.2.3.

Four grids with different density are used. Fluid grid 3, from now on grid A, of figure 3.9 is refined three times leading to four grids with different grid density, grids A, B, C and D of table 3.5. For the refinement, the adaptive grid refinement method in ReFRESCO is used. Within this method each cell of the grid is refined either 2, 4 or 8 times in x- and y direction. Where the initial grid has 1 cell, the refined grids have either 4, 16 or 64 cells. The number of cells for the refined grids are given in table 3.5.

The results of the uncertainty analysis are shown in figure 3.11. The relative step size of 8 at the x-axis, represents the unrefined grid, step size 1 is the finest grid refined eight times. On the y-axis the converged value for the force is given. The estimated uncertainty based on the fit through the results is 0.03 %. It can be concluded that the result is very accurate (second order). Due to the grid being accurate and the increased computational time of the finer grids, the initial grid of figure 3.9 is used in further simulations.

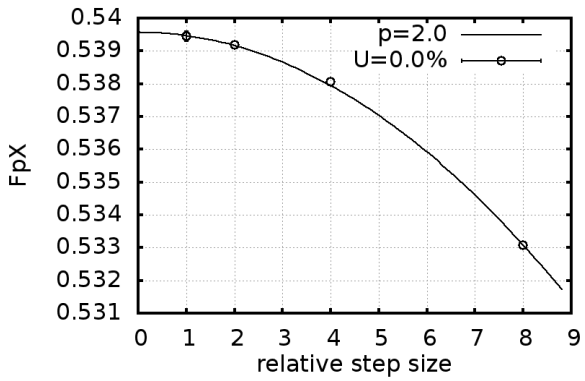

Figure 3.11: Uncertainty analysis

Grid name	Amount of cells	Iterations
grid A	19,389	413
grid B	77,556	691
grid C	310,224	1032
grid D	1,240,896	8824

Table 3.5: Different grid densities used for uncertainty analysis, with corresponding number of iterations until a converged solution is obtained

3.5.2. Pressure and Streamlines Results

The results of the RANS simulations with the rigid plate are expressed in pressure and streamlines of the fluid at the converged solution. This equilibrium pressure is shown in figure 3.12 and streamlines in figure 3.14. The result found by Lesmana [25] for the rigid plate is given as reference in figures 3.13 and 3.15.

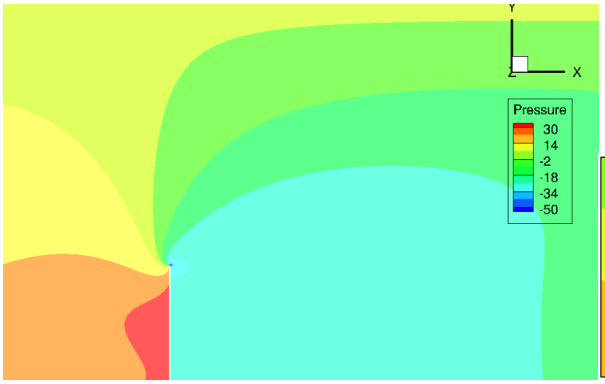

Figure 3.12: Pressure steady simulation (ReFRESCO)

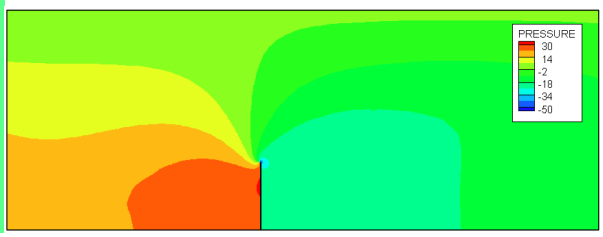

Figure 3.13: Pressure distribution at t=10 s (Lesmana [25])

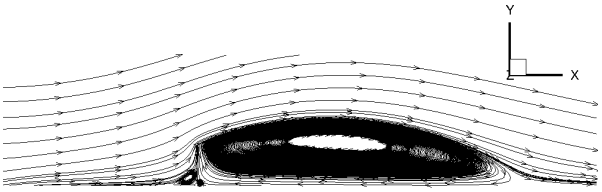

Figure 3.14: Streamlines steady simulation (ReFRESCO)

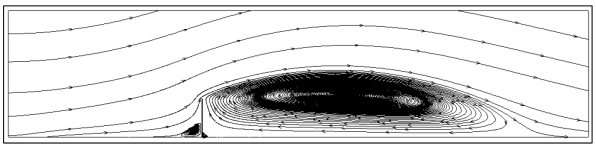

Figure 3.15: Streamlines velocity at t=10 s (Lesmana [25])

The pressure distribution shows maximum positive values at the top and front area of the plate. At the back of the plate the pressure is negative. Forces on the plate are monitored by integrating the pressure over the area. A total force of 54 N in x-direction is found representing the pressure integrated over the entire plate.

3.6. Discussion Rigid Results

The pressure results and streamlines found for the rigid plate (figures 3.12, 3.14) are compared to results found by de Nayer [11] and Lesmana [25]. Comparable results were found as becomes clear from figures 3.13 and 3.15. The streamlines show the same behaviour. In figure 3.13 a larger area of highest pressure is visible and a higher low pressure region on the right side of the plate. When comparing this pressure distribution to the results of the RANS simulation of figure 3.12, it becomes clear that a smaller region of highest pressure is found and a lower pressure on the right side of the plate. These differences can be due to the different fluid solvers or discretisation of the problem. However, it can be concluded that the overall pressure difference between left and right side of the plate is the same.

3.7. Results Flexible Plate

In this section the RANS-FEM results of the flexible plate simulations are explained. Within these simulations the structural ANSYS FEM model of figure 3.2 is coupled to the fluid grid. Unsteady simulations are performed with a uniform air flow of 10 m/s with settings as explained in section 3.4.

First the numerical uncertainty is determined of these steady equilibrium results. Then the deflection and frequency results are outlined and discussed.

3.7.1. Numerical Uncertainty

The discretisation error of the FSI simulations is determined in the same way as for the rigid simulations of section 3.5.1. The first three refined grids of table 3.5, are used for the numerical uncertainty method. The result is shown in figure 3.16, it is visible that the discretisation error is still very low, 0.07% (rounded to 0.1% in the figure). Therefore, the FSI simulations are carried out with the coarsest grid having 19.389 cells of figure 3.9.

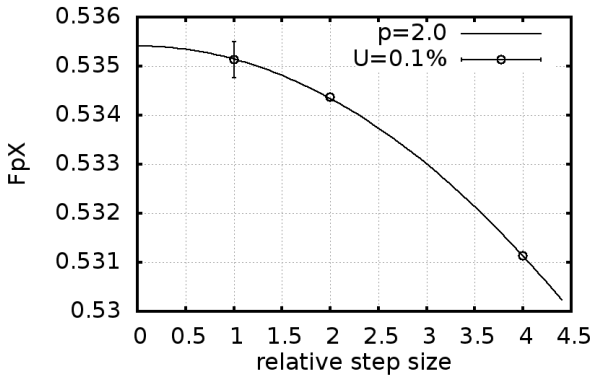

Figure 3.16: Numerical uncertainty FSI simulation

3.7.2. Deflection

The pressure distribution in the response of the flexible plate is shown in Figure 3.17. It is clearly visible that at the start of the simulation a large pressure is visible at the frontal area of the plate and a low pressure at the upper back of the plate. This low pressure is due to the separated flow behind the plate. In the second figure it is visible that the flow separates after 0.13 s.

The tip displacement in x-direction is monitored in figure 3.18 with pointers indicating at which time steps figure 3.17 is obtained. The motion is damped due to viscous damping of the plate in the air flow. The equilibrium displacement after approximately 4 seconds is 0.024 m. The pressure reaches an equilibrium state as well as shown in the last figure of 3.17.

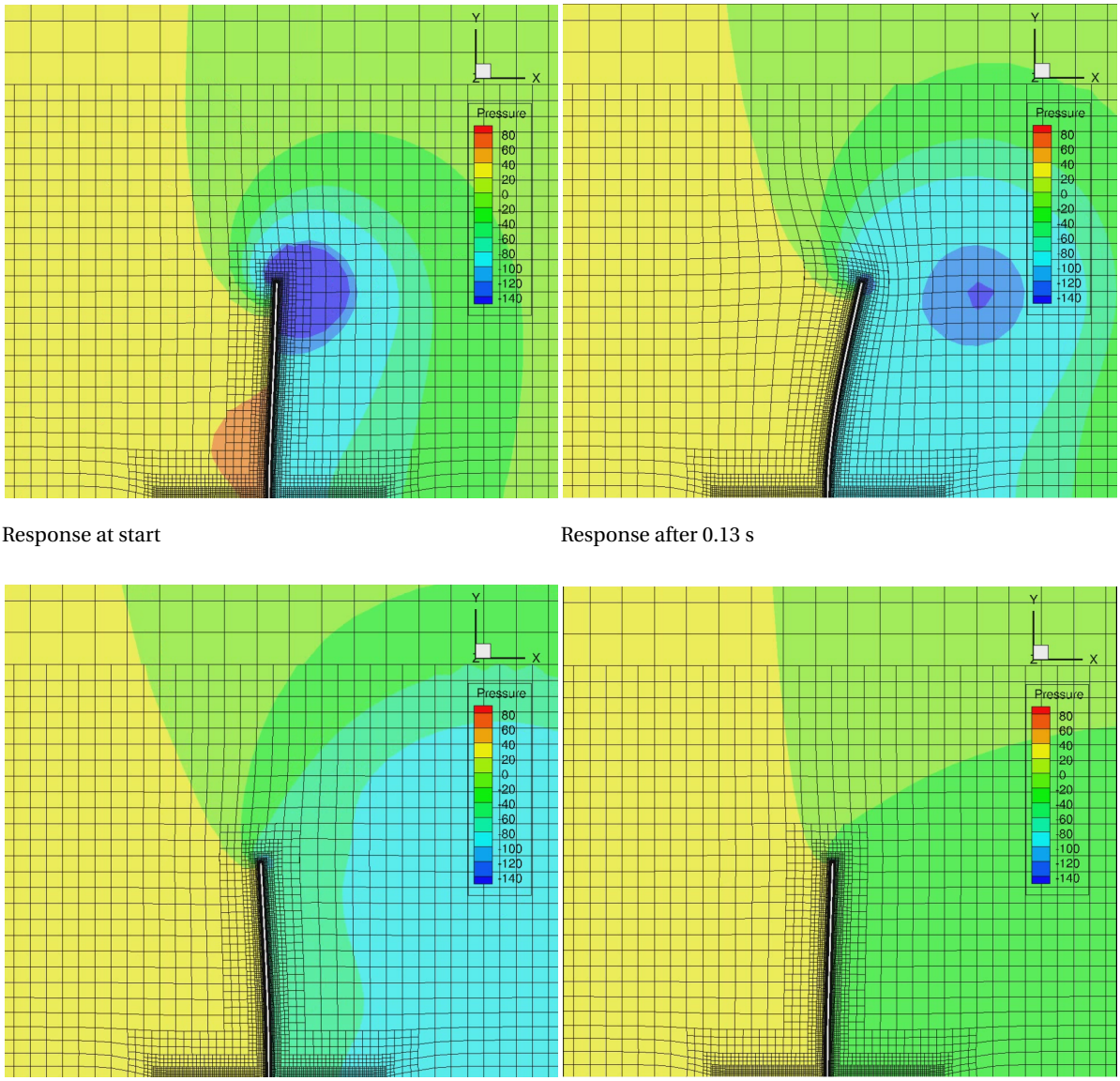

Response at start

Response after 0.13 s

Response after 0.3 s

Response after 4 s

Figure 3.17: FSI response at different timesteps

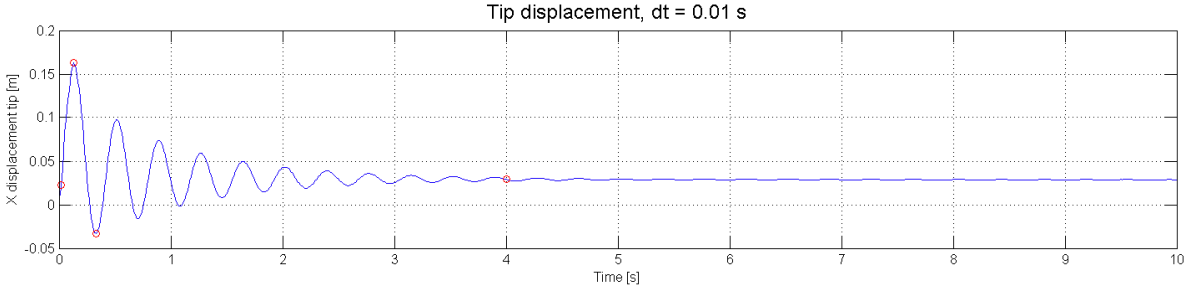

Figure 3.18: Tip displacement, red pointers indicate the timesteps where plots of 3.17 are defined

3.7.3. Response Frequency

From figure 3.18 it becomes clear that the plate vibrates in the first 5 seconds of the response. It is expected that the frequency of this vibration is close to the natural frequency of the plate. When a Hanning window and Fast Fourier Transform (FFT) is applied to the first 5 s of the response from figure 3.18 with $\triangle$t = 0.01 s, a frequency of 2.734 Hz is found. The first 5 seconds are only used because after 5 seconds the displacement is damped and has an equilibrium value of 0.024 m.

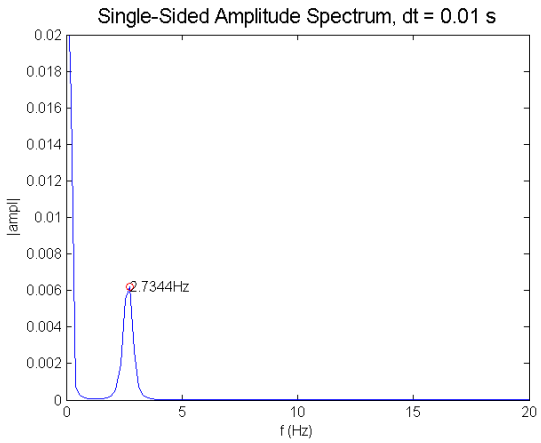

Figure 3.19: FFT applied on response of calculation with $\triangle$t=0.01 s

3.8. Discussion Flexible Results

The equilibrium displacement of 0.024 m found after t=5 s is equal to displacements found by both de Nayer [11] and Lesmana [25]. The frequency of 2.734 Hz is comparable to Lesmana[25] and de Nayer[11] who found 2.73 and 2.71 Hz, respectively. The natural frequency found in the modal analysis of the ANSYS model was 2.78 Hz. The reason for the frequency being lower in the simulation response is probably the viscous damping of the plate in the flow. This is not a free undamped vibration as in the modal analysis, leading to a lower frequency in the simulations. Expected is that when a smaller time step $\triangle$ t is chosen higher frequencies are found in the response as well.

RBF interpolation is used for the transformation of load and deformation across the interface of fluid and structure. It is checked whether the deflection in ANSYS is the same compared to the deflection response of ReFRESCO. By importing the pressure distribution from ReFRESCO in the ANSYS model, the same displacement of 0.024 m was found. The performance of the interpolation is also determined the other way around. A steady simulation is performed with the deformed solution after t = 5 s as grid. When the interpolation of pressure across the interface works properly, the forces on the plate should be the same. A difference of 0.009 % was found in the forces. It can be concluded that the results are the same as found in reference literature and that the loads and deformation are correctly transferred throughout the interface. The RBF interpolation and time step are discussed further in the sensitivity analysis.

3.9. Sensitivity Analysis

To get more insight in the behaviour of different methods and parameters in the FSI module of ReFRESCO a sensitivity analysis is performed. The influence of added Rayleigh damping, different time steps and RBF radii are analysed and discussed. Damping can be useful for the propeller study later on. Damping can be added to obtain an equilibrium steady equation earlier. The influence of the time step is analysed to see the effect of the magnitude of the time step on the captured response. The RBF radius is checked as the RBF provides a crucial part of the transfer of loads and deformations across the fluid- structure interface. More insight in the performance of RBF is useful for further analysis.

3.9.1. Rayleigh Damping

The influence of Rayleigh damping on the result of flexible plate simulations is analysed. By adding damping, energy is dissipated reducing the amplitude of the vibration [16]. More information on damping is given in the theory chapter 2.3. Damping can be added to the system to limit the peak response or when the final equilibrium solution is requested, rather than the initial response of the structure. For the flexible propeller this can be useful as tests are performed in a uniform wakefield and only the final equilibrium result is used for analysis as explained in the scope of section 1.4.

From the flexible plate response it becomes clear that there is already damping in the system. This is probably viscous damping due to the structure interacting with air. From the response, this damping can be determined by the maximum at $t = T$ compared to n consecutive maxima at $t = T + nT$, by using the logarithmic decrement (δ) [36] defined by,

$$\delta = \frac{1}{n} \ln \frac{x(t)}{x(t+nT)} \tag{3.3}$$

From this logarithmic decrement the damping ratio (ζ) is determined with [36],

$$\zeta = \frac{\delta}{\sqrt{(2\pi)^2 + \delta^2}} \tag{3.4}$$

By comparing the first peak and last peak of the response in figure 3.20 a logarithmic decrement of $\delta = 0.13$ and corresponding damping ratio of $\zeta = 0.021$ is found.

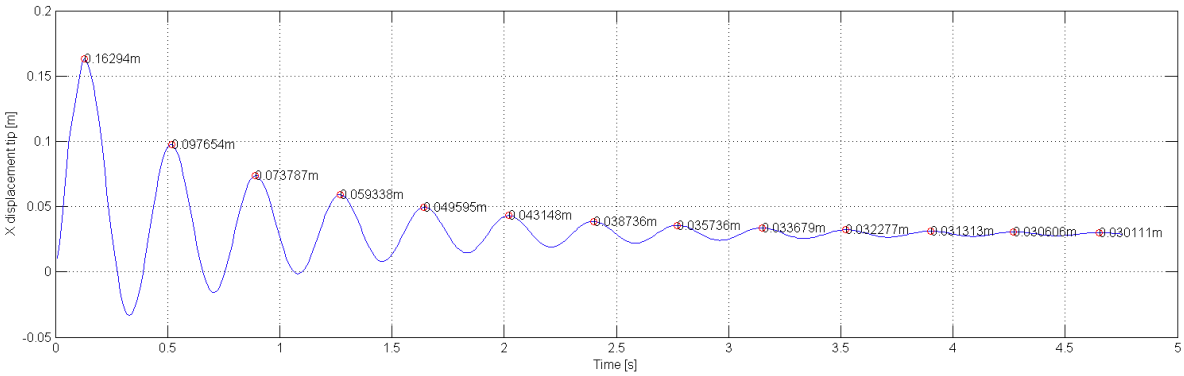

Figure 3.20: Amplitudes of the simulation without Rayleigh damping used for determination of logarithmic decrement

In the FSI module of ReFRESCO an option for added Rayleigh damping, is built in. This means that an α and β can be defined for mass- and stiffness proportional damping, respectively. Damping matrix $[C]$ is then defined by,

$$[C] = \alpha[M] + \beta[K] \tag{3.5}$$

Coefficients α and β are obtained by choosing a critical damping coefficient. Critical damping is the lowest damping for which the oscillatory movement is totally damped. The fraction of this critical damping is called the damping coefficient. Then α and β can be determined using the frequency range (ω_1, ω_m) and selected damping ratios (ζ_1, ζ_m). The damping ratios correspond to the chosen amount of critical damping. α and β are obtained by evaluating equations 3.7 and 3.6 [6].

$$\beta = \frac{2\zeta_1\omega_1 - 2\zeta_m\omega_m}{\omega_1^2 - \omega_m^2} \tag{3.6}$$

$$2\zeta_1\omega_1 = \alpha + \beta\omega_1^2 \tag{3.7}$$

Two critical damping ratios are chosen, 0.1 and 0.05, in the range of $\omega/2\pi = 2-3$ Hz. Corresponding α and β are: $\alpha = 1.255$ and $\alpha = 2.507$ and corresponding $\beta = 0.0032$ and 0.0064.

The response of these two simulations together with the response of the system without proportional damping are given in figure 3.21 and corresponding maximum values at $t = T$ and $t = nT$ in table 3.6.

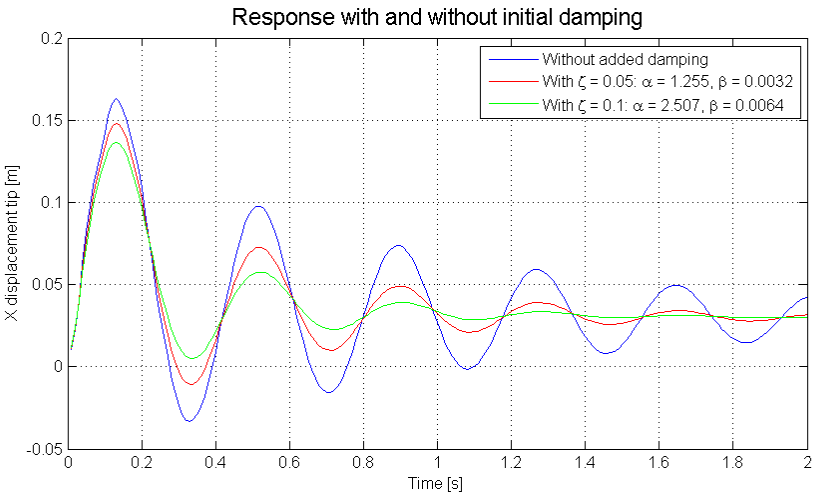

Figure 3.21: Response of system with and without proportional damping

Alpha	0	1.255	2.507
Beta	0	0.0032	0.0064
Ampl 1st peak	0.163	0.148	0.137
Ampl 2nd peak	0.098	0.073	0.058
Ampl 3rd peak	0.074	0.049	0.039
Ampl 4th peak	0.059	0.039	0.034
Ampl 5th peak	0.050	0.034	0.031
ζ (1st vs 5th peak)	0.0378	0.0468	0.0472

Table 3.6: Amplitudes found for response of figure 3.21

3.9.2. Discussion Rayleigh Damping

The system already shows damping without any added proportional damping. This is probably due to viscous damping exerted by the interaction of air and structure due to its velocity in the medium. From figure 3.21 and table 3.6 it becomes clear that when proportional damping is added for $\zeta = 0.05$, the maximum values compared to the initial response are lowered with 0.015 to 0.025 m every period T. This leads to a damped response after approximately 6 periods. For $\zeta = 0.1$ this is between 0.025 and 0.04 m every period T, and a damped response after 4 periods.

The corresponding damping ratios determined from the logarithmic decrements of the response are shown in table 3.6. Differences between the damping ratios are due to the different methods of determining the coefficients. One is experimentally by comparing maximum values, the other is by choosing a damping coefficient in a certain range of frequencies. Another reason for the differences can be the effect of numerical damping of the solving method. When the exact amount of damping is needed, this influence should be further analysed.

3.9.3. Time Step

The time of a simulation is subdivided into a discrete number of time steps. This is called time discretisation. To fully capture the response the time step should be chosen carefully. If the time step is chosen too large, the solver will not be able to capture the response. Parts of the response are "jumped over" by the time step. Furthermore, solvers can become inaccurate or unstable if the time step is chosen too small. Therefore, the effect of the time step should be checked. The natural frequency of the system found in section 3.7 is 2.73 Hz which corresponds to a natural period of 0.366 s. To ensure at least 10 data points in one period, the time step should be smaller than 0.04 s. Simulations with $\triangle t = 0.001$ to 0.1 s are performed to analyse the behaviour. The displacement responses for the time steps $\triangle t = 0.005$ to 0.1 are shown in figures 3.22 and 3.23.

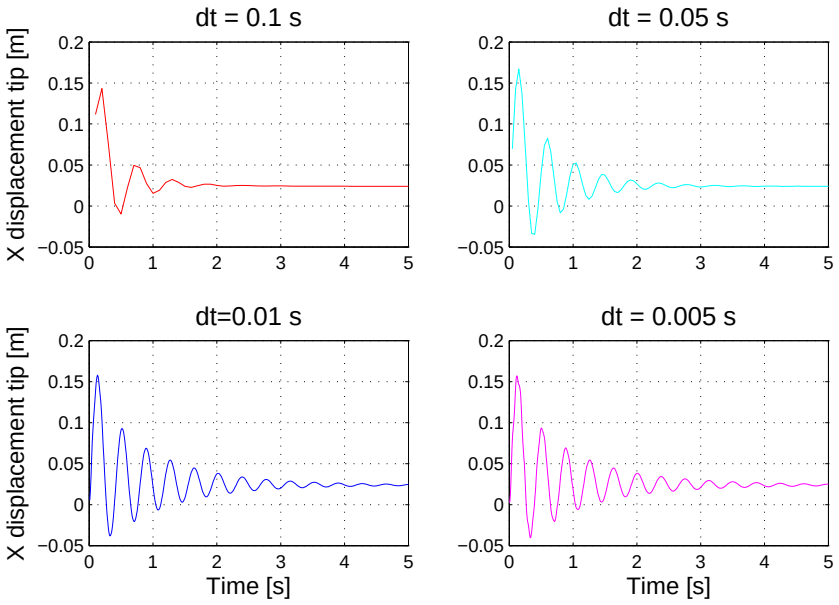

Figure 3.22: Tip displacements for different timesteps

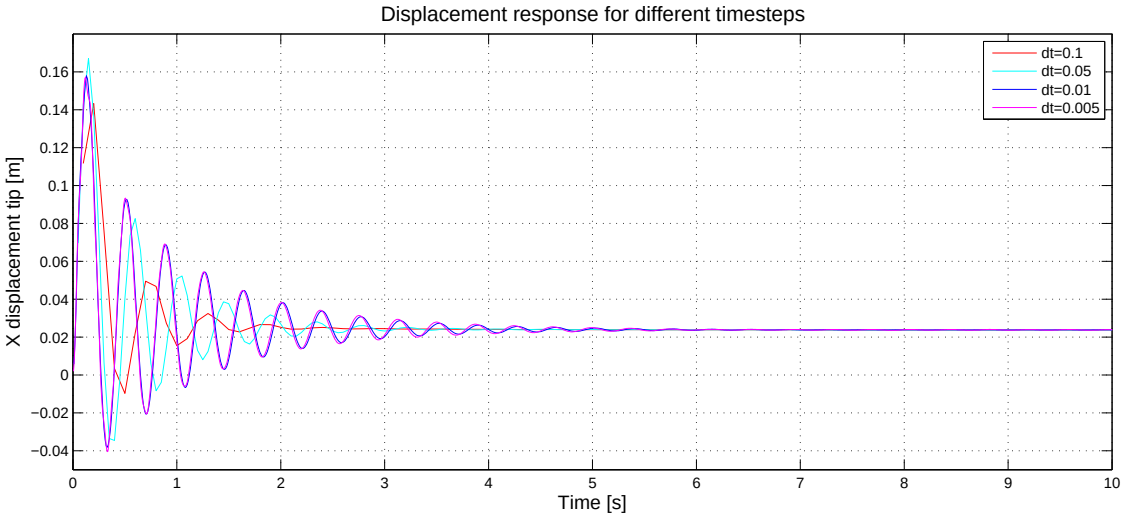

Figure 3.23: Tip displacements for different time steps in one figure

The force response is shown in figure 3.24, for time step $\triangle$t = 0.005 s and smaller. The response showed higher frequency signals on top of the signal obtained with time step $\triangle$t = 0.01 s. When the time step further decreases, peaks occur in the response between t = 2 s and 2.5 s for $\triangle$t = 0.001 s. For $\triangle$t = 0.003 s these peaks did occur as well, however, later in the signal and with lower amplitude.

3.9.4. Discussion Time Step

The response of $\triangle$t = 0.01 s and $\triangle$t = 0.005 s are close to each other. When the time step is larger than 0.01 the response is not fully captured and as a consequence damped earlier. In figure 3.23, all responses are plotted together. It becomes clear that the equilibrium response after t=5 s is the same for all time steps $\triangle$t.

Mean equilibrium displacements for $\triangle$t = 0.005 - 0.1 are the same. For the forces this holds for $\triangle$t = 0.003 - 0.1. The peaks in the force response of smaller time step $\triangle t$ = 0.003 s are probably due to an error occurring in ReFRESCO. The pressure shows fluctuations between two consecutive cells, which wrongly determines the

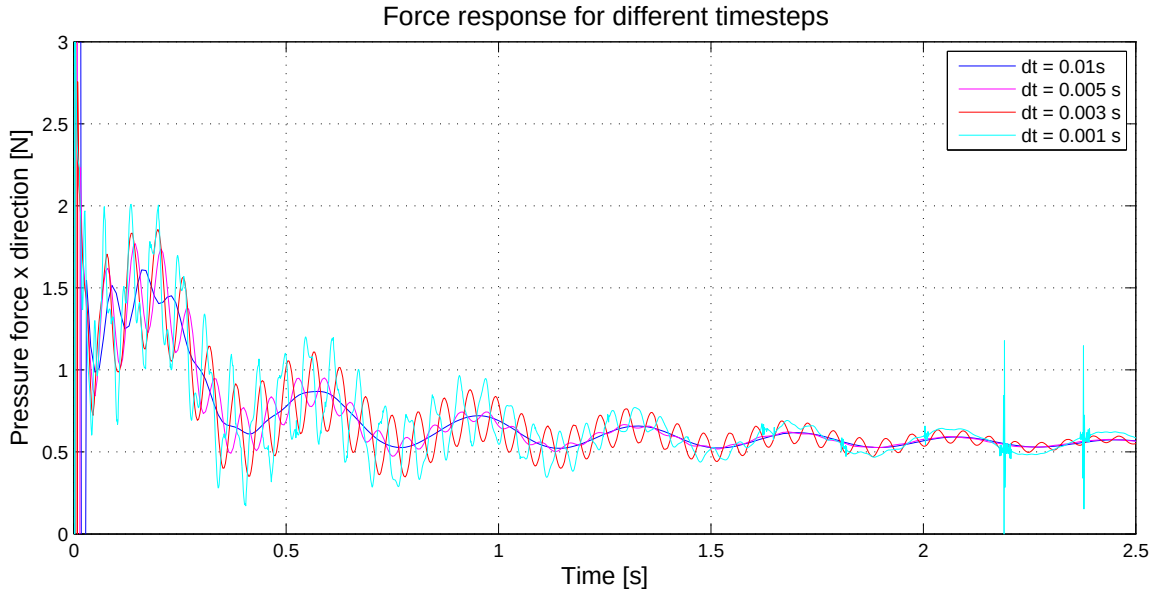

Figure 3.24: Forces for different time steps

force on the plate. After the peak the simulation continues and seems to converge when the pressure fluctuations are not present. This phenomenon is probably not due to FSI simulations as it can occur in ReFRESCO simulations without FSI as well.

From this analysis on the magnitude of the time step Δt, it is concluded that in order to capture the full displacement response, the time step should be chosen sufficiently small. The method of ensuring at least 10 data points in one period of the vibration response seems a suitable rule of thumb.

The time step should not be chosen too small, as peaks in the pressure can occur leading to several peaks in the force response. When only the final equilibrium state is requested in a steady simulation a larger time step suffices, as the larger time steps showed the same final equilibrium displacement and mean force.

3.9.5. RBF Interpolation

Two different grids are used for the fluid and structure. Therefore, interpolation between the grids is necessary to transfer load of the fluid to the structure across the interface. Also, deformation has to be transferred from the structure through the interface to the fluid grid. The RBF interpolation is used for the transfer of loads and deformation across the interface between fluid and structure. For a description of the RBF interpolation it is referred to theory chapter 2.4.4. As this is an integral part of the fluid-structure interaction simulation, performance of RBF is analysed.

In the theory chapter it was explained that a higher RBF radius generally leads to a more accurate solution [9]. When a cell moves, only the nodes inside a circle with this RBF radius are influenced by the movement of this cells' centre. However, the size of the problem that is solved increases with increasing RBF radius. The influence of the magnitude of this RBF radius is analysed by performing simulations with different RBF radii of 0.2, 0.4, 0.6 and 0.8 m.

For a radius of 0.2 the grid deformation crashes at the plate top. If the response of the simulation with RBF radius 0.8 and 0.4 are compared a difference in plate top displacement for the first peak in the response of 0.00025 m (figure 3.25) is found. It can be seen that when the total displacement of the plate declines the different response for two RBF radii also decreases and becomes close to zero after t=3 s.

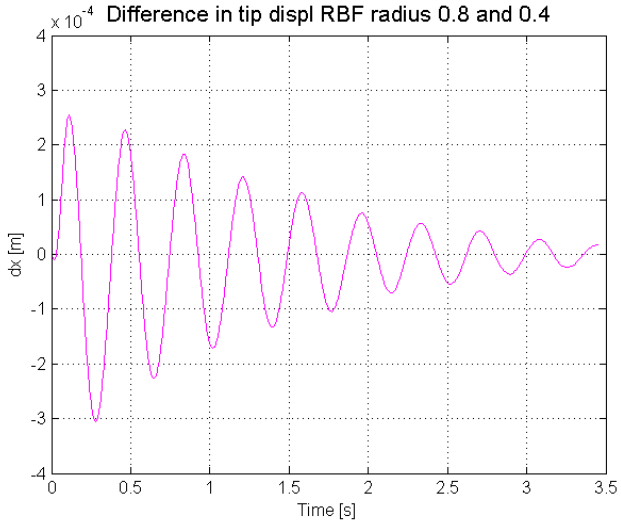

Figure 3.25: Difference in tip displacement between response with RBF radius 0.8 and 0.4

3.9.6. Discussion RBF Interpolation

From this analysis it follows that the RBF radius should be larger than 0.2 m. Reason for the instability at low RBF radius is the geometry of the model. The plate top consists of an abrupt angle of 90 degrees. This asks for a large RBF radius for stability.

The difference between response of RBF radius of 0.4 and 0.8 shows a difference in displacement of 0.00025 m for the first peak. This is approximately 0.2% from the total displacement of the first peak, found with a RBF radius of 0.8. The difference in displacement decreases together with the response of the plate. It can be concluded that for simulations where only the final equilibrium displacement is needed, the error between RBF radii is lower. However, for a stable and accurate solution the RBF radius should be chosen sufficiently large. In the FSI module of ReFRESCO, the total work, total energy loss and change in energy per time step are monitored, these are shown in figure 3.26. From this figure it becomes clear that after some time the energy loss and change become zero, when the equilibrium is reached.

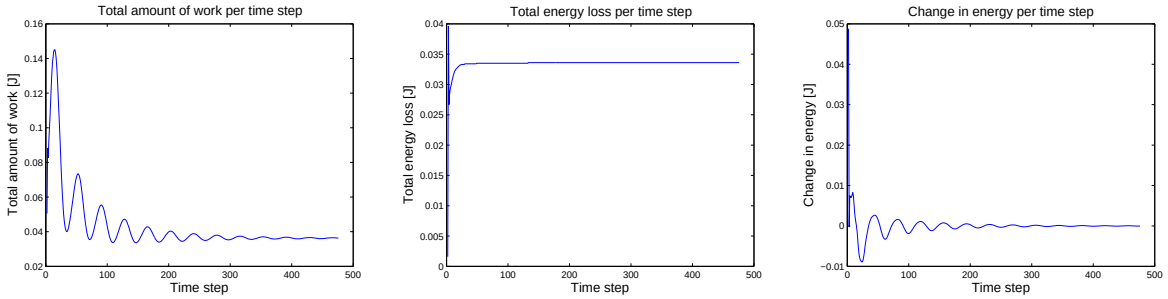

Figure 3.26: The total amount of work, energy loss and change of energy at the interface

3.10. Summary and Conclusions

In this chapter a benchmark case is carried out on a 2D flexible thin plate clamped perpendicular to the bottom. With a uniform air flow applied that is parallel to the bottom plate. Simulations are carried out as if the plate is rigid and flexible, either by performing RANS and RANS-FEM simulations using ReFRESCO and ANSYS. The reason for this benchmark case is to get familiar with the methods and to check the reliability of the FSI module in ReFRESCO. The results are compared to literature and a sensitivity analysis is carried out.

The fluid grid is created using the program Hexpress and consists of an unstructured hexahedral mesh. The final mesh was obtained by improving the initial grid by monitoring the y+ and jump estimators. The numerical uncertainties of the final mesh are 0.03 % and 0.07 % for rigid and FSI results, respectively.

The structural model is build up of linear solid elements (SOLID185). A grid study is carried out, comparing the deflection and natural frequency with analytical values. Before the simulations are carried out, it is checked whether the fluid and structure interface are correctly outlined. The conclusions drawn in this chapter are outlined here.

1. The FE model has a deviation of -2% and 1.1% for deflection and natural frequency, respectively. Quadratic solid elements (SOLID186) give a result closer to the analytical solutions of 0.4% and 0.3% for deflection and natural frequency, respectively. This difference between linear- and quadratic solid elements is assigned to the shear locking effect. The linear solid model is assumed to be sufficiently accurate and used in this study.

2. The results of the rigid RANS simulations and flexible RANS-FEM simulations correspond to the results found in literature. The same equilibrium deflection of 0.024 m and a response frequency of 2.73 Hz are found. The FSI module of ReFRESCO can therefore be considered accurate for this case.

3. In the sensitivity analysis, damping was added to the system. The damping works, i.e. it damps the response. However, the amount of damping seems incorrect, the influence of added Rayleigh damping should be further investigated.

4. It is studied whether the response changes or becomes unstable when different time steps are chosen. A large time step can save time in the propeller study when only the equilibrium response is required. $\triangle t$ of up to 0.1s are analysed and give equal equilibrium results compared to smaller time steps. When the total deformation in time is requested, the time step should be chosen sufficiently small. For this case ensuring at least ten data points in one period, based on the natural frequency, is a suitable rule of thumb. However, a very small time step can lead to inaccuracies in the pressure signal, which occurred for $\triangle t$ = 0.001 s, the cause for these inaccuracies is not clear and should be further investigated.

5. The size of the RBF radius is important ensuring accurate interpolation across the interface. The largest element size of both grids is present for the FE model of 0.0005 m, with aspect ratio of one. It was expected that an RBF radius that reaches several elements would suffice. However, an RBF radius larger than 0.2 m was necessary, this was due to the geometry of the plate that contained right angles at the top, impossible for the interpolation to solve for low RBF radii.

With the benchmark case the FSI module of ReFRESCO is tested thoroughly, due to the benchmark case several updates were performed that have improved the FSI module. More insight is gained in CFD and FSI of ReFRESCO. Next to that, the problems still present in the module are identified, such as the inaccuracies at small $\triangle t$ and the exact amount of added Rayleigh damping. The benchmark case has led to the conclusion that it can be reliably used in the propeller study.

4

Rigid Propeller Case

In this chapter the rigid propeller study is described. In the introduction it was explained that rigid propeller simulations are carried out to determine the required grid density. The rigid RANS results are compared to experiments and BEM results. Besides that, it is interesting to compare the flexible propeller results. For background information on the geometry and the performance parameters of propellers, one is referred to the introduction, chapter 1. First a description of the rigid propeller case study is given. Then the numerical set-up of the fluid model is explained together with the test conditions and settings corresponding to these conditions. In the last part of this chapter the results are discussed and conclusions are drawn.

4.1. Case Description

The propeller of Greenprop used in this study is a 2-bladed, fixed pitch and right handed propeller with a diameter of 0.34 m. The propeller has considerable skew. The coordinate system is the same as discussed in figure 1.1. The propeller grid is constructed by A. Lampe of MARIN. This fluid grid is explained in the next section. This grid is used to perform simulations with different flow conditions. The open water diagram is constructed and compared to experiments and BEM simulations, both performed by Greenprop.

4.2. Fluid Model

The fluid grid is a multiblock structured grid, created using the program GridPro. The domain and propeller grid are shown in figures 4.1 and 4.2. The domain is circular with diameter and length three and five times the propeller diameter, respectively. The propeller is located in the middle of this domain where refinements are applied in the grid. The inflow and outflow are indicated in figure 4.1. The geometry of the propeller made it difficult to construct a grid of good quality, due to the thin trailing edge and large skew of the blade.

The solution with this grid did not easily converge. In chapter 2, it was explained that a QUICK scheme for the convective flux discretisation is the most accurate. However, as the solution did not converge with the QUICK scheme, a blending scheme was used having a combination between first order upwind- and the central differencing scheme. Consequence of using a blending scheme is that the discretisation error does not decrease as fast as the higher order schemes when the grid is refined.

The boundary conditions applied on the domain and propeller are given in table 4.1. At the in- and outflow the velocity and pressure are imposed. At the inlet this is velocity V_A, which depends on the chosen flow conditions. The pressure at the outlet is set to zero. The propeller and hub both have a wall boundary condition with zero velocity at the wall, i.e. a no-slip boundary condition. At the tunnel a free-slip boundary condition is applied. This means that the velocity normal to the wall will be zero and the velocity tangential to the wall is free [4]. This ensures that the fluid cannot pass through the tunnel wall.

Four grids are obtained by coarsening the finest grid. The amount of cells are given in table 4.3. These four grids are used for the numerical uncertainty analysis as part of the simulations.

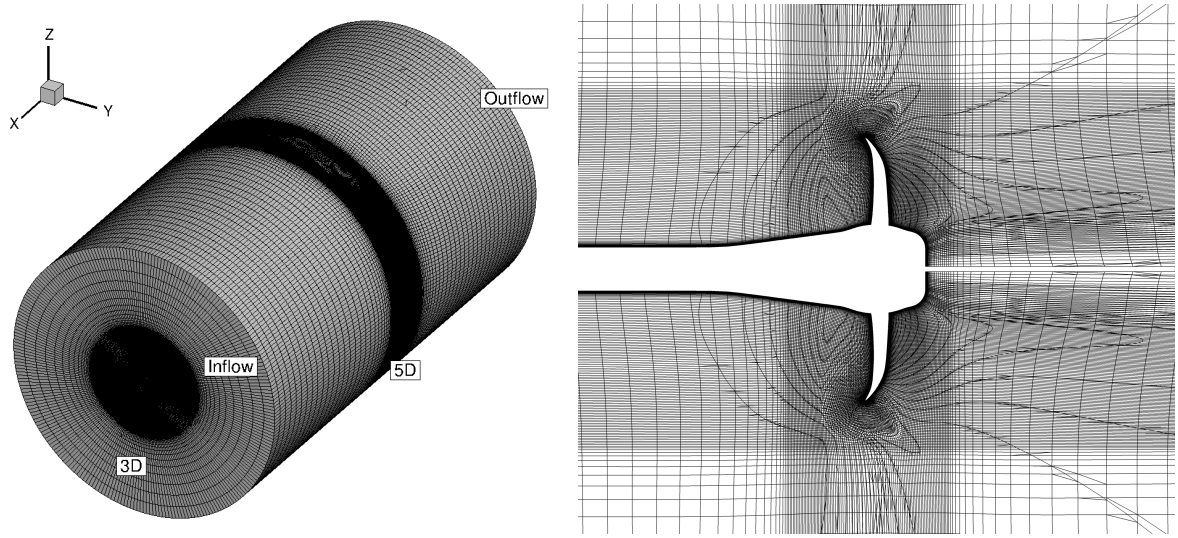

Figure 4.1: Domain and grid around the propeller

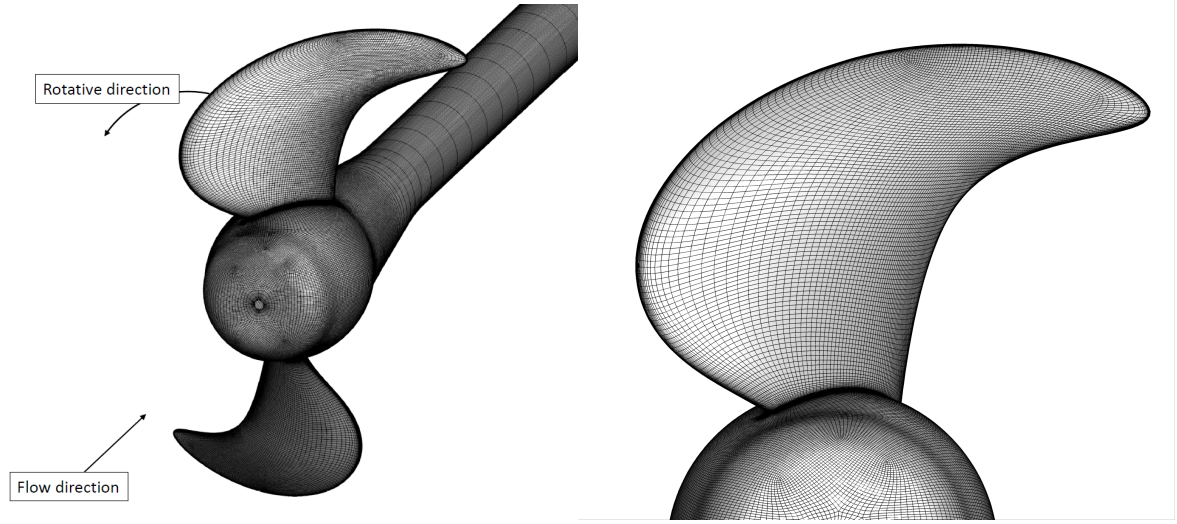

Figure 4.2: Propeller grid and suction side of the upper blade

	Boundary Condition
Inflow	Inflow velocity defined.
Outlet	Pressure is zero at outlet.
Propeller	No slip: Velocity is zero at the wall, No wall functions applied (y+ should be <1).
Tunnel	Velocity normal to the wall is zero, tangential velocity at wall is free.
Hub	No slip: Velocity is zero at the wall, No wall functions applied (y+ should be <1).

Table 4.1: Boundary conditions of fluid grid

4.3. Simulations

The inflow and flow direction are indicated in figures 4.1 and 4.2 with the water flowing in negative x-direction. In open water experiments the hub and shaft of the propeller are reversed. This ensures that the influence of the measuring equipment and shaft are excluded when the propeller is towed trough the water[24]. In the fluid grid, the same configuration is applied. The rotative direction is shown in figure 4.2 as well. Advance ratios ranging from J=0.2 to J=1.1 are chosen to construct the open water diagram. Next to these conditions, the exact same conditions as in the flexible Greenprop simulations are performed. These advance ratios are

J=0.369, J=0.512 and J=0.849. The inflow and rotational velocities are shown in table 4.2. The results that are compared in the rigid propeller study are the thrust, torque and the pressure distribution on the propeller blade.

J	V_A	n_p
0.369	1.88	901
0.512	2.91	1001
0.849	6.74	1400

Table 4.2: Conditions of Greenprop simulations

For the open water diagram, simulations are performed with a constant rotational speed of 1170 rpm and varying inflow velocity V_A to obtain the desired advance ratio J. Advance ratios $J = 0.2$ to $J = 1.1$ are used for comparison with experimental tests and the BEM simulations. By having a constant rotational speed the Reynolds number is kept constant as much as possible for the different conditions. This is due to the Reynolds number being more dependent on rotational speed (n_p) than on inflow velocity (V_A). The Reynolds number is calculated using the chord length at r/R=0.7 ($C_{0.7R}$) and viscosity of the fluid (ν),

$$Re = \frac{C_{0.7R}\sqrt{V_A^2 + (0.7\pi n_p D)^2}}{\nu} \tag{4.1}$$

First, the numerical uncertainty of the calculations is determined. The discretisation error and iterative error of the fluid grid are obtained by performing the numerical uncertainty analysis of Eça and Hoekstra [14].

4.3.1. Settings

For the rigid propeller steady simulations can be performed. The grid domain is circular as visible in figure 4.1. This allows using a moving grid method, where for this case, the interior of the fluid grid domain can rotate around the propeller. The Absolute Formulation Method (AFM) is used with the x-axis as rotating axis[44]. A convergence tolerance of the residuals of 10^{-6} is set.

In section 4.2, it was explained that a Blending scheme is used. For the rigid simulations, the simulation converged if a blending factor of 0.7 was used. However, for the FSI simulations a lower blending factor of 0.5 was required. Therefore, the rigid simulations are also performed with a blending factor of 0.5.

In the open water diagram simulations the k$-\omega$ turbulence model was chosen initially. However, later on during the FSI simulations, the $k-\sqrt{k}L$ turbulence model was found to be more robust. Therefore, the rigid RANS simulations are carried out with the $k-\sqrt{k}L$ turbulence model as well.

4.4. Numerical Uncertainty

The numerical uncertainty of the fluid model is determined using the method of Eça and Hoekstra [14]. This method is explained in section 2.2.3. The four fluid grids that are used differ only in cell density. The number of cells of these four grids is given in table 4.3.

Grid	Amount of cells
A	917,000
B	2,390,000
C	3,790,000
D	9,460,000

Table 4.3: Amount of cells of finest grid (grid D) and coarsened grids

The numerical uncertainty is determined for the thrust and torque of the open water conditions J=0.4, 0.6 and 0.8 and for the Greenprop conditions of J=0.369, 0.512 and 0.849. The numerical uncertainty results are shown in figures 4.3 - 4.6. In these figures, U represents the numerical uncertainty of the finest grid and p the order of accuracy. The numerical uncertainties for thrust and torque are given in figure 4.3 4.4 for J=0.4,0.6

and 0.8 and in figures 4.5 and 4.6 for the Greenprop test conditions of J=0.369, 0.512 and 0.849, for thrust and torque respectively. Other numerical uncertainties determined in this study can be found in appendix C.

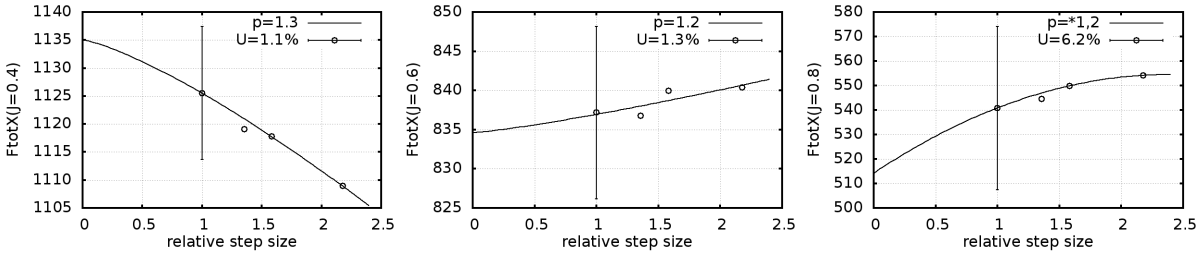

Figure 4.3: Numerical uncertainty thrust, Open water simulations

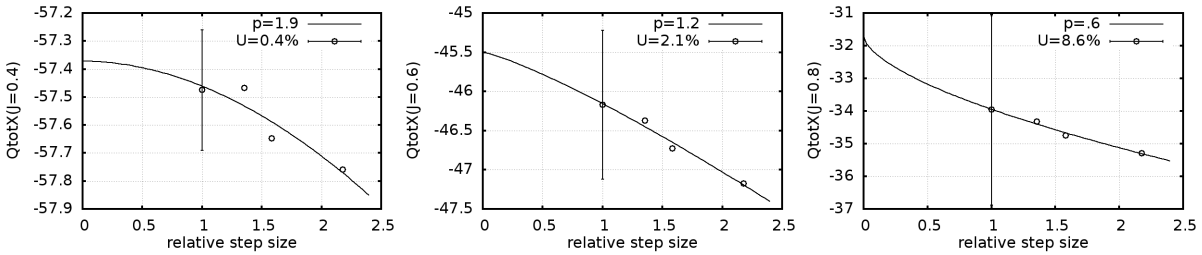

Figure 4.4: Numerical uncertainty of torque, Open water simulations

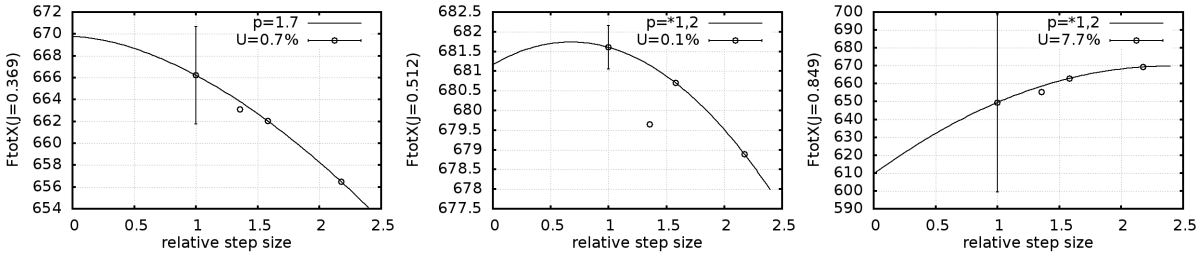

Figure 4.5: Numerical uncertainty of thrust, Greenprop test conditions

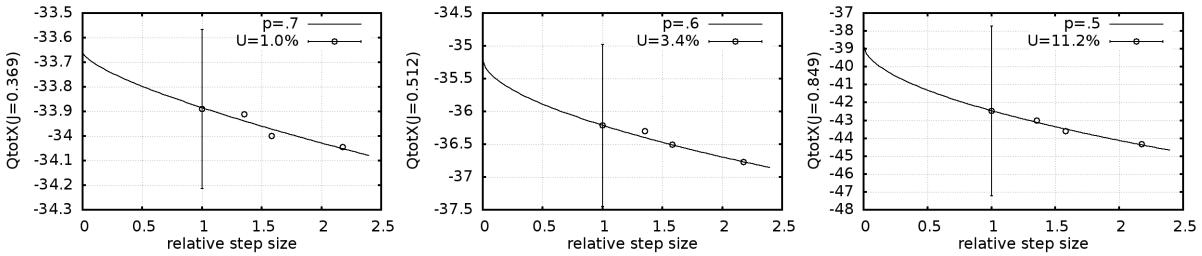

Figure 4.6: Numerical uncertainty of torque, Greenprop test conditions

It is clearly visible that the order of accuracy is lower than two. In the benchmark case an order of accuracy of two was found for the outcomes of the uncertainty analysis. The order of accuracies are in the range of p=0.6 to 1.9. An order of accuracy of p=*1,2 means that a fit was made using first and second order exponents[33]. The order of accuracy is not equal to two, due to the blending scheme used. The uncertainties are between 0.1% and 7.7 % for thrust and between 0.4% and 11.1% for torque. From Klaij et al.[22], it becomes clear that for marine propeller applications a discretisation error of up to 5% is acceptable. The numerical uncertainties of advance ratios J=0.4-0.6 are below 5% and therefore, it is concluded that the finest grid (grid D) is sufficiently accurate for these simulations. For J=0.8 and 0.849 the numerical uncertainties are

between 6.2%-11.1% and therefore larger than 5%. Initially, numerical uncertainties below 5% were found for these advance ratios. However, an error in the use of the method was discovered leading to higher numerical uncertainties. From these results it is recommended to use a finer grid for advance ratios larger than 0.8. However, because this error was identified late in the process the simulations are performed with this grid (grid D) also for advance ratios larger than 0.8. The corrected numerical uncertainties are further used in this study.
The iterative error found for these simulations are at most two orders of magnitude smaller than the discretisation error. The iterative errors for J = 0.369, 0.512 and 0.849 are reported in appendix B.

4.5. Results Open Water Diagram

First the open water diagram is constructed by performing simulations at constant rotative velocity n_p and varying inflow velocity V_A to keep the Reynolds number as constant as possible throughout the different conditions, as explained in the simulations section 4.3. The open water diagram is constructed by expressing the dimensionless thrust (K_T) and torque (K_Q) against the advance ratio.

The results of K_T and K_Q at advance ratios J = 0.2, 0.4, 0.6, 0.8, 1.0 and 1.1 are shown in figure 4.7, indicated by the red line. These values are plotted together with the results of the model tests in the Deepwater Tank (DT) and the BEM simulations with BEM solver Procal, both performed by Greenprop [28]. In this figure, the blue line represents the experimental model tests and the pink line represents the Procal simulations of Greenprop. In table 4.4 the K_T and K_Q corresponding to the red line of the RANS simulations are shown.

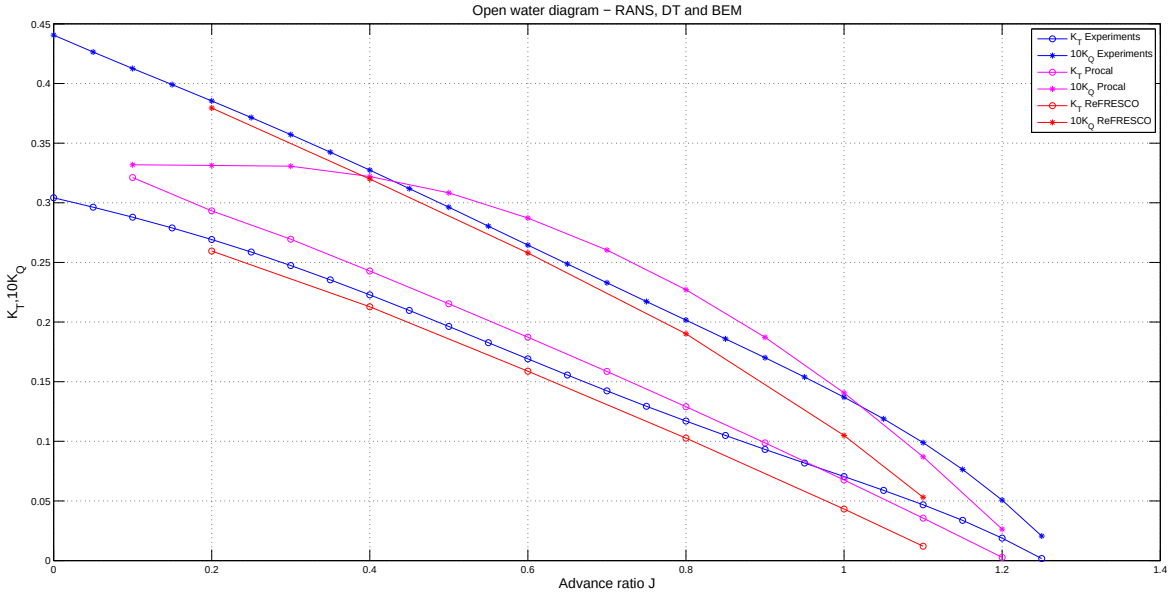

Figure 4.7: K_T and K_Q Experiments, BEM- and RANS simulations

	Kt(RANS)	10Kq(RANS)
J = 0.2	0.260	0.379
J = 0.4	0.213	0.320
J = 0.6	0.159	0.258
J = 0.8	0.103	0.190
J = 1.0	0.043	0.105
J = 1.1	0.012	0.053

Table 4.4: K_T and K_Q Open water diagram of rigid propeller model RANS

In figure 4.8 the differences found for K_T, K_Q are shown for RANS compared to experiments and to BEM results. These differences are discussed in sections 4.7 and 4.8, respectively.

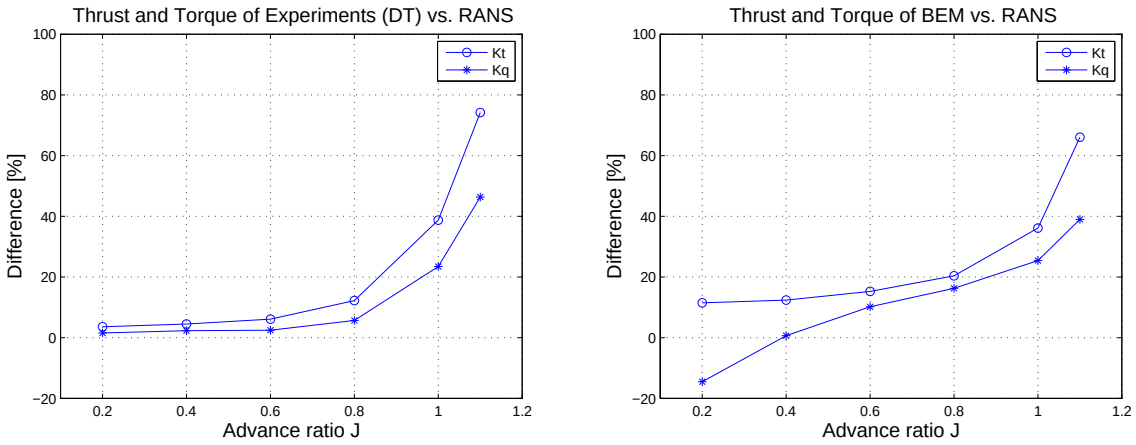

Figure 4.8: Difference between RANS and model tests in the DT (left) and RANS and BEM (right)

4.6. Results Greenprop Conditions

In this section results of the simulations with the Greenprop test conditions are presented. The three tests that are performed are shown in table 4.2 and have advance ratios of 0.369, 0.512 and 0.849. The results for K_T and K_Q are shown in table 4.5. The streamlines on the suction side of the propeller show a similar pattern for J=0.369 and J=0.512, which is visible in figure 4.9.

	K_T(RANS)	$10K_Q$(RANS)
J = 0.369	0.221	0.331
J = 0.512	0.184	0.287
J = 0.849	0.089	0.172

Table 4.5: K_T and K_Q of rigid propeller RANS simulations

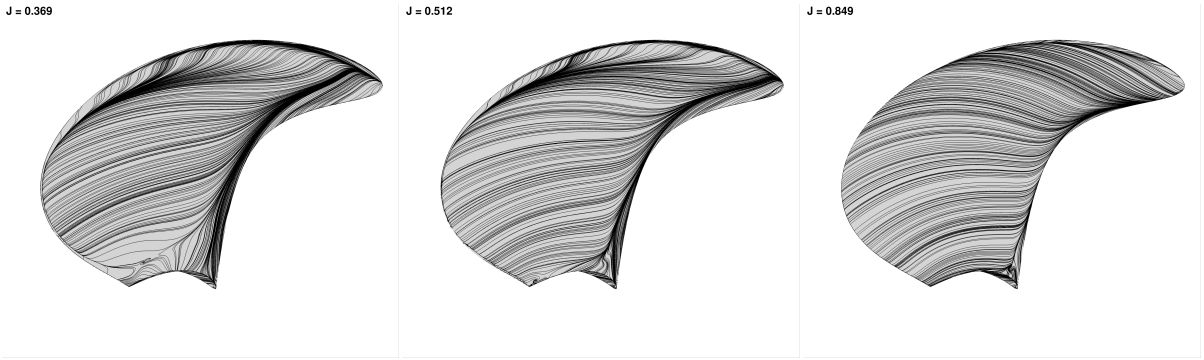

Figure 4.9: Streamlines on the suction side for J=0.369, J=0.512 and J=0.849

4.7. Discussion RANS versus Experiments

The results of K_T and K_Q found with RANS are compared to the results of the experiments. In figure 4.8 the deviations of RANS compared to the experiments is shown in percentage. These values are given in table 4.6 as well.

	Kt(DT)	Kt(RANS)		10Kq(DT)	10Kq(RANS)	
J = 0.2	0.269	0.260	-3.3 %	0.385	0.379	-1.6 %
J = 0.4	0.223	0.213	-4.5 %	0.327	0.320	-2.1 %
J = 0.6	0.169	0.159	-5.9 %	0.265	0.258	-2.6 %
J = 0.8	0.117	0.103	-12 %	0.202	0.190	-5.9 %
J = 1.0	0.071	0.043	-39 %	0.137	0.105	-23 %
J = 1.1	0.047	0.012	-74 %	0.099	0.053	-46 %

Table 4.6: K_T and K_Q Open water diagram of rigid propeller model tests compared to RANS

It is assumed that the experiments in the Deepwater Tank (DT) at MARIN performed with the bronze propeller are accurate. MARIN has a lot of experience in performing open water tests for research and commercial purposes. Three tests were performed in the DT, the method of testing is described in the report of Lafeber et al. [24]. The largest difference in the measured K_T was 1.7% and 1.1% for K_Q. It is therefore assumed that the results of the model tests are within 2% accurate. Next to this error present in the repeated tests, there is an error in the measuring equipment and sensors. It is assumed that this error is approximately 1%. Therefore, a total uncertainty of the DT tests of 3% is assumed. The bandwidth of 3% around the DT results of K_T and K_Q is shown in figure 4.10. The bandwidth around the RANS results are the numerical uncertainty results of section 4.4. If these uncertainty bandwidths overlap, the results of RANS and experiments are considered to be equal.

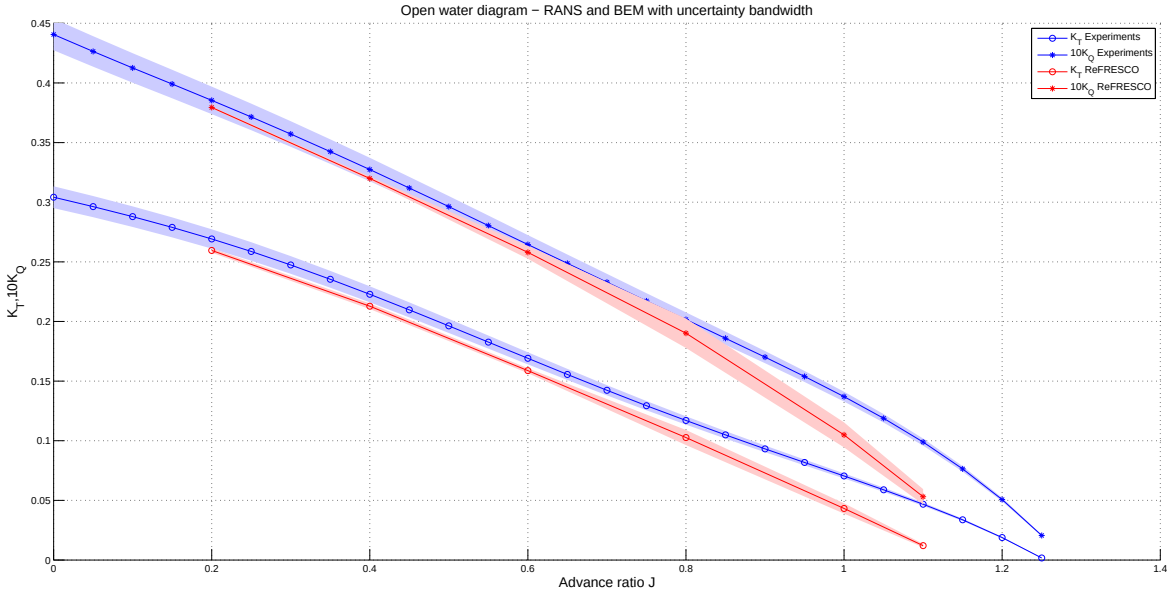

Figure 4.10: Openwater diagram with uncertainty bandwidths

For advance ratios up to 0.8, the K_Q bandwidths overlap and are therefore considered equal. K_T only shows overlap for J=0.2, for advance ratios 0.4, 0.6 and 0.8 lower values for K_T are found by RANS of 0.4%, 2% and 4%, respectively. For the results of advance ratios 1.0 and 1.1, larger deviations are found both in K_Q and K_T. For RANS K_Q is 12% and 36% lower compared to the K_Q results of the experiments. For K_T lower values of 29% and 68% compared to the experiments are found. These lower results for K_T and K_Q can have several causes,

1. Influence of tunnel walls: The simulations are performed in a circular fluid domain. The experiments are performed in a normal towing tank without influences of the tunnel the so-called blockage.
2. Modelling errors: Wrong modelling of transition from laminar to turbulent flow by the turbulence model in ReFRESCO.
3. Experimental errors: The tests in the DT are chosen for comparison. Despite the experience of MARIN, experimental errors are made in these tests, which can lead to deviations in the results.

These three possible causes for differences between RANS simulations and model tests are now further analysed. First, the influence of tunnel walls or so-called blockage is discussed.

4.7.1. Blockage

The experiments with the bronze propeller are performed in the Deepwater Tank (DT) which is an open basin compared to the circular fluid domain used in the RANS simulations. To analyse whether the influence of blockage leads to the lower K_T and K_Q for higher advance ratios, the results are compared to the open water diagram obtained in the Cavitation Tunnel (CT). The experiments performed with the epoxy propeller are performed in the CT. Beforehand, reference tests were carried out with the bronze propeller to verify the open water diagram with the DT. Therefore the open water diagram tested in the CT is available as well. It should be noted that the CT is not used on a daily basis. The actual flow velocity V_a can deviate from the measured flow velocity. The reason that the open water diagram of the DT is analysed first, is that at MARIN open water tests are usually performed in the DT and measurement equipment is more up-to-date.

The difference with the cavitation tunnel in real life and the circular grid domain is that the tunnel is not cylindrical. Reason for this difference is that for the use of the moving grid method in ReFRESCO, as explained in the settings section 4.3, a circular domain is needed to be able to use the moving grid method. Another parameter that is different in the CT compared to the simulations in ReFRESCO, is the arrangement of flow velocity V_A and rotation speed n_p. In the CT it is easier to adjust n_p compared to V_A. For V_A the entire flow velocity of the tunnel has to be adjusted, whereas the rotational velocity of the propeller can be adjusted easily. In ReFRESCO, n_p is kept constant while V_A is varied. The Reynolds number is more sensitive for rotational velocity compared to the V_A, which becomes clear from equation 4.1. For J = 0.8 the RANS simulations are performed with constant n_p of 19.83 rps and V_A of 5.4 m/s, leading to a Reynolds number of 1.78E6. The CT tests are either performed with constant V_{Tunnel} of 2 m/s and 6 m/s, and corresponding Reynolds numbers of 6.6E5 and 1.98E6 respectively. This can have a considerable effect on the results. The results from the cavitation tunnel are highly velocity dependent, as for same advance ratios J, different results are found. It is assumed that the flow is uniform throughout the tunnel, however, vortices/swirls were visible during the tests. These differences and inaccuracies of the CT have to be taken into account in further analysis.

The results of the tests in the CT are shown in figure 4.11, indicated with the green lines. The different signs on the green lines correspond to the water velocity in the tank. The results of the DT tests and ReFRESCO simulations are shown as well. The test results of the CT are closer to the simulation results for J>0.8. For J=1.1, the deviation of the RANS results are -26% for K_Q and -35% for K_T. This is lower compared to the deviations in the DT results i.e. -46% and -74% for K_Q and K_T, respectively. It can be concluded that blockage is a plausible reason for the deviation at advance ratios larger than 0.8. A recommendation for future work is to study the influence of blockage when a larger diameter is chosen for the fluid grid domain, it is expected that the simulation results with a larger domain are closer to the DT results, excluding the effect of blockage.

4.7.2. Modelling Errors

Transition from laminar to turbulent flow plays an important role in properties of the flow and loads on the propeller blade [15]. Turbulence models were not designed to accurately model the transition from laminar to turbulent. Rijpkema et al [38], investigated the application of surface roughness at the leading edge, resulting in earlier transition to turbulent flow. This gave better comparable results between ReFRESCO simulations and experiments looking at limiting streamlines and paint tests.

To analyse the influence of the turbulence model on the flow and prediction of the thrust and torque, simulations are performed with varying Reynolds numbers. Simulations at J = 0.8 and J = 1.0 are performed with Reynolds numbers ranging from 1E4 - 1E7 obtained by varying the dynamic viscosity from μ = 0.1807 -

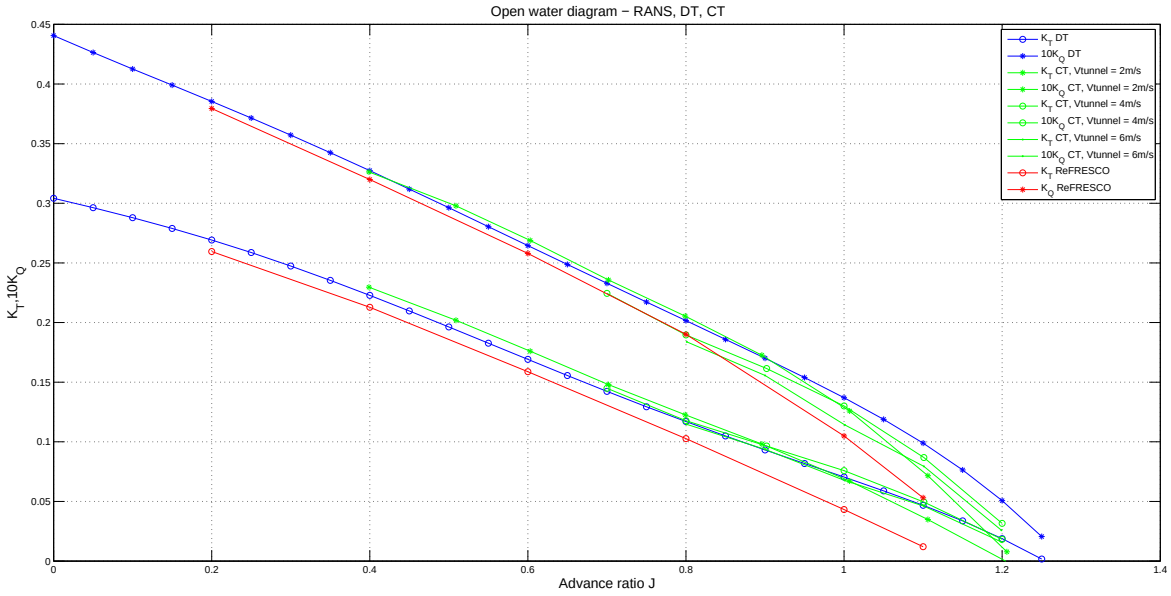

Figure 4.11: K_T and K_Q compared to experimental results in the DT and in the CT

1.807E-4, for J=0.8. For J =1.0 a simulation with Reynolds 1E7 is performed obtained with μ= 8.65E-4.

Note that when the Reynolds number is a factor 10 higher, the y-plus value will also be a factor 10 higher. The maximum y-plus value for the Re=1E7 becomes 1.8, and is assumed to be close to one. Therefore, the grid is not refined for this purpose. It is expected that more turbulent flow is present on the blade for this higher Reynolds number. The turbulence model will be able to better predict the loads on the blade, leading to results that are closer to the experimental results.

The results limiting streamlines for Re=1E6 and 1E7 are shown in figure 4.12 for J=0.8. The limiting streamlines on the blade show a higher extent of laminar separation at the trailing edge for the lower Reynolds number. The flow for the higher Reynolds number is less radially directed at the trailing edge, indicating more turbulent flow. For higher Reynolds number at J=0.8 there is an increase of 4.8 % and 2.4 % for K_T and K_Q respectively. For J = 1.0 this is 6.4 % and 2.2 %. Especially for K_T the results found with higher Reynolds number are closer to the experiments. The transitional flow from laminar to turbulent is therefore a plausible reason for the large difference between RANS simulations and experiments for this propeller.

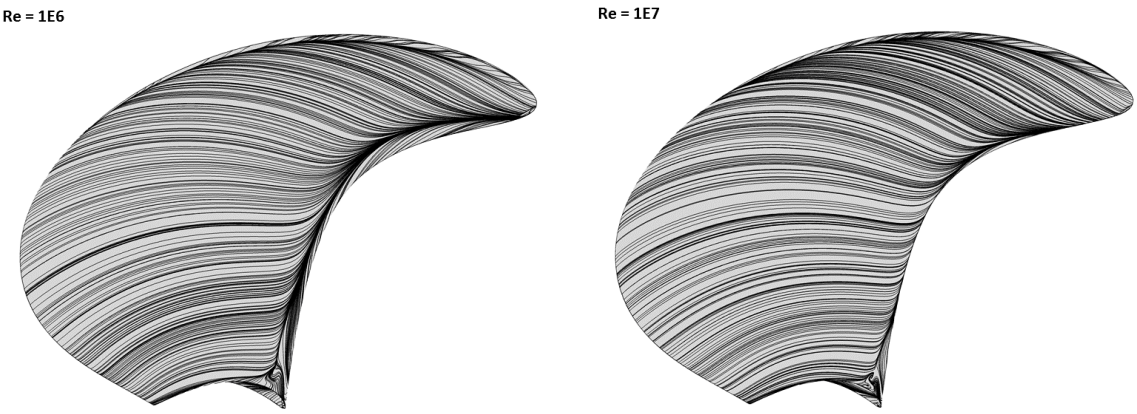

Figure 4.12: Limiting streamlines on suction side for J=0.8 with μ= 1.807E-3 (left) μ= 1.807E-4 (right)

4.7.3. Experimental Errors

During the RANS simulations the propeller is not allowed to deform. It is assumed that the deformation of the bronze propeller in the model tests can be neglected as well. However, in reality this propeller will slightly deform in response to the hydrodynamic loading. To get an idea of this deformation the pressure on the blade obtained from the RANS simulations is applied to the FEM model, but now with material properties of bronze, i.e. ρ = 7590 kg/m^3, E = 125 GPa and ν = 0.32. The ANSYS model showed a maximum deformation of 0.17 mm of the bronze propeller. This deformation is small but can give slight changes in measured thrust and torque. However, it is expected that this deformation will lead to lower thrust and torque, and is therefore not a cause of the higher thrust and torque measured in the experiments.

In the paper of Lafeber it is also mentioned that other errors in the experimental tests can be present, such as sensor calibration, sensor drift and polynomial fitting of the results[24]. These errors are accounted for through the uncertainty bandwidth. It is assumed that these errors do not influence the thrust and torque more than this bandwidth and are not the cause for the differences at advance ratios larger than 0.8.

From the comparison of the RANS simulations with the experiments in the DT, it can be concluded that for advance ratios up to 0.8 a good resemblance is found for K_Q and K_T. The uncertainty bandwidths overlap for K_Q and for K_T a maximum deviation of 4% is found. For larger advance ratios, deviations in the range of 12-68% are found. These differences are attributed to blockage and the wrong modelling of the transition from laminar to turbulent by the turbulence model in ReFRESCO. In the next section, the RANS results are compared to BEM.

4.8. Discussion RANS versus BEM

In this section, the results obtained with RANS for the open water- and Greenprop conditions are compared to the BEM results obtained by Greenprop. The results of thrust and torque and the pressure distributions of RANS and BEM are compared.

4.8.1. Thrust and Torque

From the open water diagram of figure 4.7 it becomes clear that K_T and K_Q of RANS are close to the experimental results for advance ratios up to 0.8. At J=0.2 the largest difference is visible of RANS compared to experiments is visible of -1.5% for K_Q and -3.6% for K_T. This is -14% for K_Q and 8.9% for K_T. In figure 4.8 the difference of RANS compared to BEM results is shown as a percentage. These values are given in table 4.7. It should be noted that the numerical uncertainty bandwidth is not taken into account in this analysis, the mean values are used for comparison. Especially at low advance ratio the results of BEM deviate from the model tests and RANS results. This can be attributed to the flow separation being present at high angles of attack (low advance ratio J), that is not captured by BEM.

	Kt(BEM)	Kt(RANS)		10Kq(BEM)	10Kq(RANS)	
J = 0.2	0.293	0.260	-11 %	0.332	0.379	+14 %
J = 0.4	0.243	0.213	-12 %	0.322	0.320	-0.6 %
J = 0.6	0.187	0.159	-14 %	0.287	0.258	-10 %
J = 0.8	0.129	0.103	-20 %	0.227	0.190	-16 %
J = 1.0	0.068	0.043	-36 %	0.141	0.105	-25 %
J = 1.1	0.036	0.012	-66 %	0.087	0.053	-39 %

Table 4.7: Kt and Kq Open water diagram of rigid propeller BEM compared to RANS

For the Greenprop test conditions the RANS results are compared to BEM as well. These results are shown in table 4.8. Deviations in the same range of table 4.7 are found.

To analyse the cause for these differences the pressure distributions of RANS and BEM are compared in the next section. The Greenprop conditions of J=0.369, 0.512 and 0.849, are chosen for comparison.

	K_T(BEM)	K_T(RANS)	%	$10K_Q$(BEM)	$10K_Q$(RANS)	%
J = 0.369	0.250	0.221	-12 %	0.342	0.331	-3 %
J = 0.512	0.209	0.184	-12 %	0.307	0.287	-7 %
J = 0.849	0.113	0.089	-21 %	0.204	0.172	-16 %

Table 4.8: K_T and K_Q of rigid propeller RANS compared to BEM

4.8.2. Pressure Distribution

The pressure distributions of advance ratio J=0.369 for RANS and BEM are shown in figures 4.13 and 4.14 for the suction- and pressure side, respectively. The dimensionless pressure coefficient (C_{pn}) is used as parameter,

$$C_{pn} = \frac{p - p_{ref}}{\frac{1}{2}\rho(n_p D)^2} \tag{4.2}$$

in which p is the pressure on the blade and p_{ref} the reference pressure in the farfield, which is assumed to be zero. The pressure distribution C_{pn} is also expressed at certain radii against the chord length (x/c), for RANS (ReFRESCO) and BEM (Procal) in figure 4.15. Radii (r/R) of 0.605, 0.809 and 0.960 are chosen to display.

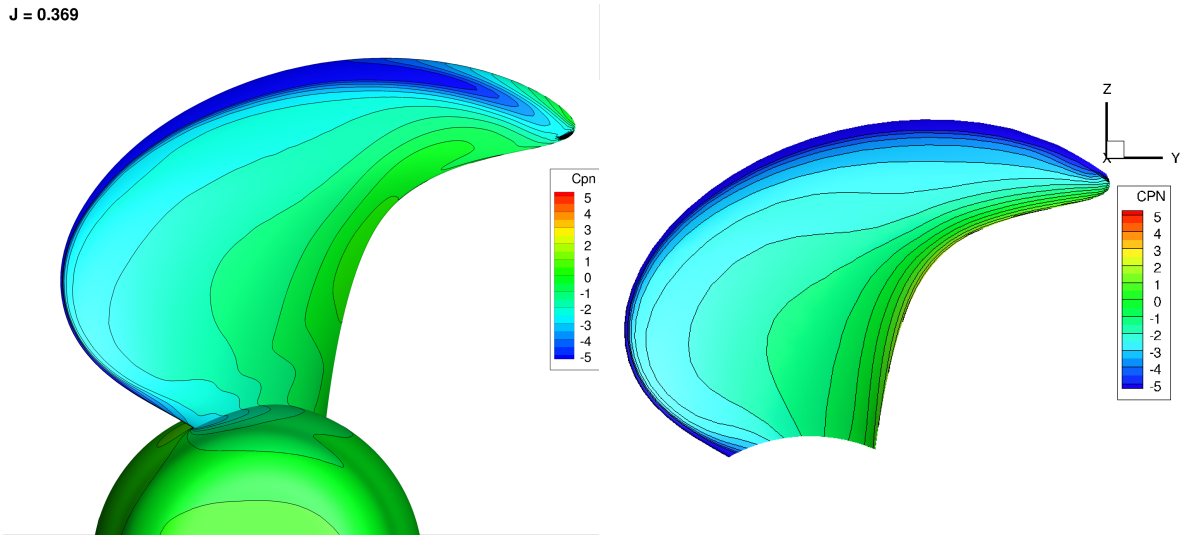

Figure 4.13: Pressure distribution (Cpn) on the suction side for J = 0.369 RANS (left) and BEM (right)

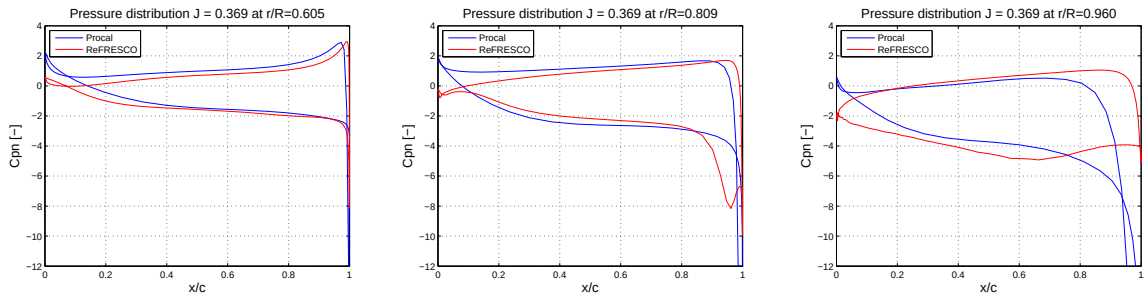

Figure 4.15: Pressure distribution r/R = 0.605, 0.809, 0.960 for J = 0.369

From the pressure distribution at the suction side (figure 4.13), it becomes clear that the suction peak of BEM reaches the tip, which is not the case for RANS. The reason for this is that in BEM there is no tip vortex. Therefore the pressure at the tip is different compared to RANS. This pressure difference at the outer radius

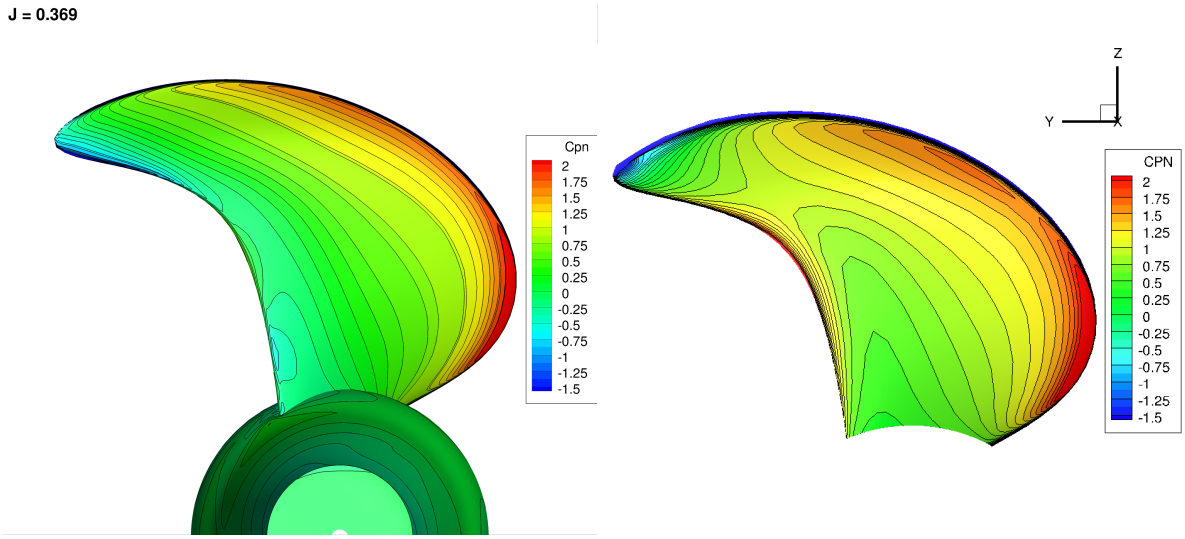

Figure 4.14: Pressure distribution (Cpn) on the pressure side for J = 0.369 RANS (left) and BEM (right)

can be the reason for the deviation in torque. It is expected that this will have a large impact on the tip deformation in the flexible propeller case for RANS-FEM compared to BEM-FEM.

If the suction sides are compared to the pressure sides of figure 4.14, it becomes clear that the overall pressure of RANS is lower. This is the cause for the lower thrust of RANS compared to BEM. Next to that, the pressure distribution is more concentrated at the leading edge for RANS, compared to the more dispersed distribution of BEM. Another difference from these distributions is that the flow around the propeller at the tip is different for the two solvers.

For advance ratios J= 0.512 (figure 4.16 and 4.17) comparable pressure distributions are found for the suction- and pressure side. For advance ratio J = 0.849, a different pressure distribution is found compared to J=0.369 and 0.512. The high advance ratio corresponds to a small angle of attack, leading to a lower loading on the blade. When the BEM and RANS pressure distributions are compared for J=0.849, a similar distribution is found. However RANS shows a lower overall pressure. This corresponds to the lower thrust and torque results found for RANS compared to BEM.

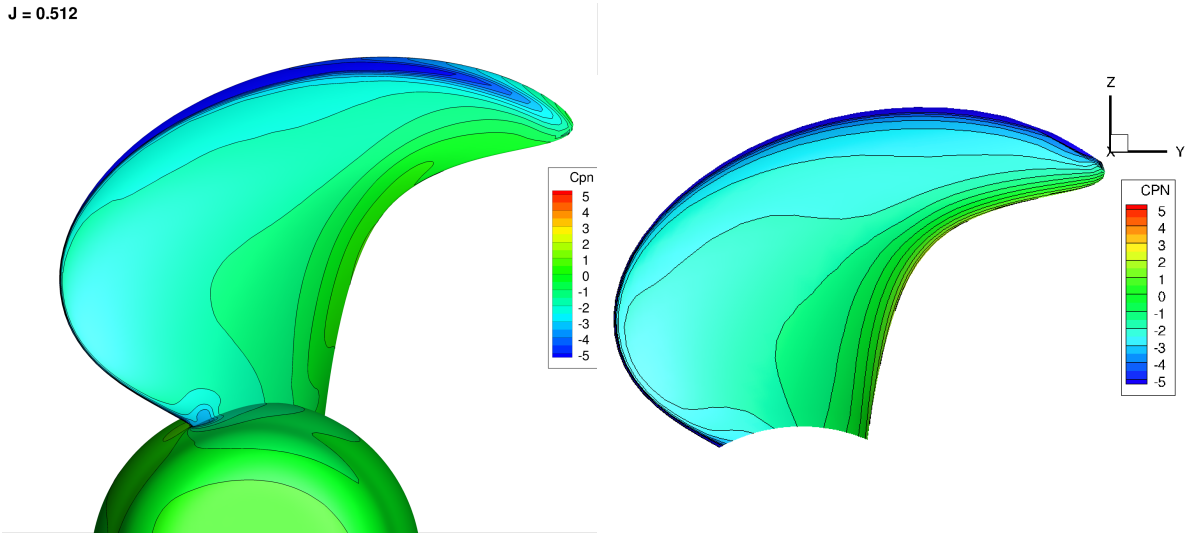

Figure 4.16: Pressure distribution (C_{pn}) on the suction side for J = 0.512 RANS (left) and BEM (right)

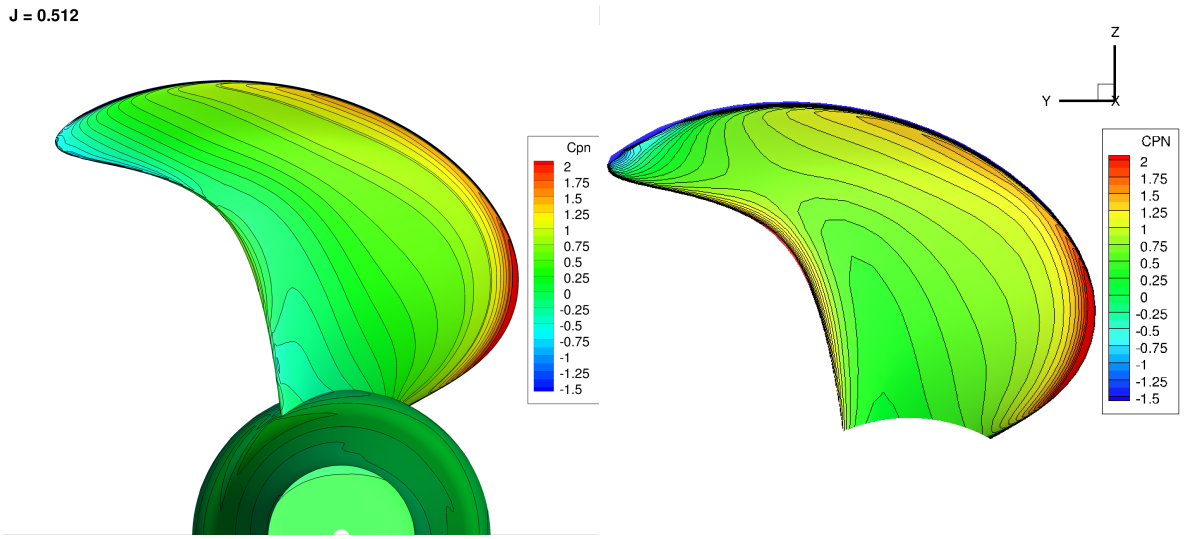

Figure 4.17: Pressure distribution (C_{pn}) on the pressure side for J = 0.512 RANS (left) and BEM (right)

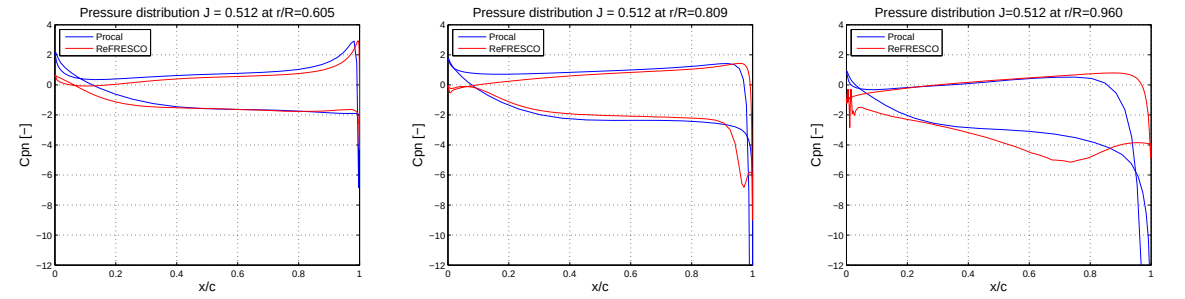

Figure 4.18: Pressure distribution r/R = 0.605, 0.809, 0.960 for J = 0.512

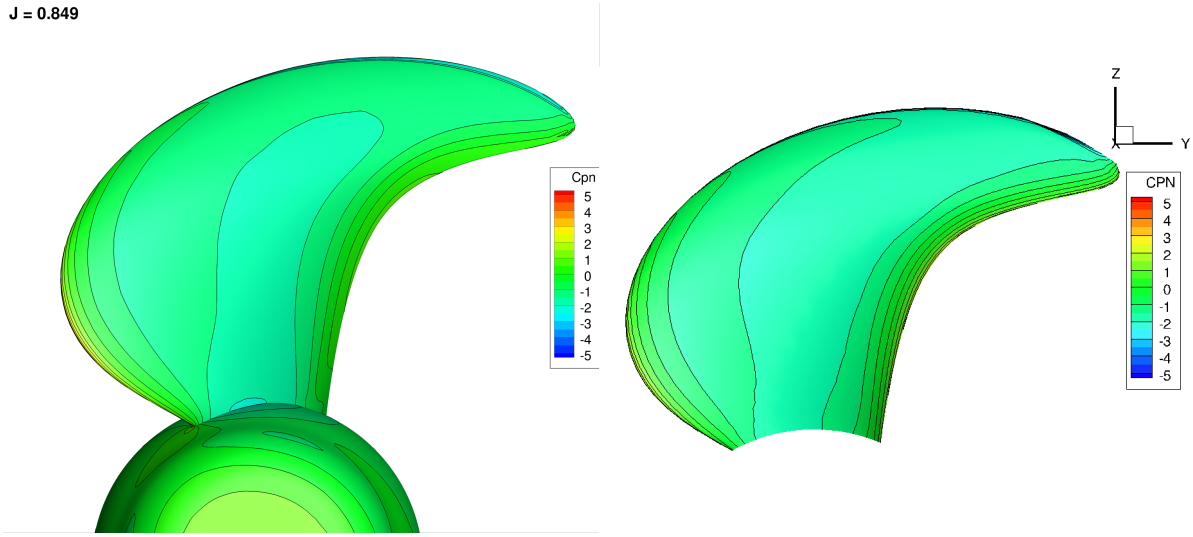

Figure 4.19: Pressure distribution (C_{pn}) on the suction side for J = 0.849 RANS (left) and BEM (right)

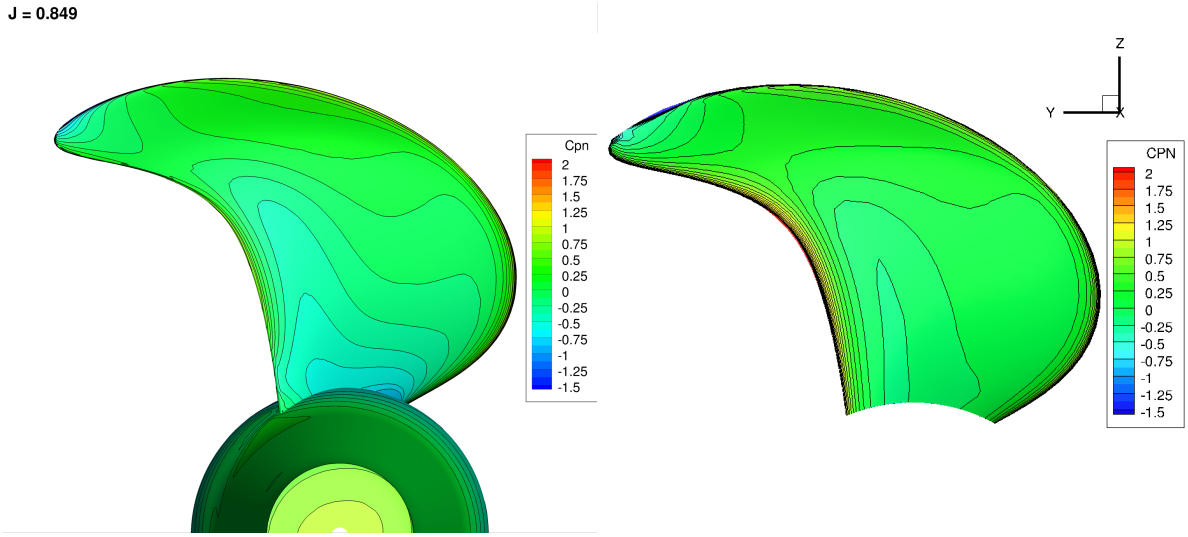

Figure 4.20: Pressure distribution (C_{pn}) on the pressure side for J = 0.849 RANS (left) and BEM (right)

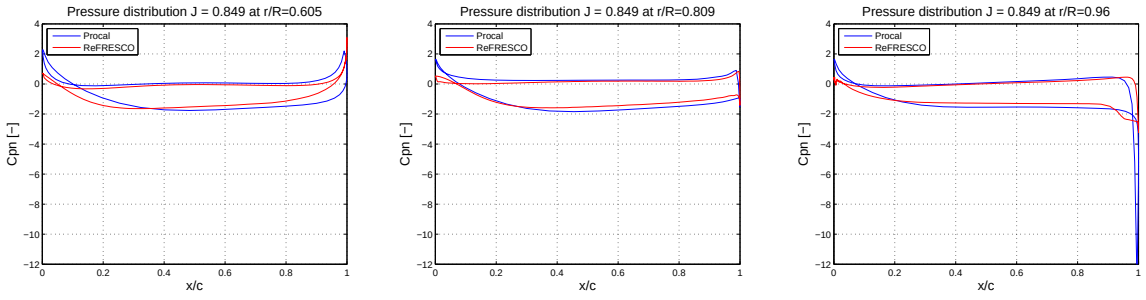

Figure 4.21: Pressure distribution r/R = 0.605, 0.809, 0.960 for J = 0.849

4.9. Summary and Conclusions

In this chapter RANS simulations are performed with the rigid propeller of Greenprop. The open water diagram is constructed with advance ratios ranging from J=0.2 to J=1.1. The results are compared to experiments and BEM simulations, both performed by Greenprop. Next to that, simulations with conditions of the Greenprop tests are performed to compare to BEM and to the flexible results later on. These simulations consisted of advance ratios J=0.369, 0.512 and 0.849. The conclusions from this chapter are divided in numerical uncertainties, RANS compared to experimental results and RANS compared to BEM results.

1. The numerical uncertainties are between 0.1% and 7.7 % for thrust and between 0.4% and 11.1% for torque. From Klaij et al.[22], it becomes clear that for marine propeller applications a discretisation error of up to 5% is acceptable. The numerical uncertainties of advance ratios J=0.4-0.6 are below 5% and therefore, it is concluded that the grid is sufficiently accurate for these simulations. For J=0.8 and 0.849 the numerical uncertainties are between 6.2%-11.1% and therefore larger than 5%. Initially, numerical uncertainties below 5% were found for these advance ratios. However, an error in the use of the method was discovered leading to higher numerical uncertainties. From these results it is recommended to use a finer grid for advance ratios larger than 0.8. However, because this error was identified late in the process the simulations are performed with this grid also for advance ratios larger than 0.8.

2. The results of the RANS simulations and the measured open water diagram in the DT tank show for an advance ratio of J>0.2 larger differences in K_T than expected from the numerical and experimental uncertainties. For advance ratios 0.4, 0.6 and 0.8 lower values for K_T are found by RANS of -0.4%, -2% and -4%, respectively. For advance ratios of 1.0 and 1.1 larger deviations both in K_Q and K_T are observed. For RANS, K_Q is -12% and -36% compared to the experiments. For K_T deviations of -29% and -68% are found. These lower results for K_T and K_Q can have several causes. The influence of blockage is discussed by comparing to tests in the cavitation tunnel with the bronze propeller and the modelling and experimental errors are discussed. The most likely reasons for the lower K_T and K_Q are blockage of the fluid domain and the turbulence model in ReFRESCO. It is recommended to further study the deviations compared to experiments for advance ratios larger than 0.8.

3. The comparison of RANS with BEM results shows that for advance ratios up to J = 0.8, RANS better predicts the load on the blade compared to BEM. The largest difference is visible for J=0.2, the results of RANS are -1.5% and -3.6% compared to the experiments for K_Q and K_T respectively. For BEM this is -14% and +8.9%. This difference is assigned to the flow separation at large angles of attack, i.e. low advance ratios. This flow separation is a viscous effect that is not captured by BEM. When the pressure distributions of RANS and BEM are compared, it becomes clear that the suction peak of BEM reaches the tip, whereas this is not the case for RANS. The reason is that in BEM there is no tip vortex leading to a different pressure at the tip compared to RANS. This pressure difference at the outer radius can be the reason for the deviation in torque, which is -3% to -16% lower for RANS. The pressure distributions for RANS and BEM showed a lower pressure overall leading to a lower thrust of -12% to -21% for RANS.

From the simulations performed in this chapter, knowledge is gained in propeller simulations with RANS. The accuracy of the RANS results is determined by evaluating the numerical uncertainty and comparing to experimental results. Next to that, a comparison is made between the results of BEM. The numerical uncertainties and performance parameters found for the rigid propeller are used in the flexible propeller study.

5

Flexible Propeller Case

In this chapter the flexible propeller case is discussed. RANS-FEM simulations are performed with the epoxy propeller of Greenprop. First a short case description is given, then the grid study of the FEM model is explained and the conditions and settings of the RANS-FEM simulations are outlined. The results of the simulations are compared to the experiments and BEM-FEM simulations, both performed by Greenprop with the epoxy propeller.

5.1. Case Description

The propeller geometry is described in chapter 4. The propeller material is epoxy, with elastic modulus of $E = 3.6$ GPa and a density of $\rho = 1140$ kg/m^3. The fluid grid that is used in the RANS-FEM simulations is described in section 4.2. For the flexible simulations, taking into account Fluid-structure interaction, the FEM model is included. For this structural model Finite Element solver ANSYS is used, which is described in the next section.

5.2. Structural Model

ANSYS Workbench is used for the FE modelling of the propeller. Eigenfrequencies of a structure are dependent on the mass- and stiffness matrix, which was pointed out in section 2.3. The matrices are part of the equations of motion. If the eigenfrequencies of the ANSYS model are equal to those of Greenprop it can be concluded that the response corresponds as well. Therefore, the eigenfrequencies are chosen as parameters for comparison between the FE and physical model of Greenprop.

The first 5 eigenfrequencies of Greenprop are shown in table 5.1. The eigenfrequencies found for the Greenprop model are obtained by modal analysis in the FE solver. The natural frequencies of the physical model are obtained through experimental tests. From these experimental tests, only the first two eigenfrequencies are measured. These tests were only performed as check and it is expected that the uncertainty is 5%, this leads to a bandwidth around the natural frequency of 295 to 352 Hz for the first mode. However, the natural frequencies of the Greenprop FE model are aimed for in the FE modelling of this study. Before the structural model is constructed several requirements of the model are set. The model should,

- be sufficiently accurate, especially at the tip, leading edge and trailing edge;
- have eigenfrequencies that are within 5% compared to the Greenprop FE model.

In chapter 2 it was explained that in the FSI module of ReFRESCO, solid elements should be used for the FE model. Quadratic solid elements (SOLID186) are chosen for the modelling of the propeller structural grid. In the Benchmark case of chapter 3, it was shown that the use of these elements resulted in a more accurate solution than linear solid elements. The material of the propeller is assumed to be isotropic with elastic modulus, density and poisson ratio of epoxy. The hub is excluded from the structural model and clamped boundary conditions are applied on the root of the blade at its connection to the hub. Meshes obtained with three different mesh methods are considered, these methods are explained first.

Meshes obtained with the Sweep-, Multizone- and Hex dominant method of ANSYS Workbench are considered. The sweep method is used if the geometry is recognised as a sweepable body. Two opposite faces (source- and target face) are chosen. On the source face a quadrilateral or triangular mesh is generated that is copied to the target face generating the mesh between the source- and target face [40]. The multizone method divides the geometry in sweepable bodies if it does not consist of one sweepable body. The hex dominant method will create a hexahedral mesh for bodies that cannot be swept. This method is suitable for bodies with a large interior volume. For thin structures and bodies that are easily swept, the hex dominant method is less suitable [40]. It is expected that the propeller geometry is a sweepable body with the pressure- and suction side as source- and target face. Therefore, the sweep mesh method will be most suitable. However, all three methods are considered to study the effect on element distribution and response.

Mode	Greenprop [Hz]	Exp. [Hz]
1	318	310
2	460	454
3	799	
4	1085	
5	1331	

Table 5.1: Eigenfrequencies found in experiments and modal analysis of Greenprop FE model

In ANSYS a linear elastic analysis is performed. Greenprop investigated whether this is a valid assumption for the epoxy propeller by comparing results of linear elastic analysis and geometric non-linear analysis. It was concluded that linear elastic propeller analysis is a valid assumption [28].

5.2.1. Grid Study

From the grid study of the benchmark case of section 3.2 it was concluded that an aspect ratio of 1 gives the best result. For the structural model of the propeller, element sizes are chosen such that the aspect ratios of the elements are close to one. The best fit of multizone-, hex dominant- and three sweep meshes are shown in table 5.2. The eigenfrequencies are compared to those of the Greenprop FE model and the deviation is indicated as a percentage. It is assumed that the response of the FE model corresponds to the Greenprop FE model if the eigenfrequencies are within 5% from the Greenprop FE model.

From the eigenfrequencies it becomes clear that all meshes are within 0.4% from the first natural frequency of the Greenprop model. The quality of the elements at the tip, leading- and trailing edge are compared. In figure 5.1 the tip elements of the multizone method are shown. With this method not enough resolution at the tip is obtained. This made the multizone method not suitable. The hex dominant method created more elements through thickness, leading to three elements in thickness. However, the mesh obtained with this method showed not enough resolution at the tip, which is visible in figure 5.2. The sweep mesh method showed the best element distribution. These meshes are shown in figures 5.3, 5.4 and 5.5. The differences between these meshes are the total number of elements and the number of elements through thickness. This is visible in figure 5.5.

When sweep 1, 3 and 3 are compared, it becomes clear that the amount of cells of the first two methods (Sweep 1 and 2) is lower. This is due to the third mesh having two elements through thickness. The element quality which is obtained in ANSYS is the best for Sweep 3. However, the other meshes show better quality at the tip, which is shown in figures 5.6 and 5.7.

The first eigenfrequencies of the three sweep meshes are 0 - 0.4 % higher than the Greenprop frequencies. For the other eigenfrequencies, sweep 1 and 2 are closer compared to sweep 3. When the Sweep 3 mesh was used in ReFRESCO, the RBF method was not capable of solving the interpolation for two elements through thickness at the tip. Therefore, the sweep 2 mesh which shows slightly better element quality compared to sweep 1, is chosen for the RANS-FEM simulations. This final mesh together with its properties are shown in table 5.3 and figure 5.8. The results are discussed in the next section.

Mesh method	**MultiZone**		**Hex. Dom.**		**Sweep 1**		**Sweep 2**		**Sweep 3**	
Element size	0.005	m	0.005	m	0.008	m	0.006	m	0.006	m
Sweep size					0.0005	m	0.005	m	0.0005	m
# elements	473		2577		309		479		962	
# elem. in t	1		3		1		1		2	
Quality [-]	0.691		0.588		0.653		0.659		0.710	
Tip?	–		–		++		++		+	
Freq. [Hz]		%		%		%		%		%
Mode 1	318.8	+0.3	317.7	-0.1	319.3	+0.4	318.9	+0.3	317.9	0.0
Mode 2	455.5	-1.0	453.0	-1.5	457.3	-0.6	456.3	-0.8	453.3	-1.5
Mode 3	775.5	-2.9	772.2	-3.4	775.5	-2.9	773.7	-3.2	771.9	-3.4
Mode 4	1042.7	-3.9	1039.6	-4.2	1042.3	-3.9	1040.3	-4.1	1039.5	-4.2
Mode 5	1296.2	-2.6	1292.9	-2.9	1295.9	-2.6	1292.8	-2.9	1293.1	-2.8

Table 5.2: Grid study different mesh methods, deviation of frequencies compared to GreenProp frequencies

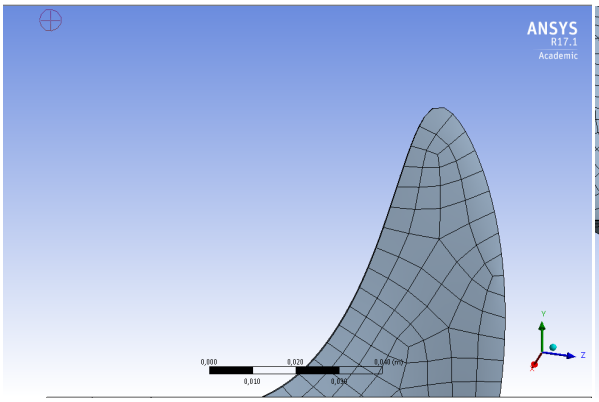

Figure 5.1: Tip elements multizone method

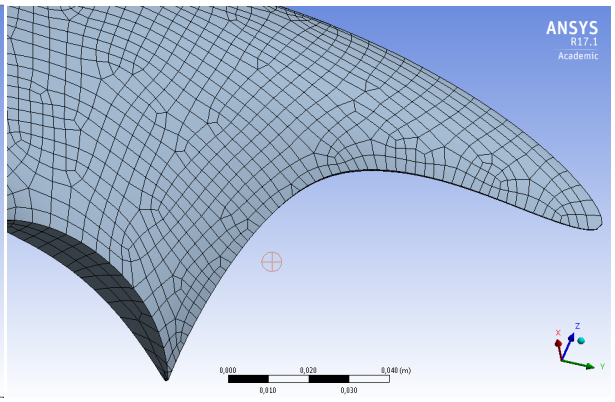

Figure 5.2: Hex. dominant method

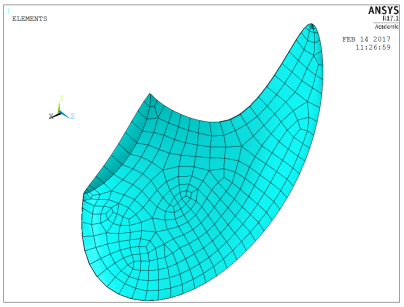

Figure 5.3: Sweep 1

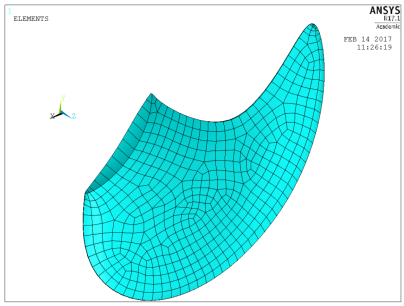

Figure 5.4: Sweep 2

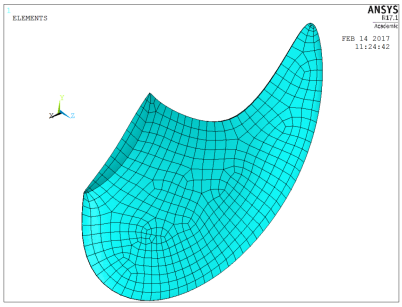

Figure 5.5: Sweep 3

Mesh method	Sweep	
Element size	0.006	m
Sweep size	0.005	m
# of elements	479	
# of elements in t	1	
Frequencies		
Mode 1	318.9	Hz
Mode 2	456.3	Hz
Mode 3	773.7	Hz
Mode 4	1040.3	Hz
Mode 5	1292.8	Hz

Table 5.3: Characteristics and results of ANSYS model

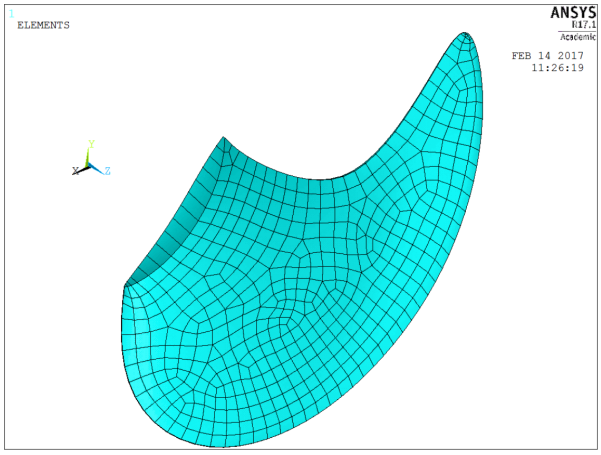

Figure 5.8: ANSYS model

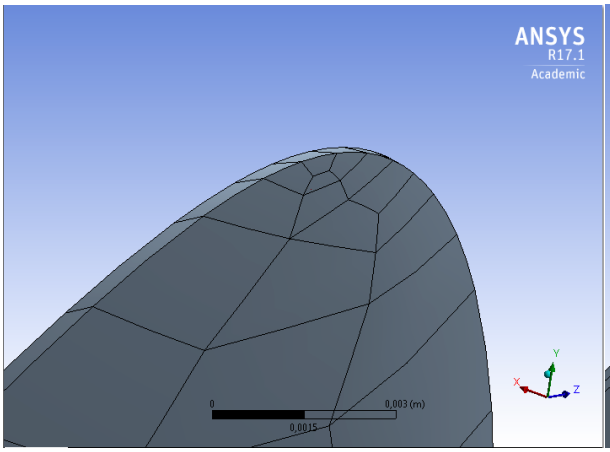

Figure 5.6: Tip elements Sweep mesh 2

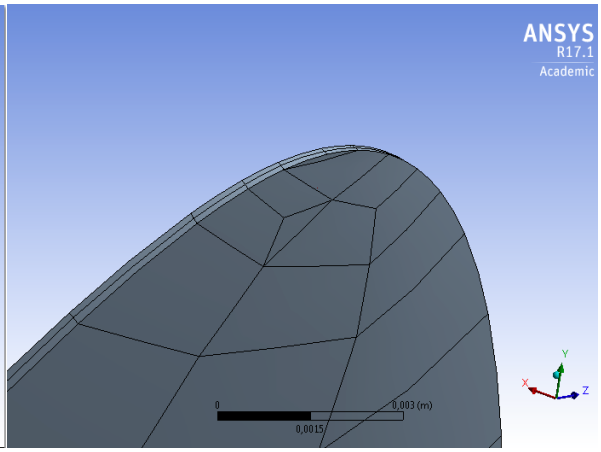

Figure 5.7: Tip elements Sweep mesh 3

5.2.2. Discussion FE Results

The chosen mesh of figure 5.8 is compared to the Greenprop FE model. The model of Greenprop is constructed using FE solver MARC. Both models use quadratic solid elements. Within solid elements, shape functions describe the variation of displacement in the element. These shape functions can be different for the two FE packages. The mesh distribution is another source for dissimilarities. The Greenprop model uses a mesh distribution of 29 (along chord) x 30 (in radial direction) x 4 (through thickness), thus 3480 elements, whereas the ANSYS model has 479 elements. The structural model of Greenprop is made identical to the fluid model, allowing for direct integration of the loads and deformations across the fluid- and structure interface. This leads to another mesh distribution of the FE model.

The deviation in eigenfrequency of the first mode is only 0.3 %. For the second mode this is 0.8% and for mode 3 to 5 the deviation has a maximum of 4%. These deviations are within 5% and it is therefore assumed that the same response is found for both FE models. The deviation from the physical model is 2.8 % and 0.5 % for mode one and two, respectively. However, when the uncertainty bandwidth of 295-352 Hz is taken into account, the eigenfrequency of the sweep 2 mesh falls within this bandwidth and can therefore be considered equal. It can be concluded that the differences in outcomes are small, the ANSYS model can be considered sufficiently accurate and the response is considered to be equal to the Greenprop FE model.

5.3. Simulations

The flexible (RANS-FEM) simulations are carried out by coupling the structure grid to the fluid grid of section 4.2. For these simulations a similar approach is used as in the FSI simulations of the benchmark case. Before the simulations are carried out, it is verified whether the interface nodes of the FEM model are correctly located in the fluid model. This check is performed to ensure that loads and deformations can be correctly transferred across the interface by the RBF interpolation method.

The test conditions of the simulations are equal to the Greenprop simulations with the rigid propeller of table 4.2. Parameters that are used in the analysis are thrust, torque, pressure and deformation. The numerical uncertainty analysis of Eça and Hoekstra [14] is performed for the flexible results. First the results are presented together with the results of the RANS simulations with the rigid propeller. This gives insight in the influence of the flexibility on the analysed parameters. The results are discussed and compared to the results of the BEM-FEM simulations and experiments.

5.3.1. Settings

The additional simulation settings for the RANS-FEM simulations compared to the RANS simulations are described in this subsection. With the flexible propeller unsteady simulations are performed. In the sensitivity analysis of the benchmark case it was concluded that the time step $\triangle t$ should be chosen carefully. However, for the flexible propeller, only the equilibrium displacement is requested. Therefore, the size of the time step can be large compared to the period of the initial motion of the structure. For the time discretisation the

three-time level method is used. The time step is chosen such that the grid rotates 30 degrees in every time step. The three test conditions have a rotational speed n_p of 901, 1001 and 1400 rpm for J = 0.369, 0.512 and 0.849, respectively. This leads to time steps of $\triangle t$ = 0.006,0.005 and 0.004 seconds, respectively.

Another conclusion that was drawn in the sensitivity analysis of the benchmark case concerned the RBF radius. For the RBF radius it should be checked whether the forces are transferred correctly across the interface. The RBF radius of the interface coupling is set to 0.1 m, with a convergence tolerance of 10^{-12}.

The AFM moving grid method is used for the rotation of the grid equal to the RANS simulations. For RANS-FEM simulations the fluid grid also deforms due to the deformation of the propeller blade. Therefore a deforming grid method should be applied. The RBF method is used for the deformation of the internal grid, with an RBF radius of 0.1 m. The convergence tolerance of the coupling is set to 10^{-5}.

The blending scheme for the convective flux discretisation of the momentum equation is used with a blending factor of 0.5 and the $k-\sqrt{k}L$ turbulence model, equal to the rigid Greenprop simulations. For the coupled mass-momentum problem a segregated type is used, similar to the benchmark case FSI simulations.

5.4. Results Numerical Uncertainty

The numerical uncertainty method of Eça and Hoekstra [14] is used for the determination of the numerical uncertainty. The method is used for the thrust, torque en tip displacement that are important parameters in this study. The grids that are used for this analysis are described in section 4.2 with the amount of cells of table 4.3.

The results of the numerical uncertainty analysis are shown in figures 5.9-5.11. In these figures, U represents the numerical uncertainty of the finest grid and p the order of accuracy. All numerical uncertainties derived in this study are also found in appendix C. The results for the different advance ratios are now discussed and compared to the numerical uncertainties found for the rigid propeller.

The numerical uncertainties of the rigid propeller for thrust were 0.7%, 0.1%, and 7.7% for J = 0.369, 0.512 and 0.849, respectively. For the flexible propeller, comparable results for thrust are found of 0.7%, 1.1% and 7.0%, shown in figure 5.9.

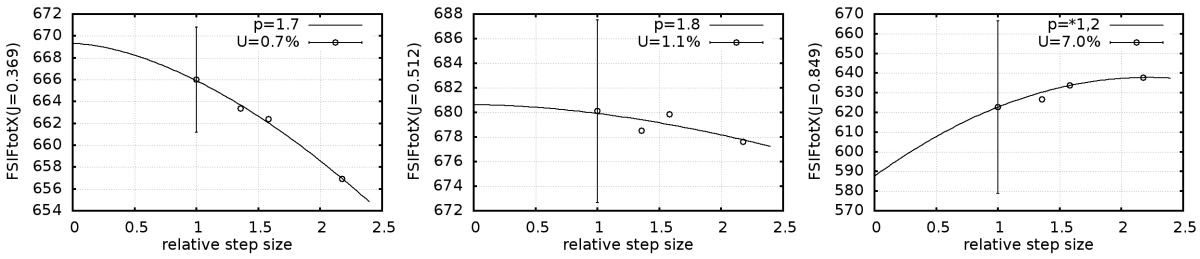

Figure 5.9: Discretisation error (Thrust) for J= 0.369, J= 0.512 and J= 0.849 - FSI simulations

For the torque, uncertainties of 2.2, 2.2 and 9.9 % are found for J = 0.369, 0.512 and 0.849, respectively. This is visible in figure 5.10. For the rigid propeller values of 1.0, 3.4 and 11.2 % were found. In the rigid propeller chapter it was mentioned that a numerical uncertainty up to 5% is acceptable for marine propeller applications [22]. The numerical uncertainties for advance ratios 0.369 and 0.512 are below 5% for both thrust and torque. For J=0.849 this is not the case, initially lower values were found, however due to an error late in the process higher values are found. For J=0.849 it is recommended to use a finer grid.

The tip displacement in x-direction is monitored by writing the location of the propeller blade tip to a file at every time step t. The location in x at the last time step is used for the uncertainty analysis of figure 5.11. Values of 5.4%, 5.4% and 3.9% are found for J = 0.369, 0.512 and 0.849. The numerical uncertainties found for thrust, torque and tip displacement should be kept in mind for further analysis.

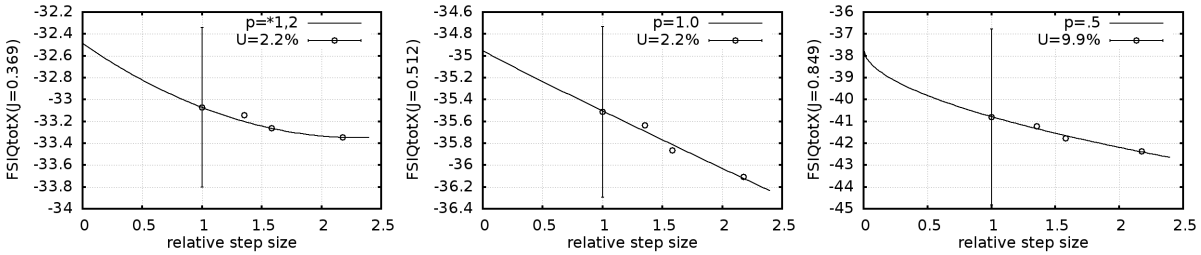

Figure 5.10: Discretisation error (Torque) for J= 0.369, J= 0.512 and J= 0.849 - FSI simulations

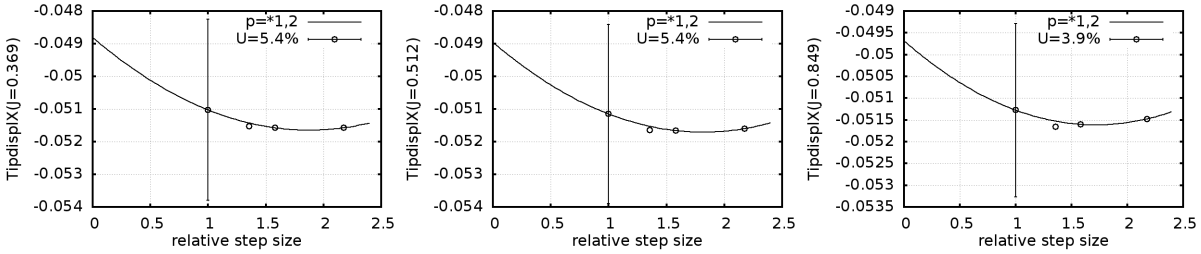

Figure 5.11: Discretisation error (Tip X Coordinate) for J= 0.369, J= 0.512 and J= 0.849 - FSI simulations

5.5. Thrust and Torque Results

The thrust K_T and torque K_Q results of the RANS-FEM simulations are compared to the rigid results, to analyse the influence of the flexibility. In tables 5.4 and 5.5, the results are shown together with the results of K_T and K_Q for the rigid propeller, found in section 4.6. The difference between the rigid and flexible thrust and torque is indicated with $\triangle K_T$ and $\triangle K_Q$ in these tables.

The numerical uncertainties obtained in sections 4.4 and 5.4 are indicated with U(RANS) and U(RANS-FEM). $\triangle K_T$ and $\triangle K_Q$ can be described as range, by taking into account the numerical uncertainties of both simulations. The bandwidths for $\triangle K_T$ and $\triangle K_Q$ are presented in the last columns and in figures 5.12 and 5.13. The results are discussed in the next section.

	K_T(RANS)	U(RANS)	K_T(RANS-FEM)	U(RANS-FEM)	$\triangle K_T$	Bandwidth
J = 0.369	0.220	0.7%	0.218	0.7%	-0.9%	+0.4% -2.3%
J = 0.512	0.183	0.1%	0.182	1.1%	-0.6%	+0.6% -1.8%
J = 0.849	0.089	7.7%	0.087	7.0%	-2.3%	+11.8% -15.6%

Table 5.4: K_T RANS-FEM compared to RANS, taking into account numerical uncertainty

	$10K_Q$(RANS)	U(RANS)	$10K_Q$(RANS-FEM)	U(RANS-FEM)	$\triangle K_Q$	Bandwidth
J = 0.369	0.333	1.0%	0.326	2.2%	-2.1%	+1.1% -5.2%
J = 0.512	0.289	3.4%	0.284	2.2%	-1.7%	+3.9% -7.0%
J = 0.849	0.177	11.2%	0.169	9.9%	-4.5%	+18.1% -22.6%

Table 5.5: K_Q of RANS-FEM compared to RANS, taking into account numerical uncertainty

5.6. Discussion Thrust and Torque Results

The mean deviations of the three advance ratios are -0.9%, -0.6%, -2.3% for $\triangle K_T$ and -2.1%, -1.7%, -4.5% for $\triangle K_Q$, for J=0.369, 0.512 and 0.849, respectively. These values are indicated with '$*$' in figures 5.12 and 5.13. The advance ratio of J=0.849 has a larger uncertainty for thrust and torque in both rigid and flexible simulations. This leads to a larger bandwidth around the result of $\triangle K_T$ and $\triangle K_Q$. For simplicity, the mean values are used in the following analysis, however, this bandwidth of J=0.849 should be kept in mind. The mean

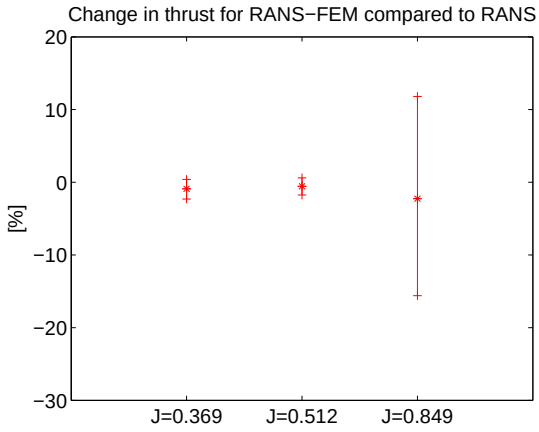

Figure 5.12: Influence of flexibility on the thrust ($\triangle K_T$)

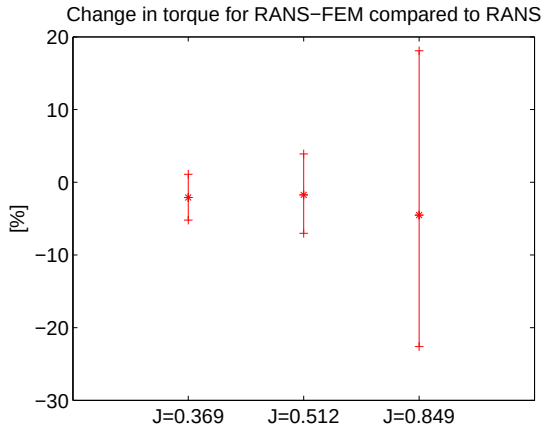

Figure 5.13: Influence of flexibility on the torque ($\triangle K_Q$)

values of $\triangle K_T$ and $\triangle K_Q$ are all negative. This means that the thrust and torque most probably decrease for RANS-FEM compared to RANS. The flexibility of the blades causes the thrust and torque to be lower. This is as expected, due to the blade adapting to the hydrodynamic loading. This was also seen in the benchmark case, where total pressure on the plate slightly decreased when it adapted to the flow.

The results of K_T and K_Q can be used to determine the open water efficiency, η_O, for RANS and RANS-FEM. For J=0.369, η_O is 38.8% for rigid and 39.3% for flexible. Advance ratio 0.512 also shows an increase in open water efficiency. η_O is 51.6% for rigid and 52.2% for flexible. For J=0.849 the largest difference is found of 67.9% and 69.6%. This means that the open water efficiency slightly increases for RANS-FEM compared to RANS of 0.5%, 0.6% and 1.7% for J=0.369, 0.512 and 0.849, respectively. It should be kept in mind that the numerical uncertainty is not taken here.

The influence of flexibility seems to have the most influence on the torque compared to the thrust. For instance for J=0.369, $\triangle K_T$ has a mean value of -0.9% where $\triangle K_Q$ has a mean value of -2.1%. This can be explained by the pressure distribution on the blade. For the determination of thrust the total pressure on the blade is integrated over the blade area. Where torque is more dependent on the location of the pressure peaks on the blade. If pressure changes are present at the outer radius, this will have more effect on the torque compared to a pressure changes at the root of the blade. To analyse whether the pressure distribution complies with this thrust and torque trend, the pressure distribution between rigid and flexible is analysed in section 5.7.

From tables 5.4 and 5.5, another phenomenon can be observed. The influence of flexibility of the propeller appears to be the largest for the higher advance ratios, i.e. for small angles of attack. The mean $\triangle K_T$ is -2.3% for J=0.849, where this is -0.9% for J=0.369. For $\triangle K_Q$ this is -4.5% compared to -2.1%. This can be explained by the geometry change due to its flexibility. For small angles of attack a slight change in pitch will have a larger effect on the flow around the blade. For large angles of attack this influence will be smaller as the flow around the blade will not drastically change.

A difference between RANS and RANS-FEM simulations is that an interpolation scheme is used to transfer the loads and deformation of the structure across the fluid-structure interface. RBF interpolation is used for this purposes which is explained in the simulations section 4.3. To check whether the interpolation of loads is correct when using this RBF interpolation, two checks can be performed. These checks are discussed in the next subsection. Then, comparison is made between BEM-FEM and experimental results, to check whether similar behaviour in loading on the blades is found.

5.6.1. RBF Interpolation

In the theory chapter, it was explained that when RBF interpolation is used it is important that the energy is conserved across the fluid-structure interface. In the FSI module of ReFRESCO the energy is monitored. At the end of every time step the total work, energy loss and change in energy are monitored. These are shown in figure 5.14. Here the unit of Work is expressed in Joule (J). The total amount of work across the interface reaches an equilibrium after approximately seven seconds, this is equal to the time at which equilibrium force and displacement are found for the flexible propeller. The change in energy becomes constant at the same time. The energy loss is around 0.0035 J, which is approximately 1.3 % of the total amount of work on the interface. From this energy check it can be concluded that the energy is correctly conserved across the fluid-structure interface.

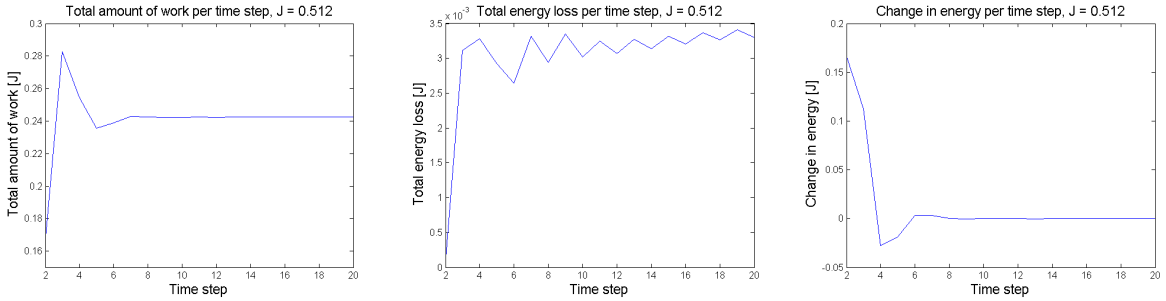

Figure 5.14: The total amount of work, energy loss and change of energy at the interface for J = 0.512

To verify the interpolation of the loads, two checks are performed. First, a rigid simulation is carried out with the deformed solution as grid. If the interpolation of the loads is correct, the same equilibrium pressure should be obtained from this rigid simulation compared to the FSI result. Secondly, the pressure obtained from the RANS simulation is applied to the FEM model. The reaction force at the root is compared to the total force of the RANS-FEM simulation.

For the RANS-FEM simulation of J=0.849 a total force of 633.67 N at one blade was found. For the rigid simulation with the deformed grid a force of 633.85 is found. This is a difference of 0.03 %. For the torque the difference is 0.02 %. For the advance ratio of J=0.512, even smaller differences of 0.0004 % and 0.001% for thrust and torque were found, respectively.

For the second verification, the pressure of the rigid RANS simulations is imported on the ANSYS model. It must be noted that by importing the pressure in ANSYS, the pressure is defined pointwise on the structure corner nodes or elements. Therefore here an interpolation to structural nodes is made as well. However, another interpolation compared to the RBF. The pressure from ReFRESCO and imported pressure on the elements and corner nodes are shown in figures 5.15 and 5.16 for the suction- and pressure side, respectively.

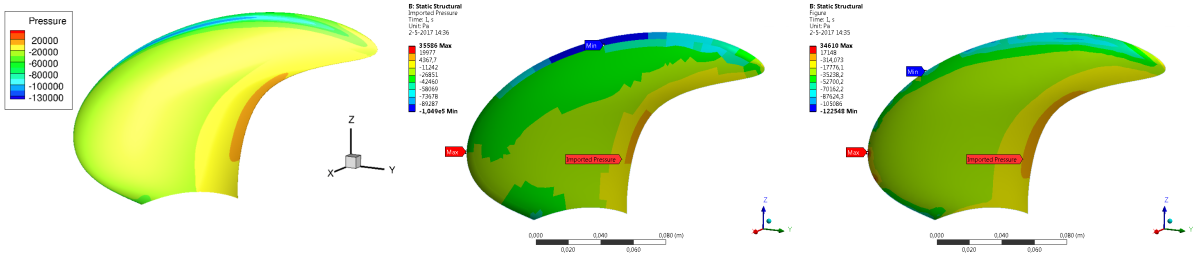

Pressure ReFRESCO Imported pressure on Elements Imported pressure on nodes

Figure 5.15: Imported pressure from ReFRESCO to ANSYS, suction side

From these checks on the RBF interpolation and the monitored energy loss, it can be concluded that the loads are interpolated correctly across the interface and that the error made by the RBF interpolation is negligible compared to the total work on the interface.

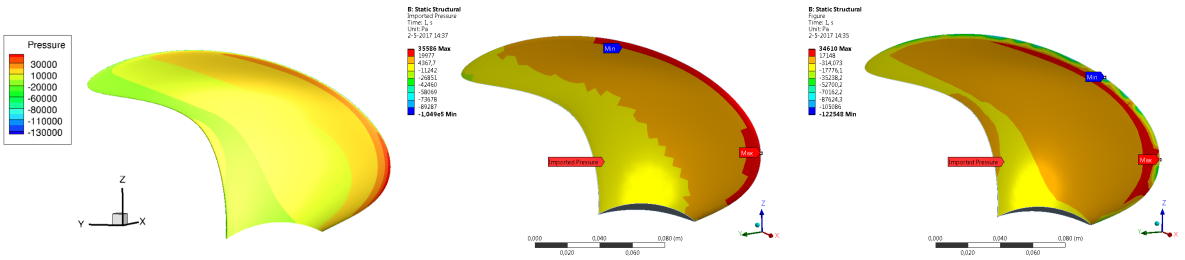

Pressure ReFRESCO Imported pressure on Elements Imported pressure on nodes

Figure 5.16: Imported pressure from ReFRESCO to ANSYS, pressure side

5.6.2. Comparison BEM-FEM

Before the flexible results of RANS-FEM are compared to BEM-FEM, a short recap of the results between the rigid simulations of RANS and BEM is given. The rigid results showed a difference in K_T of 12%, 12% and 21% for J=0.369, 0.512 and 0.849. For K_Q this was 3%, 7% and 16%. Therefore, it is expected that a deviation in the same range for RANS-FEM is found in comparison with BEM-FEM. The K_T and K_Q found for the RANS-FEM simulations are shown in table 5.6. It must be noted that here the bandwidth of numerical uncertainty for RANS-FEM is not shown, only the mean values of K_T and K_Q are shown in the table.

For the low advance ratios a deviation in K_T of approximately 10% is observed, for J=0.849 this is 18%. This is in the same range as the differences found between BEM and RANS in the rigid simulations. The highest deviation is observed for the advance ratio of J=0.849. This difference is probably due to the same causes as for the rigid simulations. The flow around the propeller and therefore the loading on the propeller is different between RANS and BEM. This was shown in the pressure distributions on the blades.

	K_T(BEM-FEM)	K_T(RANS-FEM)		$10K_Q$(BEM-FEM)	$10K_Q$(RANS-FEM)	
J = 0.369	0.244	0.218	-11%	0.326	0.326	0%
J = 0.512	0.203	0.183	-10%	0.292	0.284	-3%
J = 0.849	0.106	0.087	-18%	0.190	0.169	-11%

Table 5.6: K_T,K_Q RANS-FEM compared to BEM-FEM

In table 5.7, $\triangle K_T$ and $\triangle K_Q$ for BEM compared to BEM-FEM are shown. A reduction in thrust and torque is visible for BEM-FEM compared to the rigid results. For the thrust a reduction of -0.35% is visible for J=0.369 and J=0.512, for J=0.849 this is -4.8%. For the torque values of 2.4%, 1.4% and 5.1% are found for J=0.369, 0.512 and 0.849, respectively.

The $\triangle K_T$ and $\triangle K_Q$ results of BEM-FEM are compared to those of RANS-FEM. These percentages are plotted together in figures 5.17 and 5.18. The same trend can be distinguished. Namely, for high advance ratios the effect is larger. $\triangle K_T$ is -5% for J=0.849, compared to -0.4% for J=0.369. For the RANS-FEM results this was -2.3% compared to -0.9%.

Next to the effect on higher advance ratios, the torque shows more influence of flexibility compared to the thrust. This influence is best visible for the low advance ratios, $\triangle K_Q$=-2.35 % and $\triangle K_T$= -0.36%, for J=0.369. The same trend was visible in the RANS versus RANS-FEM results as discussed in section 5.6.

From the comparison of influence of flexibility on K_T and K_Q for RANS and BEM, it can be concluded that the same trend is found for the different advance ratios and thrust and torque. It should be mentioned that the numerical uncertainties are not taken into account in this comparison. Therefore, no firm conclusion can be drawn for the small deviations found in $\triangle K_T$ and $\triangle K_Q$ between RANS and BEM.

	$\triangle K_T$		$\triangle K_Q$	
	BEM vs BEM-FEM	RANS vs RANS-FEM	BEM vs BEM-FEM	RANS vs RANS-FEM
J = 0.369	-0.36%	-0.9%	-2.35%	-2.1%
J = 0.512	-0.34%	-0.6%	-1.37%	-1.7%
J = 0.849	-4.8%	-2.3%	-5.11%	-4.5%

Table 5.7: $\triangle K_T$ and $\triangle K_Q$ of flexible and rigid simulations

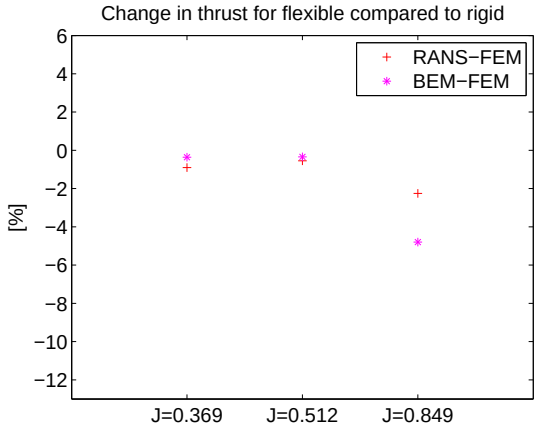

Figure 5.17: K_T influence flexibility

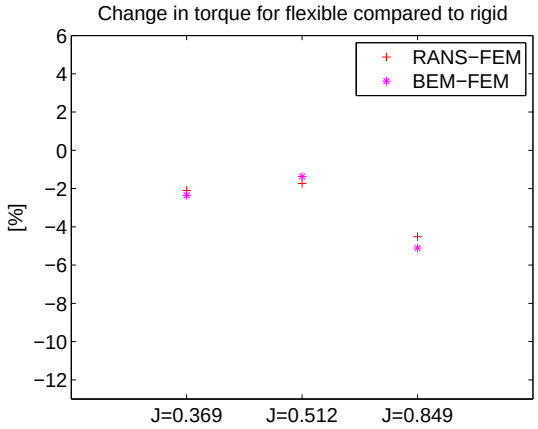

Figure 5.18: K_Q influence flexibility

5.6.3. Comparison Experiments

In the report of Maljaars [28], it was observed that $\triangle K_T$ and $\triangle K_Q$ did not show the same influence compared to BEM and BEM-FEM. This is probably due to the rigid tests in the CT. These were not carried out in the exact same conditions of the Greenprop tests, but were obtained from the open water tests in the CT. This made the comparison between thrust and torque for rigid and flexible not valid. Next to that, the K_T and K_Q results showed a lot of scatter. However, for the comparison of the deformation between RANS-FEM and experiments later on, it is interesting to know the measured total thrust. The total thrust will influence the deformation of the blade. The measured thrust in the experiments was 680, 687 and 726 N for J=0.369, 0.512 and 0.849 respectively. For RANS-FEM this is 666,680,623 N. Deviations of -2%, -1% and -16.5% are found for RANS-FEM compared to the experiments.

5.7. Pressure Results

Next to the influence of flexibility on the calculated thrust and torque, the pressure difference between the deformed and undeformed solution can be compared. For J = 0.369 this difference in C_{pn} is shown in figure 5.19. Here, the C_{pn} of the rigid result is subtracted from the flexible result. For the suction side a pressure increase is observed at the location of the leading edge vortex. At the pressure side a pressure decrease is found on outer radius and the leading edge. Similar distributions are noticed for J=0.512 and J=0.849 in figures 5.21 and 5.22. For J=0.369 the Cpn of flexible and rigid are plotted for three different radii in figure 5.20. The results are discussed in the next section.

5.8. Discussion Pressure Results

The $\triangle C_{pn}$ distributions of the previous section show that a lower overall pressure is found for the flexible blade. This lower pressure for the flexible blade is also noticed in the C_{pn} at radii r/R=0.8, 0.9 and 0.95 of figure 5.20. Here the red line represents the flexible and the blue line the rigid C_{pn}. The red line shows a lower pressure compared to the blue line. This phenomenon is attributed to the fact that the blade adapts to the hydrodynamic loading by deformation of the blade. This leads to a pressure decrease.

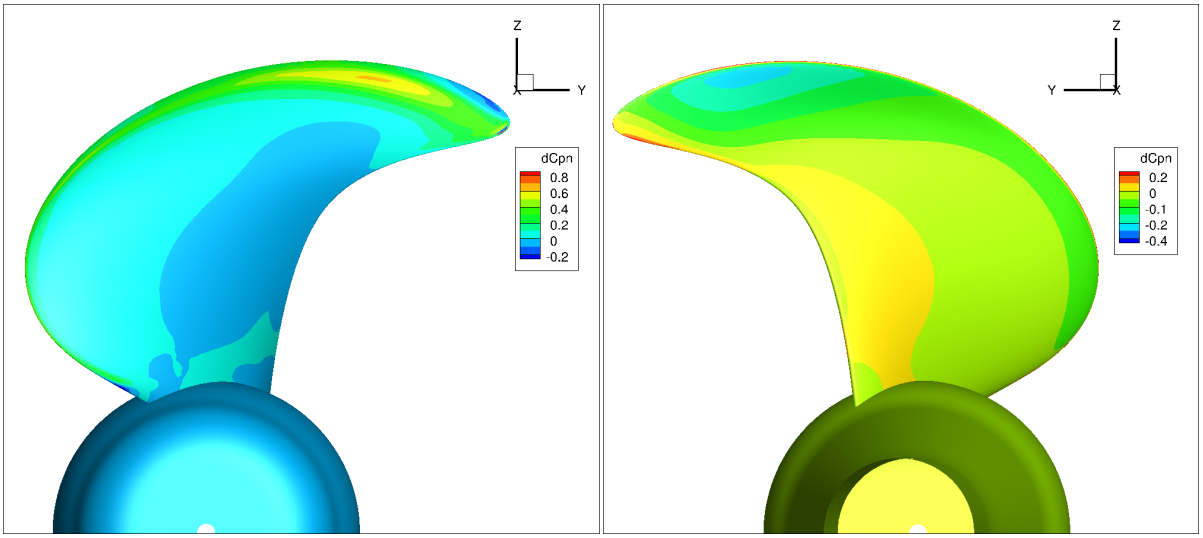

Figure 5.19: C_{pn} of rigid subtracted with C_{pn} of deformed, for J = 0.369, suction side (left) and pressure side (right)

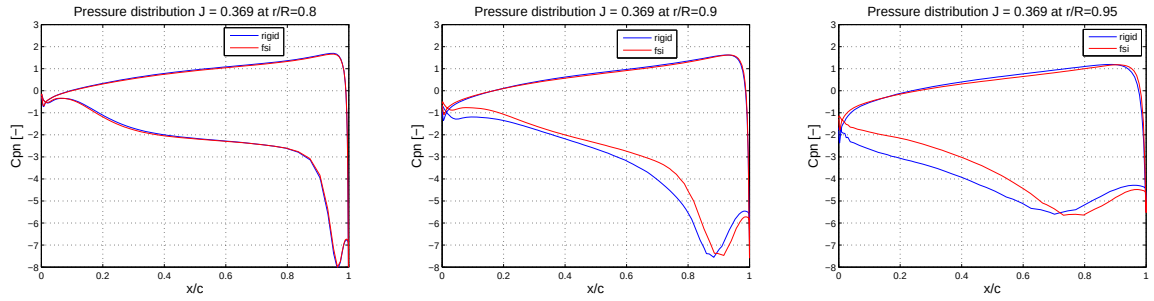

Figure 5.20: C_{pn} at r/R=0.8, 0.9 and 0.95 for J=0.369

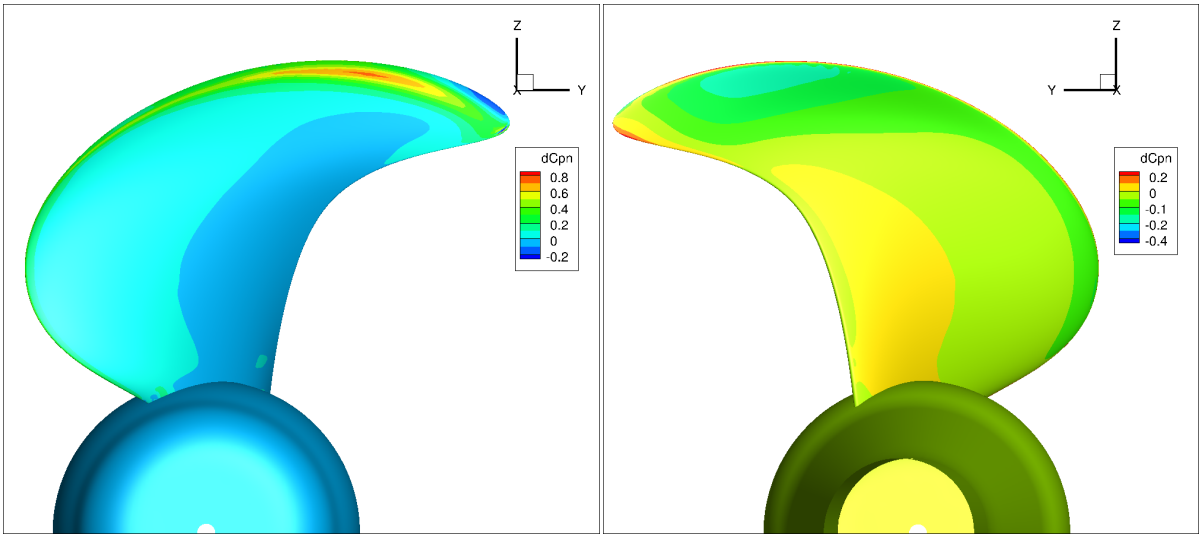

Figure 5.21: C_{pn} of rigid subtracted with C_{pn} of deformed, for J = 0.512, suction side (left) and pressure side (right)

The largest pressure change is found at the outer radii of the blade. This is because the most flexible part of the blade is located there, leading to the most deformation. The difference between flexible and rigid also declares the fact that the torque is mostly influenced by the flexibility of the blade. In section 5.6 it was discussed that a pressure peak located at the outer radius will have more effect on the torque compared to a pressure peak at the root of the blade.

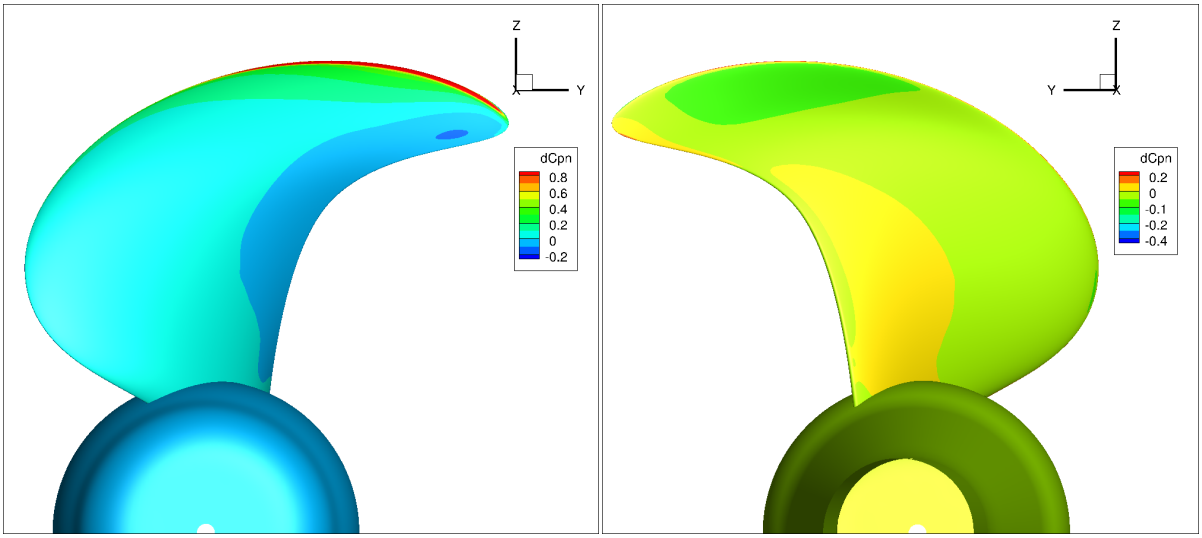

Figure 5.22: C_{pn} of rigid subtracted with C_{pn} of deformed, for J = 0.849, suction side (left) and pressure side (right)

5.9. Results Deformation

Due to the loading on the flexible propeller blades, the blades will deform. A uniform flow is applied that will lead to an equilibrium displacement after some time. To analyse the deformation, the undeformed and deformed geometries are compared. In figure 5.23 both grids are shown in one figure. The deformed geometry shows less pitch of the blade and the largest deformation is found at the tip. The deformation depends mostly on the loading of the blade,i.e. the thrust. The total thrust for the three test cases is T=666 N (J=0.369), T=680 N (J=0.512) and T=623 N (J=0.849). A difference of 6.5% is present when the thrust of J=0.849 is compared to J=0.369. It is expected that the bending difference is in the same order because a linear elastic approach is used.

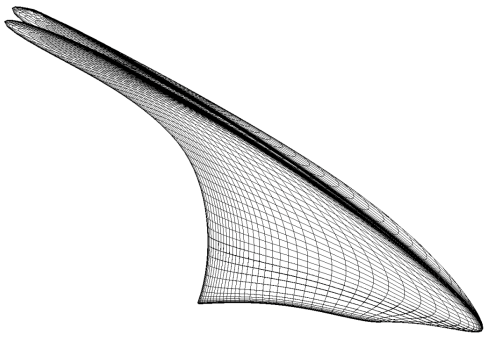

Figure 5.23: Undeformed and deformed grid

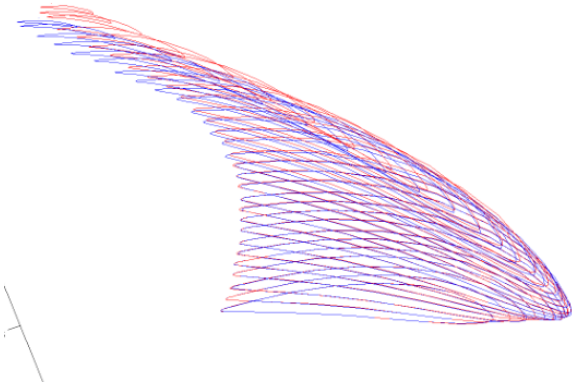

Figure 5.24: Deformed (red) and undeformed (blue) slices

Greenprop analysed the deformation of the blades found with BEM-FEM and experiments, by dividing the behaviour in pitching and bending. The blade is divided in radial slices of which the pitch angle is compared between rigid and flexible. For the bending deformation the difference in x-location of the midchord point is compared between rigid and flexible. To be able to compare to the Greenprop results, the bending and pitch behaviour are analysed for the RANS-FEM results as well. The deformed and undeformed geometries are converted to PPG files, using the MARIN propeller plug-in of Rhino. Deformed and undeformed radial slices as in figure 5.24 are found.

Due to the deformation of the propeller the geometry of the blade changes. This leads to a different radius, which makes it difficult to compare the two geometries of the deformed and undeformed propeller in

Rhino. In Rhino the diameter of the undeformed geometry is 0.34 m, the deformed geometry has a diameter of 0.344 m. This difference in diameter leads to another radial distribution of the slices. The slices are defined on different height, this makes it impossible to compare the deformed and undeformed geometries. Two assumptions can be made that are checked and used throughout the analysis, namely, the displacement of the root of the blade is zero and the displacement of the tip is used as check by comparing the most upper radii of both geometries. This deformation should be independent of different post-processing methods and is therefore used as validation. For undeformed and deformed the x positions of the midchord points are shown in figure 5.25, when the deformed midchord points are subtracted from the undeformed midchord points the bending behaviour is captured.

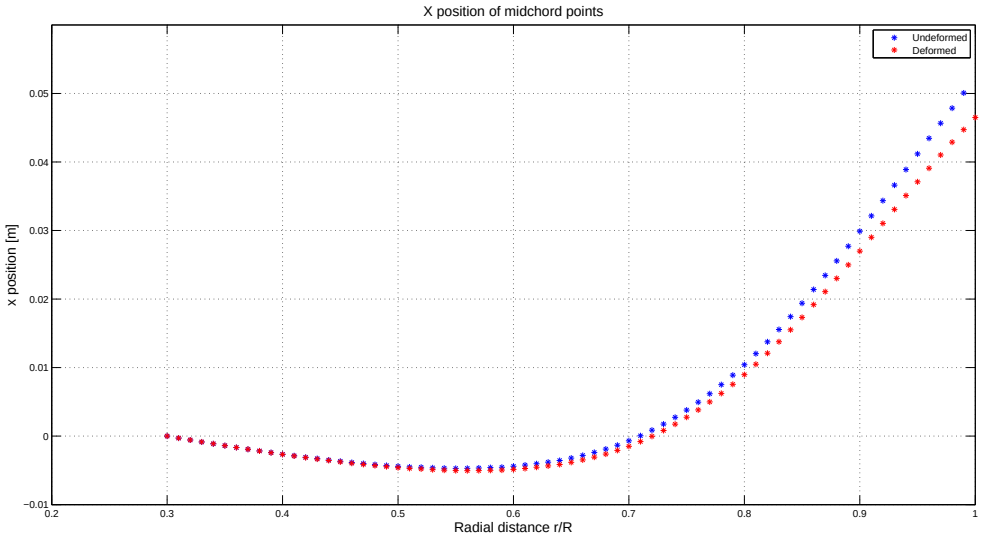

Figure 5.25: X displacement midchord points, J = 0.512 for deformed and undeformed

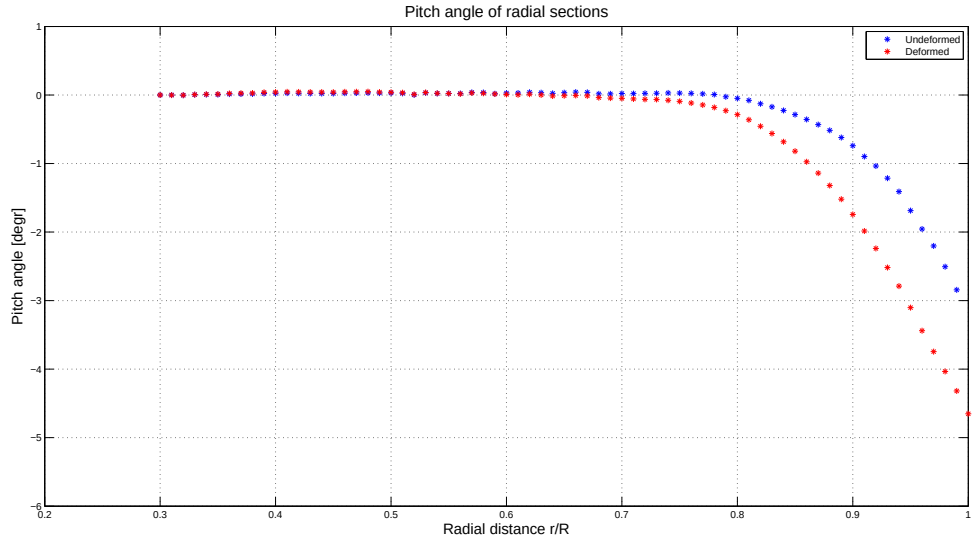

Figure 5.26: Pitch radial slices, J = 0.512 for deformed and undeformed

During the post-processing of the deformation results, it became clear that the location on the blade at which the bending and pitch results are determined is very important. Therefore, to be able to compare to

the results of Greenprop, it is ensured that the same location of radii and midchord points is chosen. In the Greenprop results the chord at 38% from the leading edge is chosen as midchord. Next to that, the midchord points on the suction side of the blade with offset from the chord line are chosen. These points are shown in figure 5.27. These points also correspond to the radii at which the pitch is determined.

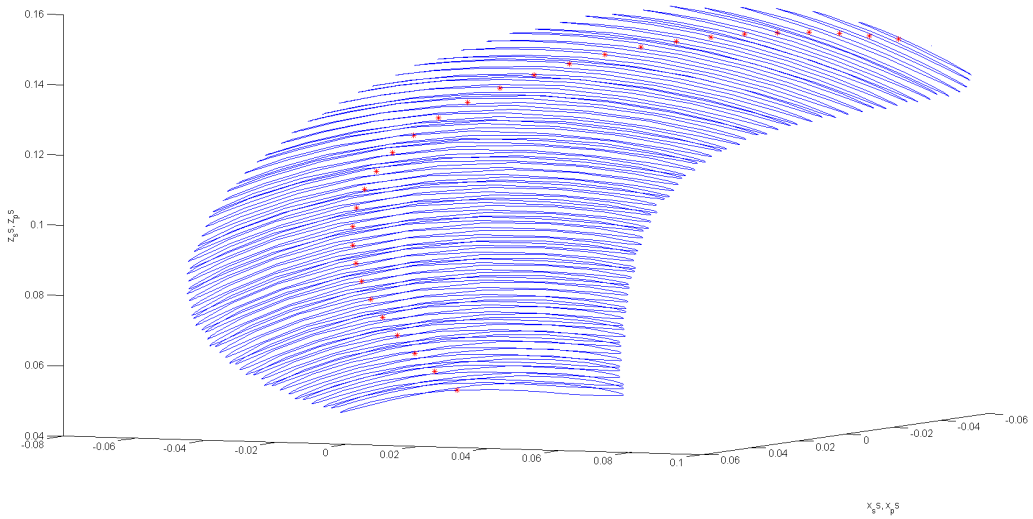

Figure 5.27: Chord points used for bending by Greenprop

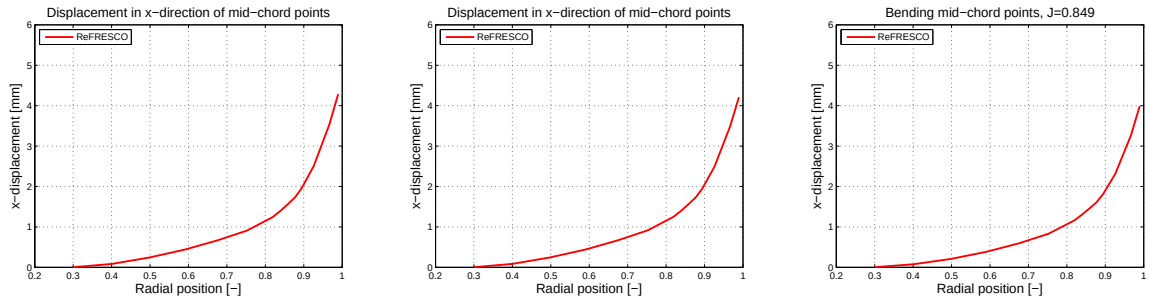

Figure 5.28: Bending deformation of deformed blade compared to rigid blade

To obtain results at the same location at Greenprop the coordinates are plotted in the fluid grid of the RANS simulations. The closest node of the fluid grid is searched for. The coordinates of this node are compared to the same node in the deformed fluid grid. By taking the change in x-direction, the bending behaviour is found. For pitch the same analysis is applied. However, two points are needed per radii to analyse the pitch angle and the change in pitch angle. In figure 5.26 the pitch angle of the different radii for undeformed and deformed are shown. When the undeformed pitch is subtracted from the deformed pitch, the distributions of figure 5.29 are found

5.10. Discussion Bend Deformation Results

From the bending of the three advance ratios in figure 5.28, it becomes clear that the bending behaviour is very similar. The low advance ratios 0.369 and 0.512 have a maximum (tip) displacement of 4.29 and 4.21 mm, respectively. The higher advance ratio, J=0.849, shows a tip displacement of 3.99 mm. However, before any conclusion can be drawn, the numerical uncertainties should be taken into account. In figure 5.31 the tip displacement is shown with corresponding bandwidth based on the numerical uncertainty of section 5.4.

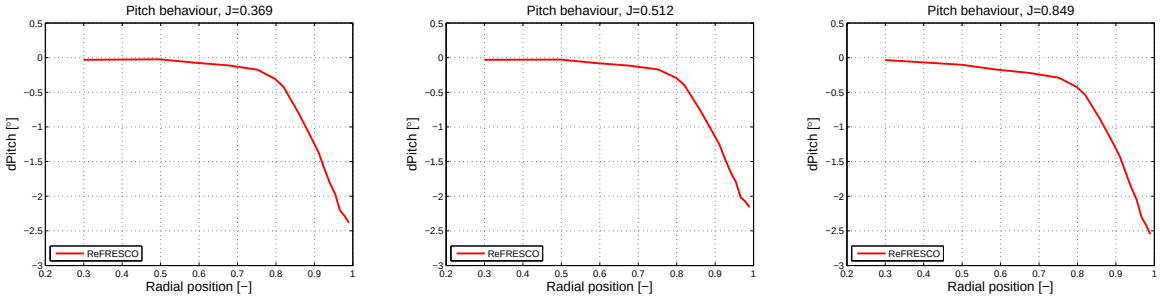

Figure 5.29: Pitch deformation of deformed blade compared to rigid blade, xyz LE,TE van GreenProp

The bending deformation is mostly governed by the thrust on the blade. Therefore this thrust with corresponding numerical uncertainty is shown in figure 5.30. The lower tip displacement of J=0.849 compared to the other advance ratios can be explained by the difference in thrust. If the mean thrust values of figure 5.30 are compared for J=0.369 and J=0.849, a difference of -6.5% is found for J=0.849. The bending of the tip is 7% lower for J=0.849. The lower thrust is probably the cause for this difference in tip displacement. Due to the large bandwidth of thrust for J=0.849, no firm conclusion can be drawn.

The thrust of advance ratio J=0.512 is higher compared to J=0.369, but the tip displacement is lower. This difference is approximately 2%, the uncertainty bandwidth overlaps with the bandwidth of J=0.369, therefore, no firm conclusion is drawn from these differences.

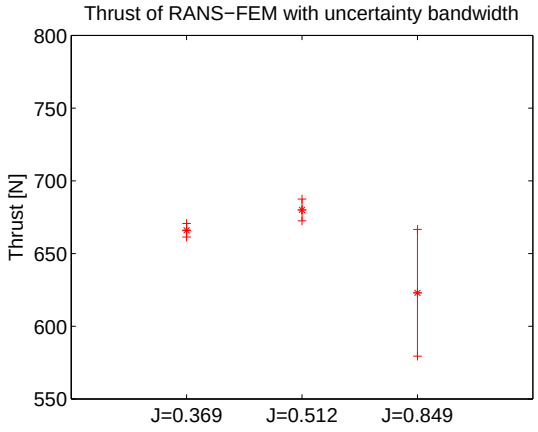

Figure 5.30: Total thrust with bandwidth

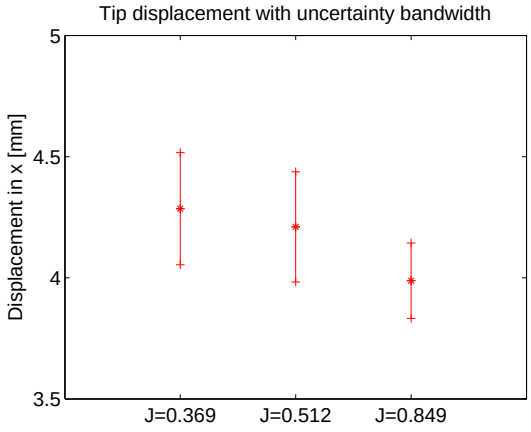

Figure 5.31: Tip displacement with bandwidth

5.10.1. Comparison Experiments and BEM-FEM

The total thrust of the simulations and experiments is shown in figure 5.32 including the numerical uncertainty bandwidth of the RANS-FEM simulations. First the thrust and bending or RANS-FEM are compared to the experiments, then the comparison with BEM-FEM is made.

The thrust of J =0.369 of RANS-FEM, is 666N with a numerical uncertainty of 0.7%. The measured thrust from the experiments is 679.9 N. This leads to a difference of -2% for RANS-FEM compared to experiments if only the mean thrust values are compared. If the numerical uncertainty bandwidth is taken into account the thrust of RANS-FEM is between -1.4% and -2.7% from the experiments. It is expected that approximately the same percentage is found for the difference in bending deformation. For J=0.512 no bending was measured during experimental tests. Therefore, it is not possible to compare the bending behaviour of J=0.512 to experimental results.

For J=0.849, a difference of 14% in the mean thrust values is observed, which is in line with the differences found in the rigid simulations. When the uncertainties are taken into account a bandwidth of -8.2% to -20.2% is found for RANS-FEM. Due to this lower thrust, it is expected that the bending deformation of RANS-FEM will be lower as well.

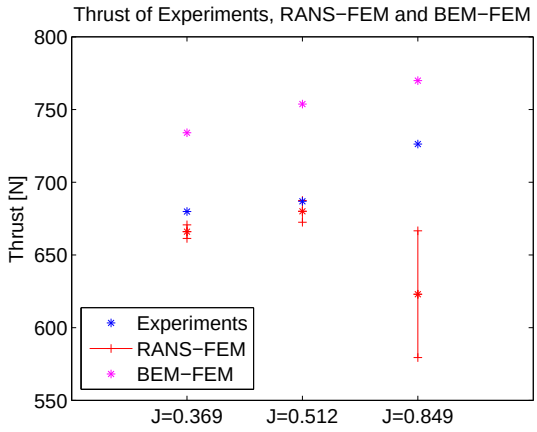

Figure 5.32: Total thrust of Experiments, RANS-FEM and BEM-FEM

The bending is plotted together with the measured results of the experiments in figures 5.33 and 5.34. For J=0.369 a good resemblance is found. The results of the RANS-FEM simulations show a lower tip displacement of -5.5 % compared to the experiments. For the rest of the blade a similar difference is found, this deviation along the radius is shown in figure 5.35. The numerical uncertainty of the tip displacement, found in section 5.4, was 5.4% for J=0.369. When this numerical uncertainty is taken into account a tip displacement in the range of -0.4% to -10.6% compared to experimental tip displacement is found. It can be concluded that this deviation in bending can be attributed to the lower thrust compared to the experiments that had a mean value of -2%.

For J=0.849, it was expected that the bending of RANS-FEM would be lower compared to the experiments due to the overall thrust being 14% lower for mean thrust values. However, from the results of figure 5.34, it follows that the bending of RANS-FEM for the last ten percent of the blade (r/R>0.90) is higher compared to the experiments. The deviation in percentage is shown in figure 5.36, for r/R between 0.6 and 0.9 a lower bending of -5% to -10% is found for RANS-FEM. After r/R=0.9 a higher bending of up to 7% is found. This is not as expected from the thrust. It is recommended to first obtain reliable results for the rigid high advance ratios before FSI simulations for these conditions are carried out.

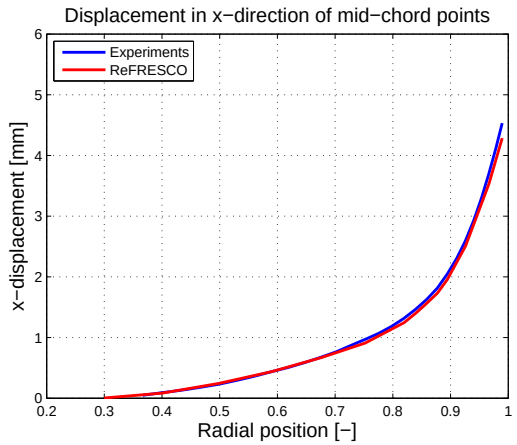

Figure 5.33: Bending results J=0.369

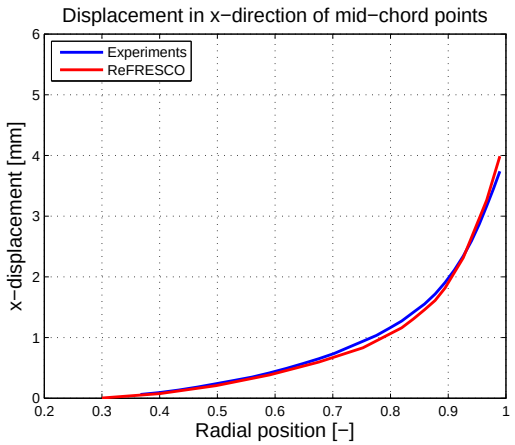

Figure 5.34: Bending results J=0.849

From the comparison of thrust and torque of RANS compared to BEM, it is expected that the deformation will be less due to the lower overall thrust predicted by RANS, shown in subsection 5.6.2. The results of BEM-FEM are plotted in figures 5.37, 5.38 and 5.39, together with the results of RANS-FEM and experiments. In these figures, the pink and green line represent the bending found with BEM-FEM for a pressure correction

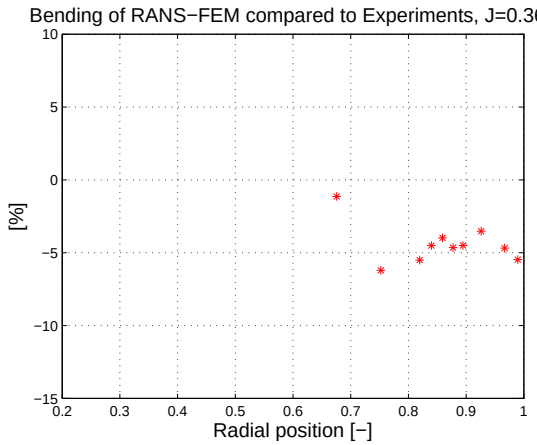

Figure 5.35: Bending of RANS-FEM compared to experiments, J=0.369

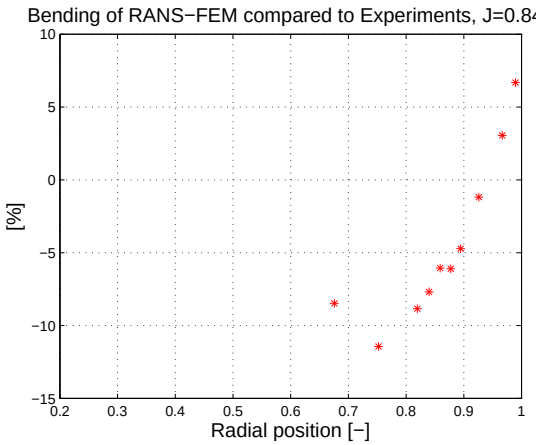

Figure 5.36: Bending of RANS-FEM compared to experiments, J=0.849

radius of r=0.90 and 0.95. This radius represents the fraction of the propeller radius at which the pressure is stretched to zero towards the tip. This explains why the bending of r=0.90 shows a lower bending deformation compared to the r=0.95 results, since for r=0.95 more pressure is left on the blade tip.

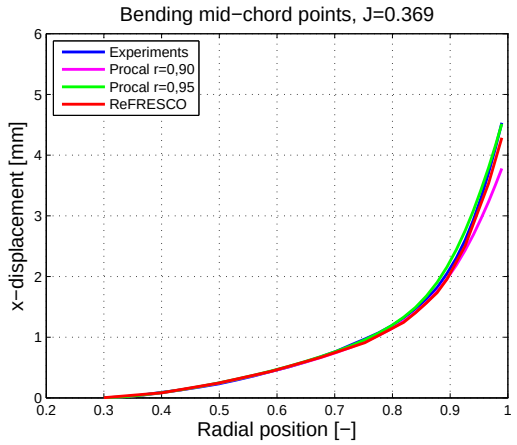

Figure 5.37: Bending J=0.369

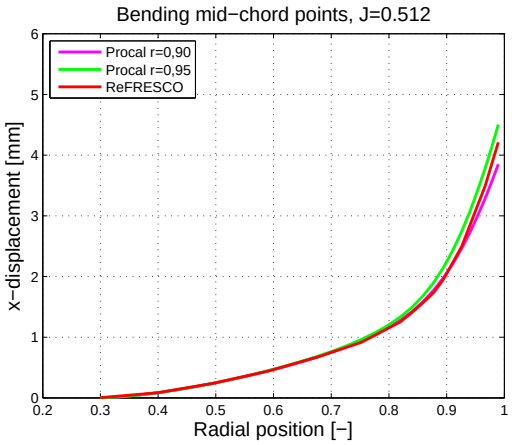

Figure 5.38: Bending J=0.512

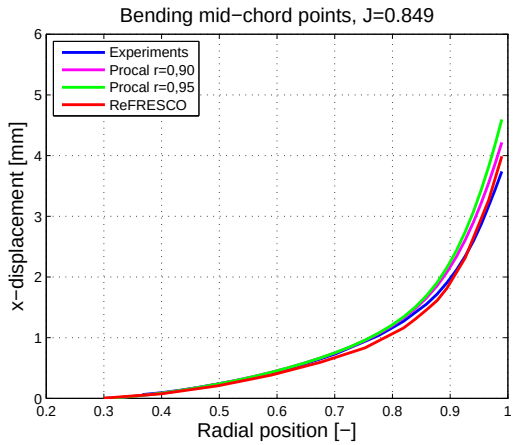

Figure 5.39: Bending J=0.849

From the thrust of BEM-FEM compared to RANS-FEM of figure 5.32, it becomes clear that RANS-FEM has a lower thrust of 9% compared to BEM-FEM for J=0.369. It is therefore expected that the bending behaviour of RANS-FEM will be around 9% lower as well. In figure 5.37 the results of Procal with a radius of 0.90 are lower than RANS-FEM and experimental results. This is due to the large area where the pressure is smoothed to zero. For r=0.95 a difference of 5% is found for the tip displacements. However, it was expected that the difference would be larger than 9% compared to RANS-FEM. For J=0.512 the same distribution is found. There, a lower tip displacement of 6.5% is observed for RANS-FEM compared to r=0.95, while the thrust is 10% lower for RANS-FEM. In the bending distribution of J=0.849, the tip displacements of the two BEM-FEM simulations are higher compared to RANS-FEM. This is as expected, because the thrust of BEM-FEM is 19% higher compared to RANS-FEM. The tip displacement of r=0.95 is 13% higher than RANS-FEM. Due to the higher thrust, a higher tip displacement was expected as well.

It can be concluded that the bending distribution of BEM-FEM with r=0.95 are higher compared to RANS-FEM. This is as expected because the thrust calculated with BEM-FEM is higher as well. Therefore, the setting of r=0.90 seems to be not suitable for this purpose, calculating a too low bending deformation compared to the thrust. It is recommended to analyse higher values for radius r to find bending that is in line with the thrust difference.

5.11. Discussion Pitch Deformation Results

The pitch deformations of J=0.369, J=0.512 and J=0.849 are shown in figure 5.29. A similar distribution for the three advance ratios is found. The flexible blade deforms under the hydrodynamic loading. The pitch decreases which is called de-pitching. The pitch deformation of the tip, i.e. r/R=0.99, is shown in figure 5.40. The bandwidth shown in this figure is determined using the numerical uncertainty of the tip displacement. For pitch two points on each radius are used for the determination of pitch. The numerical uncertainty is therefore multiplied by two. The mean values are -2.4°, -2.2° and -2.6° for J=0.369, 0.512 and 0.849, respectively.

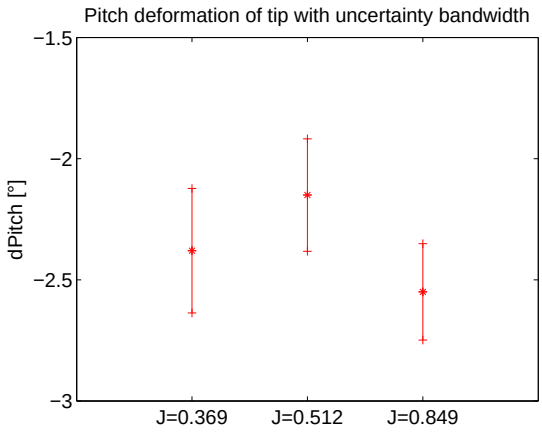

Figure 5.40: Pitch of the tip with uncertainty bandwidth

The high advance ratio shows more pitch deformation compared to the lower advance ratios. This can be explained by the lower suction peak present at the leading edge of the blade, which leads to pressure closer to the trailing edge and therefore a larger twisting moment compared to the lower advance ratios. In the next sections the pitching deformation is compared to experiments and BEM-FEM results.

5.11.1. Comparison Experiments and BEM-FEM

In figure 5.41 the results of RANS are plotted together with the experimental results for J=0.369 and J=0.849, the difference in percentage is shown in figure 5.42. For J=0.369 a lower pitch deformation is observed compared to the experiments. For the last 20 percent of the blade, i.e. r/R=0.8 to 1, the deviation is around 20%. For J=0.849 a higher pitch deformation is found in the range of 20-50% compared to the experiments. These differences are large compared to the uncertainty bandwidth and therefore too large to draw a conclusion. The difference in pitching behaviour between RANS and experiments are attributed to two causes. The first

is due to the post processing of the results. Two points are chosen either in experiments and RANS, different locations can lead to a different pitch distribution along the radius. In the experiments it was more difficult to post process the results of two points compared to the midchord point used for the determination of bending. Secondly, a modelling error of RANS for the flow at the last 10-20% of the blade can be present, due to the flow behaviour being too complex. The postprocessing and modelling error should be further investigated. Next to that, the pitch deformation of an advance ratio between 0.369 and 0.849 should be analysed.

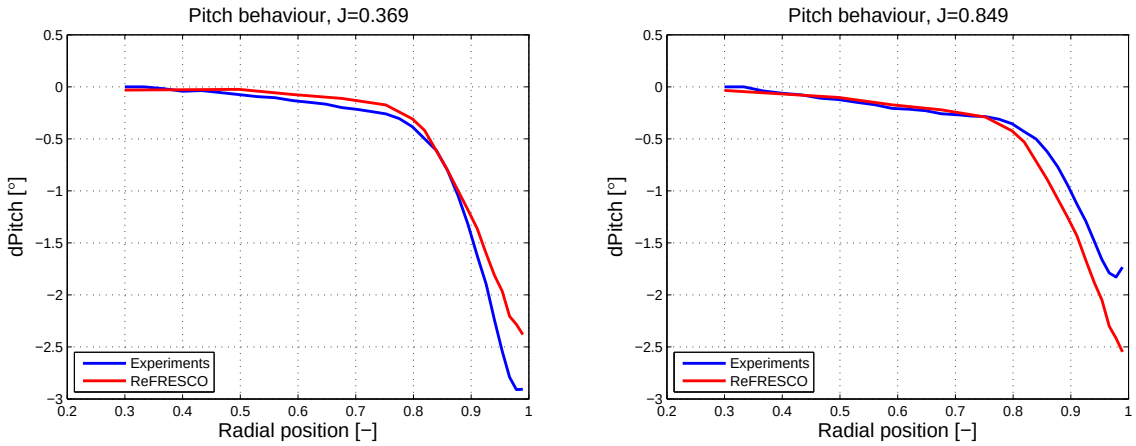

Figure 5.41: Pitch deformation results RANS compared to experiments for J=0.369(left) and J=0.849(right)

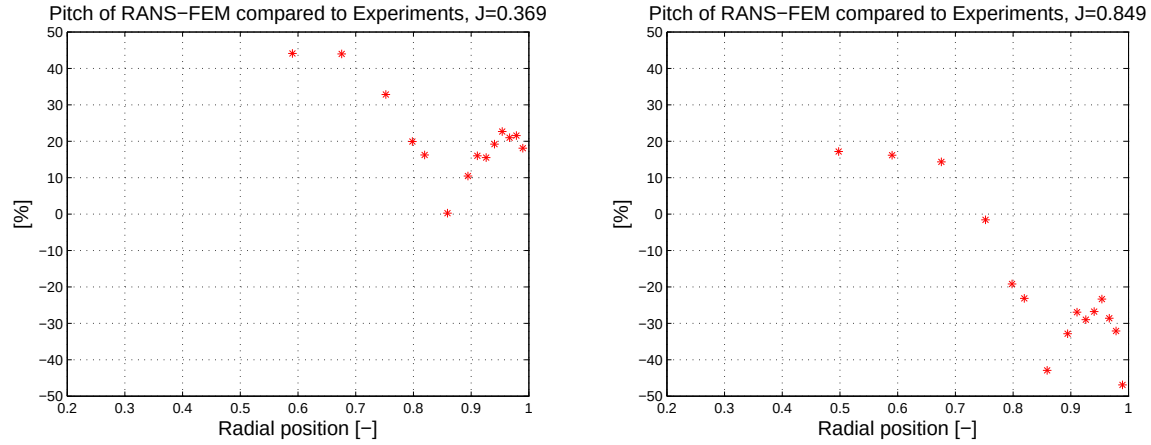

Figure 5.42: Pitch of RANS-FEM compared to experiments, J=0.849

In figure 5.43 the RANS-FEM results are plotted together with the BEM-FEM results. When the rigid pressure distributions of RANS are compared to BEM of section 4.8.2, it becomes clear that the pressure distribution of BEM is more deviated over the blade. For RANS concentrated peak pressures are found at the leading edge, this leads to a higher twisting moment of the blade. It is therefore expected that for RANS-FEM larger pitch deformations are found compared to BEM-FEM.

For J=0.369 the same distribution up to the last 5% of the blade is found compared to BEM-FEM with r=0.95. For J=0.512 the best is resemblance is found with r=0.95 as well. Here the tip pitch deformations are equal. For the pitch deformation the location of pressure- and suction peaks on the blade is important. A conclusion drawn by Maljaars (2016) [28] is that the hydro-elastic response of flexible propellers is very sensitive to small variations in pressure distribution at the tip region. This is visible in the results of BEM-FEM, where a change in radius of the pressure correction has a significant effect on the pitch deformation.

For J=0.849 the difference between r=0.90 and r=0.95 is smaller. This is due to the pressure at the tip

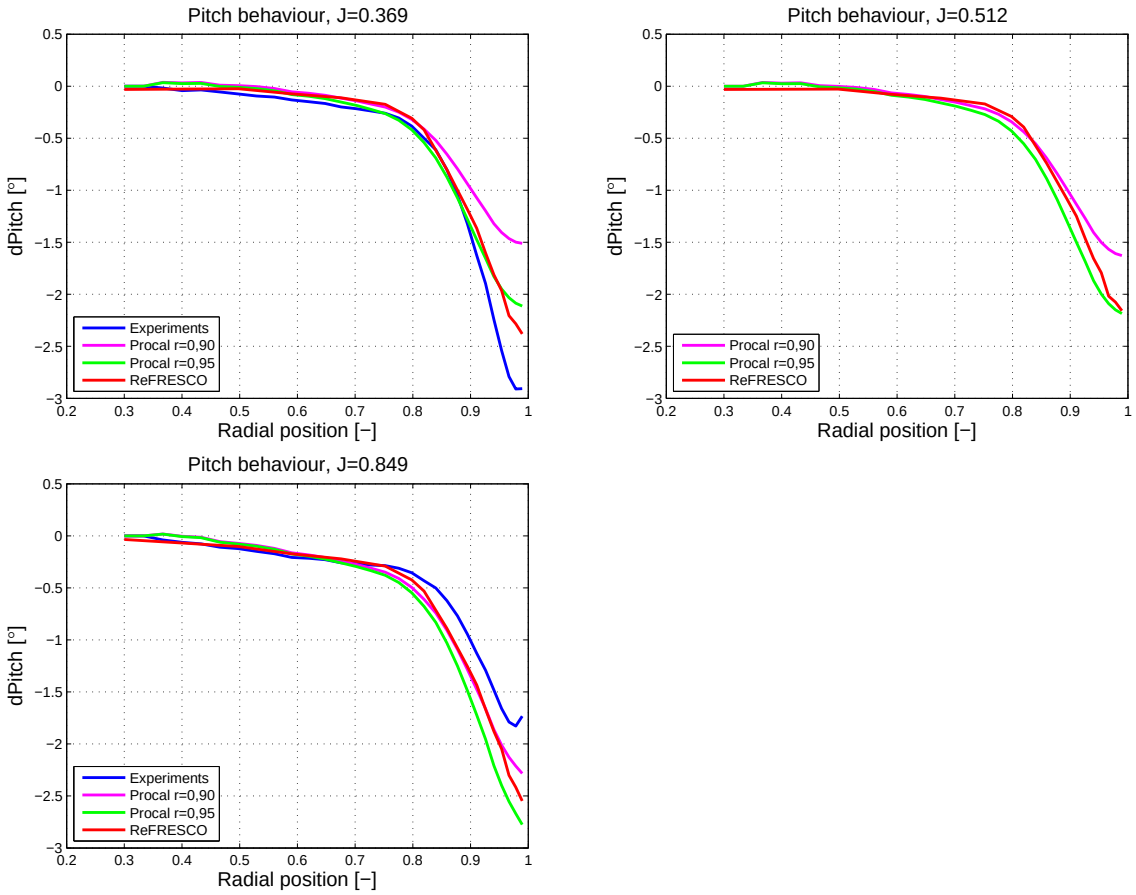

Figure 5.43: Pitch deformation for J=0.369, J=0,512 and J=0.849 compared to Procal (BEM) and measured results

for higher advance ratio. At the high advance ratio there is no clear leading edge vortex. The location from where the pressure is smoothed to zero to the tip has less influence compared to the low advance ratios. At J=0.849, RANS-FEM is closer to BEM-FEM with r=0.90. The distribution is equal up to the last 5% of the blade.

More settings for the radii in Procal can be considered to analyse the pitching behaviour. The exact pressure differences of RANS compared to BEM should be analysed to draw a firm conclusion on the deviation between the pitch deformations between RANS-FEM and BEM-FEM. A possible cause for different pitch deformation between RANS-FEM and BEM-FEM can be the arrangement of the tip elements of the FE models. The element distribution at the tip is different which can lead to a different response. The differences in pitch deformation are mostly found at the last 10% of the blade. Next to that, the postprocessing of the points at which the pitch is determined can be a cause for different distributions.

5.12. Summary and Conclusions

In this chapter, RANS-FEM simulations with the epoxy propeller are performed. For the RANS-FEM simulations, the conditions of the Greenprop tests are used, with advance ratios of 0.369, 0.512 and 0.849. A verification is performed on the RBF interpolation, to check whether the energy conservation at the fluid structure interface worked correctly. The RANS-FEM results are discussed and compared to the rigid simulations and to the Greenprop results. Conclusions drawn from the numerical uncertainty analysis, thrust, torque and deformation are outlined here.

1. The numerical uncertainty found for the RANS-FEM results showed a similar distribution as in the rigid propeller case. For advance ratios 0.369 and 0.512 uncertainties below 5% are found for thrust and torque, 0.7% to 2.2%. From Klaij et al.[22], it becomes clear that for marine propeller applications a numerical uncertainty of up to 5% is acceptable. Therefore, the grid is sufficiently accurate for advance ratios 0.369 and 0.512. For J=0.849 larger uncertainties were found, comparable to the rigid propeller study, of 7% for thrust and 9.0% for torque. In the conclusion of the rigid propeller study it was mentioned that it is recommended to use a finer grid for advance ratios larger than 0.8. However, because this error was identified late in the process the simulations are performed with this grid also for advance ratios larger than 0.8. The numerical uncertainty is also determined on the tip displacement, which is used for the deformation study, uncertainties between 3.9% and 5.4% were found, the grid is assumed to be sufficiently accurate for the deformation purpose.

2. The FEM model is constructed in ANSYS Workbench, by using a sweep mesh method and ensuring high element quality close to the leading-, trailing edge and tip. The eigenfrequencies are compared to the Greenprop FE model. The eigenfrequencies of the FE model deviate 0.3% and 0.8% from the GreenProp FE model for the first two modes. For the other three modes a maximum deviation of 4% was found. It was assumed that a deviation below 5% would suffice. Therefore, it is concluded that the FE models have a similar response.

3. The thrust and torque obtained with RANS-FEM are compared to the rigid RANS simulations. The difference in thrust and torque are described as $\triangle K_T$ and $\triangle K_Q$. The numerical uncertainties of RANS and RANS-FEM lead to bandwidths with mean $\triangle K_T$ values of -0.9%,-0.6%,-2.3% and mean $\triangle K_Q$ values of -2.1%,-1.7%,-4.5%, for advance ratios 0.369, 0.512 and 0.849, respectively. This means that it is most probable that a decrease in thrust and torque is obtained for the flexible RANS-FEM compared to rigid RANS simulations. This is explained by the blade adapting to the hydrodynamic loading. If the open water efficiency η_O is determined with the K_T and K_Q obtained from the RANS-FEM results an increase in η_O of 0.5%, 0.6% and 1.7% compared to rigid is found for J=0.369, 0.512 and 0.849, respectively.

   The first trend that is noticed in the mean values of $\triangle K_T$ and $\triangle K_Q$ is that the flexibility has the most influence on torque compared to thrust. This can be explained by the pressure distribution on the blade. The pressure difference between rigid and flexible $\triangle C_{pn}$ showed that the largest pressure changes are found at the outer radius of the blade, this has more effect on torque than a pressure change at the root of the blade.

   Another trend that is visible in the $\triangle K_T$ and $\triangle K_Q$ results, is the higher influence of flexibility on large advance ratios. This is explained by the fact that large advance ratios correspond to small angles of attack. A slight change in pitch will have more effect on the loading of the blade. For large angles of attack a geometry change will not drastically change the flow around the blade. If the results of thrust and torque are compared to BEM-FEM it becomes clear that thrust and torque of RANS-FEM are 0-17% lower compared to BEM-FEM. Both trends in $\triangle K_T$ and $\triangle K_Q$ are also visible for BEM-FEM compared to BEM. However, before any firm conclusion can be drawn, it must be noted that the mean values are used for comparison, the uncertainty bandwidth should be kept in mind.

   The comparison with experiments was not possible, the results showed too much scatter to draw a conclusion. This is attributed to the conditions of the experiments with the bronze propeller not being equal to the conditions of the flexible propeller experiments. Next to that, the results of flexible thrust and torque obtained from the experiments contained a lot of scatter.

4. It is expected that the bending is mostly influenced by the total thrust on the blade. The bend deformations of the tip obtained with RANS-FEM are 4.29, 4.21 and 3.99 mm, for J=0.369, 0.512 and 0.849 respectively. These differences are attributed to the in total thrust on the blade that has the same deviation.

   Compared to the experimental results, it can be concluded that for low advance ratios a good resemblance is found. The bending up to r/R=0.7 is identical. If the numerical uncertainty of the tip displacement is taken into account a lower bending than the experiments is found in the range of -0.4% to -10.6%. This is attributed to the lower thrust found in RANS-FEM with a mean value of -2%. For high advance ratios, where lower thrust and torque up to -20% are found for RANS-FEM, higher bending deformation is found which was not expected. It is recommended to further investigate the response at higher advance ratios before a conclusion can be drawn on the bending results.

   For the comparison with BEM-FEM, results with r=0.90 and 0.95 are used. These values represent the fraction of the radius at which the pressure is smoothed to zero towards the tip. The comparison shows better resemblance with the r=0.95 setting compared to r=0.90. It is concluded that r=0.90 is not suitable for this purpose, the pressure is too low due to the large area of pressure smoothed to zero. For r=0.95 a higher bending deformation is found than RANS-FEM of 5%, 6.5% and 13%, for J=0.369, 0.512 and 0.849, respectively. The total thrust calculated with BEM-FEM is 9%, 10% and 19% higher than RANS-FEM, it is expected that higher bending deformation would be observed. It is recommended to analyse higher values for radius r than 0.95 to find bending that is in line with the thrust difference.

5. The pitch deformation of the tip for J=0.369, 0.512 and 0.849 are -2.4°, -2.2° and -2.6°. The higher pitch of J=0.849 is explained by the lower suction peak present at the leading edge, which moves pressure closer to the trailing edge and therefore causes a larger twisting moment on the blade. For the comparison with the experiments it can be concluded that the RANS-FEM results do not have the same pitch distribution as the experiments. Even with the uncertainty bandwidth taken into account, the differences are too large. These deviations are attributed to the post processing and to a possible modelling error of RANS at the last 10-20% of the blade. This should be further analysed. Next to that, the pitch deformation of an advance ratio between 0.369 and 0.849 should be analysed.

   For the comparison with BEM-FEM it was expected that the pitch of RANS-FEM would be larger due to the more concentrated pressure distribution of RANS compared to BEM that causes a larger twisting moment. For J=0.369 and J=0.512 the best resemblance is found for BEM-FEM with r=0.95. At J=0.849, RANS-FEM is closer to BEM-FEM with r=0.90. More settings for the radii in Procal can be considered to analyse the pitching behaviour. The exact pressure differences of RANS compared to BEM should be investigated to draw a firm conclusion on the deviation. However, the exact pressure distribution between RANS and BEM should be analysed before a firm conclusion can be drawn from the pitch deviations. Next to that, the influence of the arrangement of the tip elements of both FE models on the response should be analysed.

From this flexible propeller study it can be concluded that more insight is gained in the response of the epoxy propeller in uniform flow obtained with RANS-FEM. The results are compared with BEM-FEM and experiments for thrust, torque and deformation. Next to that, knowledge is gained in the numerical uncertainties of FSI simulations with this propeller. During this study the FSI module is updated several times, which improved the module for the purpose of flexible propellers.

6

Conclusions

In this chapter the conclusions drawn in this study are summarised. The study presented in this report is part of the Greenprop project, which has the aim to calculate the hydro elastic response of flexible propellers by developing a coupling between a Boundary Element Method (BEM) and Finite Element Method (FEM), i.e. BEM-FEM simulations. In these BEM-FEM simulations a pressure correction is applied for the tip vortex, a viscous effect that is not captured by BEM. The settings of this correction showed a large influence on the hydro elastic response of the propeller blades. The study presented in this report is aimed towards the validation of BEM-FEM with Reynolds Averaged Navier Stokes (RANS) coupled to FEM. By using RANS, viscous effects are taken into account. Within the scope of this study simulations are performed with the epoxy propeller of Greenprop in a uniform wakefield, using RANS solver ReFRESCO and FE package ANSYS.

The objectives of this study are, to test the performance of the FSI module in ReFRESCO, to validate the results of the open water diagram of the rigid propeller in RANS, to verify the response of the propeller FE model and to analyse the response of the epoxy Greenprop propeller using RANS-FEM. The study is divided in three parts, the benchmark case, the rigid propeller case and the flexible propeller case. For a full description of the conclusions one is referred to the different chapters of the benchmark case (chapter 3), rigid propeller case (chapter 4) and flexible propeller case (chapter 5).

Benchmark Case

The reason for this benchmark case was to get familiar with RANS solver ReFRESCO and to check the reliability of the FSI module in ReFRESCO. The benchmark case is carried out on a 2D flexible thin plate clamped perpendicular to the bottom. With a uniform air flow applied that is parallel to the bottom plate. Simulations are carried out with the rigid plate and flexible plate, either by performing RANS or RANS-FEM simulations.

The fluid grid is constructed using the program HEXPRESS. For the structure grid linear solid elements are used. Grid studies are performed on the fluid and structural grid. The results of the rigid RANS simulations and flexible RANS-FEM simulations correspond to the results found in literature. The same equilibrium deflection of 0.024 m and a response frequency of 2.73 Hz are found. Therefore the FSI module of ReFRESCO can be considered accurate for this case. A sensitivity analysis was conducted on added Rayleigh damping, the size of the time step $\triangle t$ and the RBF radius. It was concluded that the influence of Rayleigh damping should be further analysed, next to the inaccuracies in the pressure signal that occur for very small $\triangle t$.

With the benchmark case, the FSI module of ReFRESCO is tested thoroughly, several updates were performed that have improved the FSI module. More insight is gained in both RANS and FSI in ReFRESCO. Next to that, the problems still present in the module are identified. The benchmark case has led to the conclusion that it can be reliably used in the propeller study.

Rigid Propeller

The rigid propeller study is carried out to verify the required fluid grid density and for comparison with rigid results of Greenprop. Next to that, it is interesting to compare the rigid propeller results to the flexible propeller results for analysis of the influence of flexibility. The open water diagram is constructed and simulations with conditions of the Greenprop tests are performed. The Greenprop tests have advance ratios J=0.369, 0.512 and 0.849.

The numerical uncertainties found for thrust and torque are below 5% for advance ratios below 0.8. For these conditions the grid is sufficiently accurate. For advance ratios larger than 0.8 the numerical uncertainties are larger than 5%. From these results it is recommended to use a finer grid for advance ratios larger than 0.8. The results of the RANS simulations and the measured open water diagram in the Deep Water (DT) tank show for an advance ratio above 0.2 larger differences in K_T than expected from the numerical and experimental uncertainties. These lower results for K_T and K_Q can have several causes. The effect of blockage of the fluid domain, modelling- and experimental errors are discussed. The most likely reasons are blockage and the turbulence model in ReFRESCO. This should be further analysed. The comparison of RANS with BEM results showed that for advance ratios up to J = 0.8, RANS better predicts the load on the blade compared to BEM. This is attributed to the flow separation at large angles of attack.

From the simulations performed in this chapter, knowledge is gained in propeller simulations with RANS. The accuracy of the RANS results is determined by evaluating the numerical uncertainty and comparing to experimental results. Next to that, a comparison is made between the results of BEM, which led to insight in differences and the reasons for these differences. The numerical uncertainties and performance parameters found for the rigid propeller are used in the flexible propeller study.

Flexible Propeller

In the flexible propeller study, RANS-FEM simulations are performed with the epoxy propeller of Greenprop. The FEM model is constructed in ANSYS Workbench, by ensuring high element quality close to the leading-, trailing edge and tip. The eigenfrequencies of the FE model deviate 0.3% and 0.8% from the Greenprop FE model for the first two modes. For the other three modes a maximum deviation of 4% was found. It was assumed that a deviation below 5% would suffice. Therefore, it is concluded that the FE models have a similar response. For the RANS-FEM simulations, the conditions of the Greenprop tests are used of J=0.369, 0.512 and 0.849. The numerical uncertainty analysis showed similar results as found in the rigid propeller study.

The thrust and torque obtained with RANS-FEM are compared to the rigid RANS results. A decrease in thrust and torque is obtained for the flexible RANS-FEM compared to rigid RANS simulations. This is attributed to the blade adapting to the hydrodynamic loading. The open water efficiency of the flexible propeller increases 0.5%, 0.6% and 1.7% compared to the open water efficiency of the rigid propeller. The first trend that is noticed in the thrust and torque is that the flexibility has the most influence on torque compared to thrust. This can be explained by the largest pressure changes at the outer radius of the blade, this has more effect on torque than a pressure change at the root of the blade. Another trend that is visible is the higher influence of flexibility the large advance ratio (J=0.849) i.e. small angle of attack. A change in pitch will have more effect on the flow around the blade and therefore on the loading of the blade. For large angles of attack a geometry change will not drastically change the flow around the blade. Both trends are also visible for BEM-FEM compared to BEM. It should be kept in mind that for this analysis the mean values of the uncertainty bandwidth are used. This bandwidth should be kept in mind before any firm conclusions are drawn. The comparison with experiments was not possible, the results showed too much scatter to draw a conclusion. Accuracy of the measured thrust and torque should be analysed.

The deformation of the blade is divided in bend and pitch deformation. It is expected that the bending deformation is mostly influenced by the total thrust on the blade. The differences in bend deformations of the tip, correspond to the differences in thrust. Compared to the experimental results, it can be concluded that for low advance ratios a good resemblance is found. For the high advance ratio, where lower thrust and torque were found for RANS-FEM, a higher bending deformation is found which was not expected. For RANS-FEM, it is recommended to further investigate the response at higher advance ratios before a conclusion can be drawn. For the comparison with BEM-FEM, two different radii are used which represent the fraction of the radius at which the pressure is smoothed to zero towards the tip. It was expected that higher bending defor-

mation would be observed for BEM-FEM due to higher thrust. It is recommended to analyse higher values for radius r to find bending that is in line with the thrust difference.

The pitch deformation showed higher pitch deformation for J=0.849 than J=0.369 and 0.512. This is explained by the lower suction peak present at the leading edge, which moves pressure closer to the trailing edge and causes a larger twisting moment on the blade. The RANS-FEM results do not have the same pitch distribution as the experiments. These deviations are attributed to the post processing and to a possible modelling error of RANS at the last 10-20% of the blade, which should be further investigated. Only J=0.369 and J=0.849 are analysed, an advance ratio between 0.369 and 0.849 should be analysed.

For the comparison with BEM-FEM it was expected that the pitch of RANS-FEM would be larger due to the more concentrated pressure distribution of RANS that causes a larger twisting moment. The exact pressure distribution between RANS and BEM should be analysed before a firm conclusion can be drawn from the pitch deviations. More settings for the radii in Procal can be considered. Next to that, the influence of the arrangement of the tip elements of both FE models on the response should be analysed.

From the flexible propeller study it can be concluded that more insight is gained in the response of the epoxy propeller in uniform flow obtained with RANS-FEM. The results are compared with BEM-FEM and experiments for thrust, torque and deformation. Next to that, knowledge is gained in the numerical uncertainties of FSI simulations with this propeller. Several recommendations for future work are outlined in the next section.

7

Recommendations

During this study several recommendations for future work were addressed that are outlined in this chapter. First, the recommendations from the benchmark case are presented. Then, the recommendations addressed in the rigid and flexible propeller studies are outlined.

From the benchmark case it became clear that the added Rayleigh damping worked, however the exact amount of damping seemed incorrect. The influence of this damping should be further analysed. Next to that instabilities in the pressure signal occurred for very small $\triangle t$. The cause for these instabilities should be further investigated.

The rigid propeller study showed that the numerical uncertainty for advance ratios larger than 0.8 were too high. It is recommended to use a finer grid for these advance ratios. Next to that, the open water results showed larger deviations from the experimental results for advance ratios larger than 0.8. It is recommended to further study the large deviations found for higher advance ratios.

From the flexible propeller study, it became clear that the thrust and torque obtained with experiments should be analysed. A lot of scatter was present in the measured results. Next to that, the comparison of flexible and rigid thrust and torque was not possible due to the different conditions in which the results were obtained. Both tests should be performed under the same inflow- and rotational velocity conditions to obtain results that can be compared.

The bending deformation at J=0.849 for RANS-FEM compared to the experiments was not in line with the thrust found both in RANS-FEM and experiments. It is recommended to obtain reliable rigid results first for this advance ratio, before the flexible results compared. For the bending of RANS-FEM compared to BEM-FEM it is recommended to analyse higher values for radius r to find bending that is in line with the thrust difference.

From the pitch deformation it was concluded that the RANS-FEM results and experiments did not correspond. The postprocessing of the pitch obtained from the experiments and simulations should be improved. Next to that, the modelling error of RANS-FEM at the tip of the propeller blade should be investigated. The analysis of an advance ratio between 0.369 and 0.849 can give more insight in the differences in pitch between RANS-FEM and experimental results. For the pitch comparison between RANS-FEM and BEM-FEM, the exact pressure differences and locations should be analysed to be able to draw a conclusion on the pitch differences that are found. Next to that, it is recommended to analyse the influence of the different arrangements of the tip elements in both FE models.

A

Appendix A

A.1. Interface Coupling

The coupling of fluid and structure is usually governed by kinematic and dynamic boundary conditions at the interface[10], these conditions on the continuous interface Γ are defined by,

$$\mathbf{u}_f = \mathbf{u}_s \quad \text{on} \quad \Gamma \tag{A.1a}$$

$$p_s \mathbf{n}_s = p_f \mathbf{n}_f \quad \text{on} \quad \Gamma \tag{A.1b}$$

with $\mathbf{u}_f$ and $\mathbf{u}_s$ the displacements, p_s and p_f the stress tensors and $\mathbf{n}_s$ and $\mathbf{n}_f$ the outward normal of the structure and fluid interface. These boundary conditions state that either the displacement fields of fluid and structure interface are equal. The other states that the pressure on the fluid side of the interface is in equilibrium with the structural side. The discrete representation of equations A.1a and A.1b is,

$$\mathbf{U}_f = H_{sf} \mathbf{U}_s \tag{A.2a}$$

$$\mathbf{P}_s = H_{fs} \mathbf{P}_f \tag{A.2b}$$

with transformation matrices H_{sf} and H_{fs} between the fluid and structure interface[10].

A conservative coupling approach is obtained if the energy is conserved across the fluid-structure interface[10]. This is the case when,

$$\int_{\Gamma f} \mathbf{u}_f \cdot p_f \mathbf{n}_f \, ds = \int_{\Gamma s} \mathbf{u}_s \cdot p_s \mathbf{n}_s \, ds \tag{A.3}$$

and using the discrete representation leads to,

$$[M_{ff} \mathbf{U}_f]^T \mathbf{P}_f = [M_{ss} \mathbf{U}_s]^T \mathbf{P}_s \tag{A.4}$$

with M_{ff} and M_{ss} defined by functions depending on the discretisation methods for displacement and pressure[10]. By substituting equation A.2a in equation A.4 and dividing by $\mathbf{U}_s^T$ gives,

$$H_{sf}^T M_{ff}^T \mathbf{P}_f = M_{ss}^T \mathbf{P}_s \tag{A.5a}$$

$$\mathbf{P}_s = [M_{ff} H_{sf} M_{ss}^{-1}]^T \mathbf{P}_f \tag{A.5b}$$

From equation A.5b it becomes clear that when H_{fs} is defined as $[M_{ff} H_{sf} M_{ss}^{-1}]^T$, the energy is conserved across the interface.

B

Appendix B

B.1. Iterative Error, Rigid J = 0.369

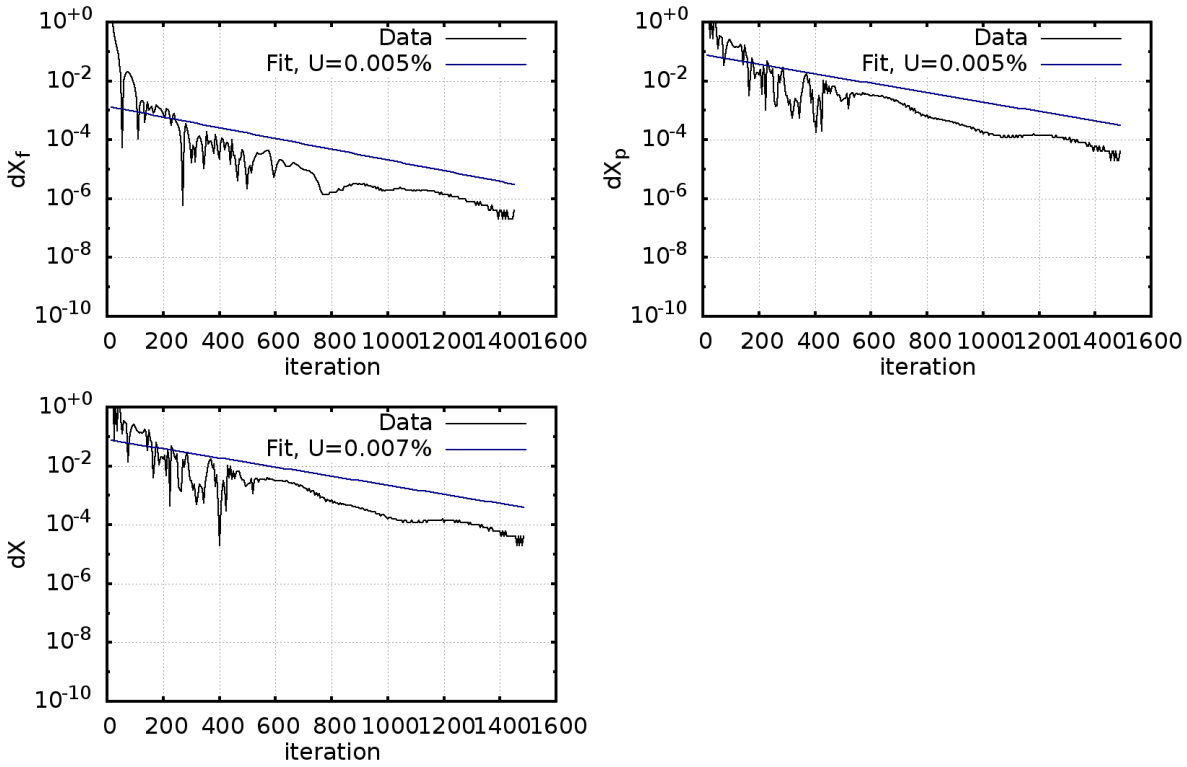

Figure B.1: Iterative error on results of force in x-direction, J=0.369

B.2. Iterative Error, Rigid J = 0.512

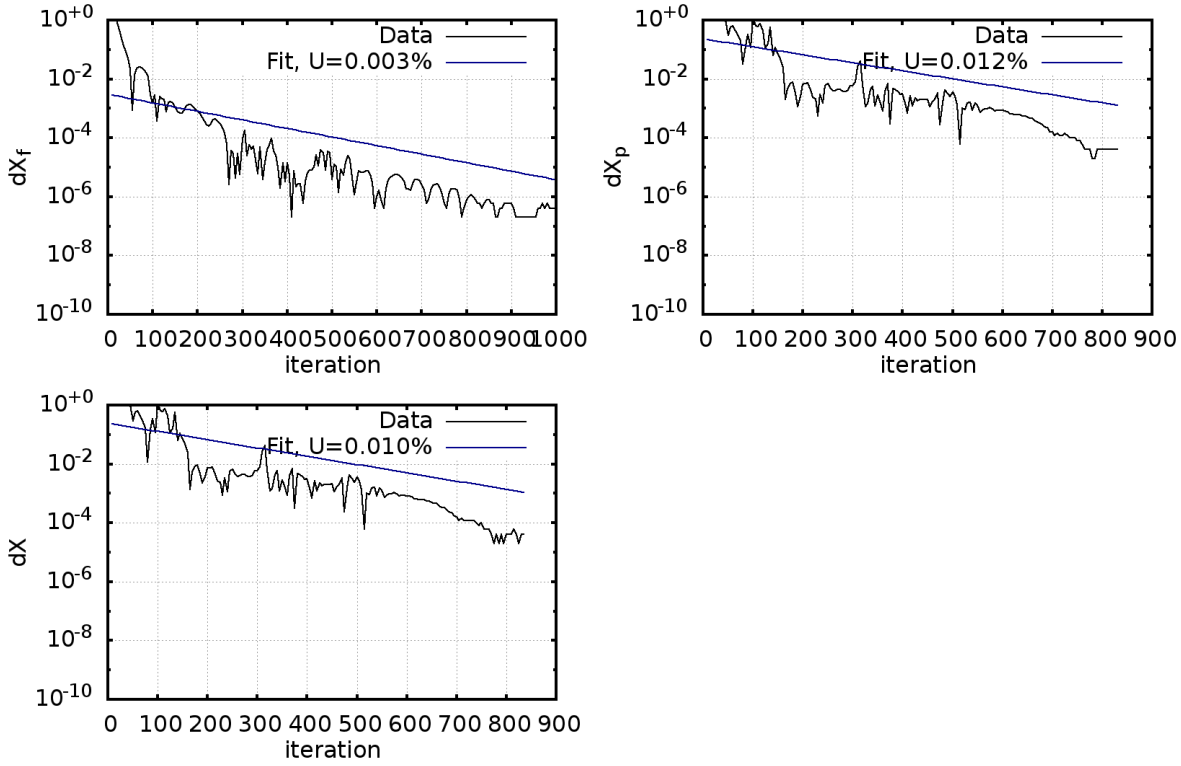

Figure B.2: Iterative error on results of force in x-direction, J=0.512

B.3. Iterative Error, Rigid J = 0.849

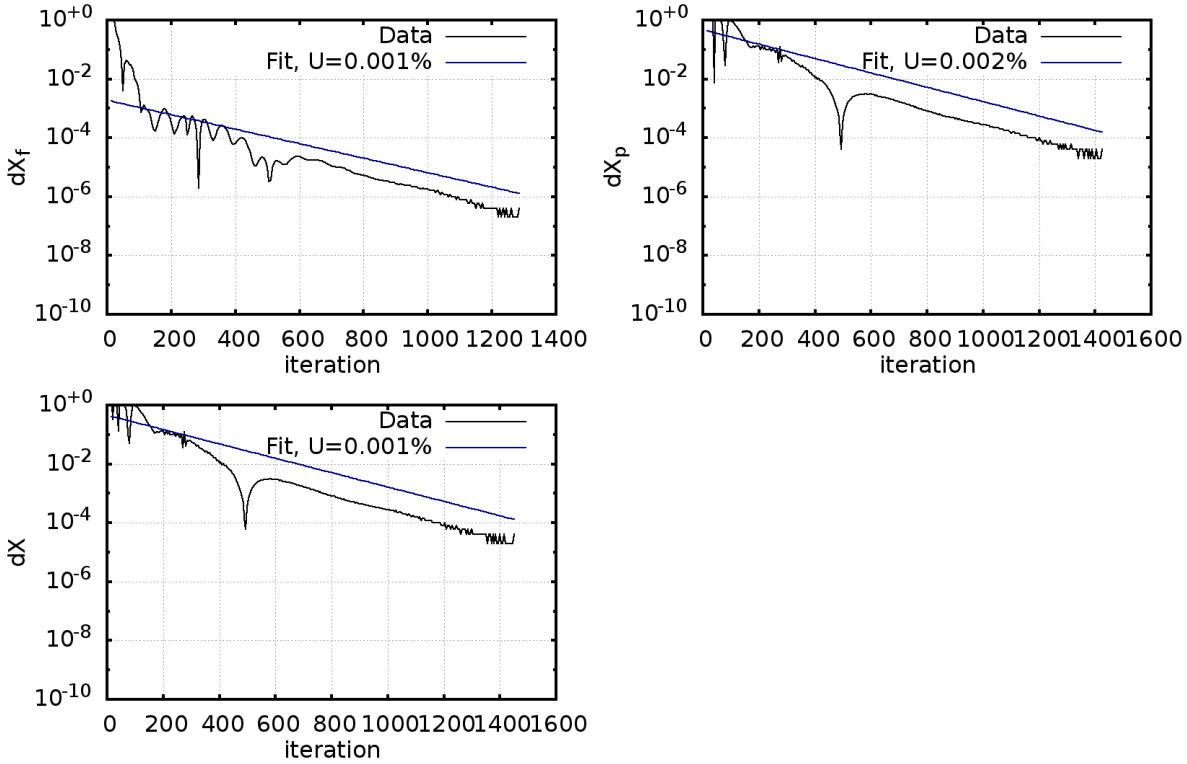

Figure B.3: Iterative error on results of force in x-direction, J=0.849

C

Appendix C

C.1. Numerical Uncertainties Propeller Studies

	FSI		RIGID	
Thrust	U [%]	p	U [%]	p
J=0.849	3.6	*1,2	7.7	*1,2
J=0.512	1.1	0.7	0.1	*1,2
J=0.369	1	2	0.7	1.7
Friction Force	U [%]	p	U [%]	p
J=0.849	5.57	0.74	5.2	*1,2
J=0.512	6.33	*1,2	6.6	*1,2
J=0.369	7.4	*1,2	7.7	*1,2
Torque	U [%]	p	U [%]	p
J=0.849	4.34	*1,2	11.2	*1,2
J=0.512	2	0.69	3.4	0.6
J=0.369	1.16	*1,2	1	0.7
Tip displacement	U [%]	p		
J=0.849	1.75	*1,2		
J=0.512	2.51	*1,2		
J=0.369	2.59	*1,2		

Table C.1: Numerical Uncertainties

Bibliography

[1] J. D. Anderson. *Introduction to flight - Fifth Edition*. Mc Graw Hill, 2004.

[2] H. Bijl, A. van Zuijlen, A. de Boer, and D.J. Rixen. *Fluid-structure interaction, an introduction to numerical coupled simulation*. TU Delft, 2008. Lecture Notes.

[3] P. Birken, T. Gleim, D. Kuhl, and A. Meister. *Fast Solvers for Unsteady Thermal Fluid Structure Interaction*. International Journal for Numerical Methods in Fluids, 2014.

[4] T. Bunnik, M. Hoekstra, C. Klaij, J. Windt, and G. Vaz. Refresco theory manual. Technical report, Maritime Research Institute Netherlands (MARIN) ARD project (Internal) v2.1.0, 2015.

[5] B.Y.H. Chen, S.K. Neely, T.J. Michael, S. Gowing, and R.P. Szwerc. Design, fabrication and testing of pitch-adapting (flexible) composite propellers. 2006.

[6] I. Chowdhury and S.P. Dasgupta. Computation of rayleigh damping coefficients for large systems. *The Electronic Journal of Geotechnical Engineering*, 8(0), 2003.

[7] International Towing Tank Conference. Propeller model accuracy. In *ITTC - Recommended Procedures and Guidelines*, number 7.5-01-02-02, 2005.

[8] R.A. Cumming, W.B. Morgan, and R.J. Boswell. Highly skewed propellers. 1972.

[9] A. de Boer, A.H. van Zuijlen, and H. Bijl. A new method for mesh moving based on radial basis function interpolation. *European Conference on Computational Fluid Dynamics*, 2006.

[10] A. de Boer, A.H. van Zuijlen, and H. Bijl. Comparison of the conservative and a consistent approach for the coupling of non-matching meshes. *European Conference on Computational Fluid Dynamics*, 2006.

[11] G. de Nayer. Interaction fluide structure pour les corps élancés. méchanique de fluides. Technical report, Ecole Centrale de Nantes, 2008.

[12] J. Degroote, K.J. Bathe, and J. Vierendeels. Performance of a new partitioned procedure versus a monolithic procedure in fluid-structure interaction. *Computers & Structures*, (87):793–801, 2009.

[13] A. Ducoin, F. Deniset, J.A. Astolfi, and J.F. Sigrist. Numerical and experimental investigation of hydrodynamic characteristics of deformable hydrofoils. *Journal of Ship Research, Vol. 53, No. 4. pp. 214-226*, 2009.

[14] L. Eca and M. Hoekstra. On the influence of the iterative error in the numerical uncertainty of ship viscous flow calculations. Technical report, 26th Symposium on Naval Hydrodynamics, 2006.

[15] L. Eca, R. Lopes, G. Vaz, J. Baltazar, and D. Rijpkema. Validation exercises of mathematical models for the prediction of transitional flows. *Proceedings of 31st Symposium on Naval Hydrodynamics, Berkeley. 11th-16th September*, 2016.

[16] R.D. Cook et al. *Concepts and Applications of Finite Element Analysis*. John Wiley and Sons, 4 edition, 2002.

[17] M.I. Gerritsma. Computational fluid dynamics, incompressible flows. *Delft University Press*, 2012.

[18] X.D. He, Y. Hong, and R.G. Wang. Hydroelastic optimisation of a composite marine propeller in a non-uniform wake. *Ocean engineering*, 2011.

[19] Numeca International. *HEXPRESS, Unstructured Full-Hexahedral Meshing*. http://www.numeca.com/, 2012.

[20] S. Jongsma, E.T.A. van der Weide, and J. Windt. Implementation and verification of a partitioned strong coupling fluid-structure interaction approach in a finite volume method. Technical report, MARIN Academy, Wageningen, 2016.

[21] S.H. Jongsma. On a method for performing fluid-structure interaction simulations with refresco. Technical Report 80165-12-RD, MARIN Academy, Wageningen, 2016.

[22] C. M. Klaij, G. Vaz, and L. Eca. Numerical uncertainty estimation in maritime cfd applications. *11th World Congress on Computational Mechanics (WCCM XI)*, 2014.

[23] G. Kuiper and S. Bernaert. *Resistance and propulsion 1 - MT527*. Faculty 3mE, Delft University of Technology, 2007.

[24] F.H. Lafeber, J. Brouwer, and J. Dang. A quasi-steady method for effectively conducting open water model tests. Technical report, MARIN, the Netherlands, 2013.

[25] H. Lesmana. Contribution to numerical modeling of fluid-structure interaction in hydrodynamics applications. Computational mechanics, Ecole Centrale de Nantes, 2011.

[26] M. Lombardi, N. Parolini, and A. Quarteroni. Radial basis functions for inter-grid interpolation and mesh motion in fsi problems. *Computer Methods in Applied Mechanics and Engineering*, 2013.

[27] P.J. Maljaars. Smart flexible propellers, hydroelastic analysis of flexible marine propellers. Master's thesis, Delft University of Technology, 2013.

[28] P.J. Maljaars. Development and validation of a steady bem-fem coupling. *Greenprop internal report*, september 2016.

[29] P.J. Maljaars and J.A. Dekker. Hydro-elastic analysis of flexible marine propellers. *Maritime Technology and Engineering - Guedes Soares & Santos (Eds)*, 2015.

[30] P.J. Maljaars and M.L. Kaminski. Hydro-elastic analysis of flexible propellers: An overview. *4th International Symposium on Marine Propulsors, Austin, Texas USA*, 2015.

[31] Maritime Research Institute Netherlands (MARIN). *CFD Code ReFRESCO (online)*. Available: http://www.marin.nl/web/Facilities-Tools/CFD/ReFRESCO.htm, 2010.

[32] Maritime Research Institute Netherlands (MARIN). *CRS Propagate Workshop - Part 3: Propeller Geometry*, 2012.

[33] Maritime Research Institute Netherlands (MARIN). *Numerical Uncertainty Analysis - User manual*, 2016.

[34] N.L. Mulcahy, B.G. Prusty, and C.P. Gardiner. Hydroelastic tailoring of flexible composite propellers. *Ships and Offshore structures 5:4, 359-370 DOI*, 2010.

[35] S.S. Raj and P.R. Reddy. Bend-twist coupling and its effect on cavitation inception of composite marine propellers. *International Journal of Mechanical Engineering and Technology (IJMET)*, 2014.

[36] S.S. Rao. *Mechanical Vibrations - 5th Edition - Chapter 8*. Pearson, 2011. ISBN-978-981-06-8712-0.

[37] T.C.S. Rendall and C.B. Allen. Evaluation of radial basis functions for cfd volume data interpolation. *48th AIAA Aerospace Sciences Meeting Including the New Horizons Forum and Aerospace Exposition, Orlando, Florida*, 2010.

[38] D.R. Rijpkema, J. Baltazar, and J. Falcao de Campos. Viscous flow simulations of propellers in different reynolds number regimes. *Fourth International Symposium on Marine Propulsors (SMP) Austin, Texas*, June 2015.

[39] S.M. Salim and S.C. Cheah. Wall y+ strategy for dealing with wall-bounded turbulent flows. *Proceedings of the International MultiConference of Engineers and Computer Scientists Vol II IMECS*, 2009.

[40] Inc. SAS IP. *ANSYS Help Version 17.1.0*, 2016.

[41] Inc. SAS IP. *ANSYS Element guide Release 16.2*, 2016.

[42] T. Taketani, K. Kimura, and K. Yamamoto. Study on performance of a ship propeller using a composite material. *Third International Symposium on Marine Propulsors*, 2013.

[43] A.H. Techet. Hydrodynamics for ocean engineers. Technical report, Massachusetts Institute of Technology, 2004.

[44] G. Vaz and D. Rijpkema. Non conformal and sliding interfaces in refresco. Technical Report 70015-13-RD, MARIN, the Netherlands, 2013.

[45] P. Wesseling. *Elements of Computational Fluid Dynamics*. Faculty ITS Applied Mathematics TU Delft, 2001. Lecture Notes WI4011 Numerieke Stromingsleer.

[46] J. Windt. Adaptive mesh refinement in viscous flow solvers: Refinement in the near-wall region, implementation and verification. *NUTTS*, 2013.

[47] H. Klein Woud and D. Stapersma. *Design of Propulsion and Electric Power Generating Systems*. IMarEST, 2008. ISBN1902536479.